

Air Force Institute of Technology

AFIT Scholar

Theses and Dissertations

Student Graduate Works

3-2020

Design and Analysis of a Compact Combustor for Integration with a JetCat P90 Rxi

Daniel Holobeney

Follow this and additional works at: <https://scholar.afit.edu/etd>



Part of the [Heat Transfer, Combustion Commons](#), and the [Propulsion and Power Commons](#)

Recommended Citation

Holobeney, Daniel, "Design and Analysis of a Compact Combustor for Integration with a JetCat P90 Rxi" (2020). *Theses and Dissertations*. 3215.

<https://scholar.afit.edu/etd/3215>

This Thesis is brought to you for free and open access by the Student Graduate Works at AFIT Scholar. It has been accepted for inclusion in Theses and Dissertations by an authorized administrator of AFIT Scholar. For more information, please contact richard.mansfield@afit.edu.



**DESIGN AND ANALYSIS OF A COMPACT
COMBUSTOR FOR INTEGRATION WITH A
JETCAT P90 RXi**

THESIS

Daniel Holobeny, Second Lieutenant, USAF
AFIT-ENY-MS-20-M-266

**DEPARTMENT OF THE AIR FORCE
AIR UNIVERSITY**

AIR FORCE INSTITUTE OF TECHNOLOGY

Wright-Patterson Air Force Base, Ohio

DISTRIBUTION STATEMENT A
APPROVED FOR PUBLIC RELEASE; DISTRIBUTION UNLIMITED.

The views expressed in this document are those of the author and do not reflect the official policy or position of the United States Air Force, the United States Department of Defense or the United States Government. This material is declared a work of the U.S. Government and is not subject to copyright protection in the United States.

AFIT-ENY-MS-20-M-266

DESIGN AND ANALYSIS OF A COMPACT COMBUSTOR FOR
INTEGRATION WITH A JETCAT P90 RXI

THESIS

Presented to the Faculty
Department of Aeronautics and Astronautics
Graduate School of Engineering and Management
Air Force Institute of Technology
Air University
Air Education and Training Command
in Partial Fulfillment of the Requirements for the
Degree of Master of Science

Daniel Holobeney, B.S.
Second Lieutenant, USAF

March 2020

DISTRIBUTION STATEMENT A
APPROVED FOR PUBLIC RELEASE; DISTRIBUTION UNLIMITED.

AFIT-ENY-MS-20-M-266

DESIGN AND ANALYSIS OF A COMPACT COMBUSTOR FOR
INTEGRATION WITH A JETCAT P90 RXI

Daniel Holobeney, B.S.
Second Lieutenant, USAF

Committee Membership:

Marc D. Polanka, PhD
Chairman

Lt Col James L. Rutledge, PhD
Member

Maj Brian T. Bohan, PhD
Member

Abstract

Ultra Compact Combustors are a novel approach to modern gas turbine combustor designs that look to reduce the overall combustor length and weight. A previous study integrated an Ultra Compact Combustor into a JetCat P90 RXi turbine engine and achieved self-sustained operation with a length savings of 33% relative to the stock combustor. However, that combustor could not operate across the full stock engine performance range due to flameout at increased mass flow rates as reactions were pushed out of the primary zone. To ensure reactions stayed in the primary zone, a new design with a larger combustor volume was conceived maintaining the same axial dimensions. The primary zone's volume was increased without changing the length by utilizing bluff body stabilization, which resulted in a space savings when compared to the previous backward-facing step stabilized configuration.

A new design was investigated computationally for generalized flow patterns, pressure losses, exit temperature profiles, and reaction distributions at three engine power conditions. The computational results were compared to stock combustor experimental results to show the validity of this new Ultra Compact Combustor, with a turbine inlet temperature of 1080 K and a pattern factor of 0.67. The combustor was then built and tested in the JetCat P90 RXi without rotating turbomachinery. The engine was force fed air and the combustor ignited at an air mass flow rate of 30 g/s and an equivalence ratio of 0.21. The combustor responded well to changes in air and fuel flow rates, maintaining a stable flame from ignition through the idle condition. Rotating turbomachinery was added and the combustor operated with an air assist of 3,000 RPM up to a maximum engine speed of 25,000 RPM, 19% of the maximum engine speed, at an exit gas temperature of 982 K, a 19 K increase over the stock.

Acknowledgements

It seems like a veritable task force came together to help me accomplish the work presented here. I would like to take a moment of your time to direct your attention towards the amazing support of several individuals that heavily impacted me and this research. First, I would like to thank my advisor Dr. Marc Polanka and my committee members Lt Col James Rutledge and Maj Brian Bohan. I would not have been able to accomplish this thesis without your expertise, mentorship, and support whether in the classroom, weekly meetings, or the lab. I would also like to thank my fellow peers 2d Lts Ricky Macias, Kavi Muraleetharan, and Bennett Staton who shared not only the COAL lab with me but also the daily grind of grad school.

The design, fabrication, and testing of the UCC required more people than I had originally imagined. My computational work was supported by Mr. Dave Doak who resolved any and all issues that I experienced on the Linux network. The AFIT Model Shop team of Mr. Brian Crabtree, Mr. Chris Harkless, Mr. Dean Harshman, Mr. Joe Owings, and Mr. Dan Ryan dedicated many hours to fabrication, assembly, and fixing my mistakes. Without their support, the experimental portion of this research would not exist. The AFIT ENY lab technician team provided me with the knowledge and expertise required to set up and run my experiments in the COAL lab. Thank you, Mr. Jamie Smith, Mr. Josh DeWitt, Mr. Keith Long, and Mr. Mike Ranft for your daily support.

Mr. Matthew Boehle out of AFRL helped deliver on the timeliness of this project by balancing the engine within a week of it being given to him. His efforts saved both time and money by having an on-base resource for this task. Mr. Jacob Wilson, a former AFIT graduate, collected experimental data on the stock JetCat P90 RXi that was instrumental in providing a baseline for the new UCC performance.

Finally, I would like to thank my family. To my parents and grandparents, thank you for your love and support throughout my time here at AFIT and in everything else. But this is not my only family. While at AFIT, my family has grown to include not only the close friends I had before, but the new friends I made while I was here. Whether at school, church, on Discord, or around Dayton each of my friends have cared for and supported me in some way. Of all these people one stands out the most, my future wife. Every day you brought me happiness, even when life was bringing me down. You provided me with more love and support than I could have ever asked for, thank you. I thank God for the blessings He has given me, and I pray that He guide, guard, and protect us in our many years to come. To my whole family, I love you and thanks for all the fish.

Daniel Holobeney

Table of Contents

	Page
Abstract	iv
Acknowledgements	v
List of Figures	ix
List of Abbreviations	xv
List of Symbols	xvi
I. Introduction	1
1.1 Ultra Compact Combustors	1
1.2 Small Gas Turbine Engine Integration	2
1.3 Objectives	3
1.4 Novelty of Research	4
II. Background	5
2.1 Turbulent Flame Stabilization	6
2.1.1 Combustion Fluctuations	9
2.1.2 Damköhler Number	11
2.2 Ultra-Compact Combustor	14
2.2.1 Recent UCC Implementations	16
2.3 Computational Fluid Dynamics	19
2.3.1 Turbulence Modelling	19
2.3.2 Conjugate Heat Transfer	20
2.3.3 Combustion Modeling	21
2.3.4 Grid Structures	22
2.3.5 Computational Modeling of Combustors	23
2.4 Combustor Exhaust Metrics	23
III. Methodology	27
3.1 Previous JetCat P90 RXi Combustor Testing	28
3.2 Combustor Design Iterations	29
3.3 Computational Analysis Setup	36
3.3.1 Grid Generation	37
3.3.2 FLUENT Case Setup	42
3.3.3 Grid Independence Study	45
3.4 Physical Hardware Production	46
3.5 AFIT Facility	50
3.5.1 Air Supply	50

	Page
3.5.2 Fuel Supply	51
3.5.3 Control Station	52
3.5.4 Non-Rotating Test Setup	54
3.5.5 JetCat Test Stand	61
3.6 Instrumentation	65
3.6.1 Non-Rotating Instrumentation	65
3.6.2 Rotating Instrumentation	67
IV. Results	70
4.1 Computational Results	71
4.1.1 Combustor Flow Path and Profile Analysis	71
4.1.2 Combustor Performance Comparison	80
4.2 Non-rotating Experimental Results	83
4.3 Rotating Experimental Results	94
V. Conclusions	99
5.1 Combustor Design	99
5.2 Computational Analysis	100
5.3 Non-Rotating Testing	101
5.4 Rotating Testing	103
Bibliography	105

List of Figures

Figure	Page
1. A cutaway of the JetCat P90 RXi showing key components of the engine.	3
2. Generic gas turbine engine combustor geometry.	6
3. The recirculation zone and flame spreading region in the wake region of a bluff body in fully developed turbulent flow.	8
4. Turbulent premixed flame regimes related to Damköhler number.	13
5. Comparison of the TVC and HGC concepts from Briones et al.	15
6. Lean blowout limit for a TVC studied under various annular-airflows by Hsu et al. relative to cavity length, H/d_f	16
7. The UCC configuration used by Bohan et al. for the JetCat P90 RXi	18
8. An example of a hybrid grid around an airfoil.	23
9. Combustor exit temperature profiles.	24
10. UCC experimental exit contours.	25
11. Experimental engine test stand.	29
12. Transition from inner diameter channel to outer diameter channel.	30
13. Computational result of a cutaway from an early outer diameter channel UCC model with total pressure contours (gauge Pa).	31
14. Open chamber design of the UCC for the JetCat P90 RXi.	32
15. JetCat P90 RXi final combustor design integrated into the engine.	34

Figure	Page
16. Cutaways of the JetCat P90 RXi UCC from Bohan et al. and the present research with engine casing and centerbody included.	35
17. UCC Solidworks model.	38
18. UCC Solidworks model used for CFD incorporating the compressor exit, engine case and centerbody, and turbine nozzle guide vanes.	38
19. An example domain where a structured grid was required instead of an unstructured grid.	40
20. Computational domain with boundary condition types identified.	40
21. The CFD domain with boundary conditions.	42
22. Monitor data taken at the nozzle guide vane exit for three different grids at the design condition.	44
23. The four lines used to determine grid independence.	45
24. Velocity and temperature profiles from the grid independence study.	46
25. The seven parts used to build the UCC.	47
26. Two pieces from the combustor stamped from Inconel 600 sheet metal.	48
27. Pieces from the combustor featuring the two rolled sheet metal parts.	48
28. The complete experimental combustor with welded pieces and propane feed system.	49
29. The air supply manifold for the AFIT COAL lab.	51
30. The propane manifold used to fuel the new combustor fed by the Alicat controller.	52
31. The COAL lab control station.	53
32. The LabView VI used for the engine control and data acquisitions systems.	54

Figure	Page
33. The JetCat P90 RXi installed without rotating turbomachinery.	55
34. The propane manifold line labeling system and configuration for the initial non-rotating testing.	56
35. The custom pieces from Bohan that were used during the non-rotating experimental testing.	57
36. The engine’s glow plug placement.	57
37. The thermocouple panel used to collect engine temperatures.	58
38. The pressure transducer assembly.	59
39. The thermocouple rake used to gather exit temperature profile data.	60
40. Engine mount system for the rotating testing.	61
41. Engine speed sensor integrated with the engine.	62
42. Side-by-side view of the newly designed and stock engine inlets.	63
43. The pump used to flow lubrication to the JetCat P90 RXi during rotating testing.	64
44. The rearranged propane line placement around the engine as viewed from the rear of the engine with glow plug and turbine nozzle guide vanes for reference.	65
45. A cutaway of the components present in the non-rotating testing with axial positions of thermocouples and pressure taps labeled.	66
46. The physical instrumentation placed in the non-rotating configuration.	66
47. A cutaway of the components present in the rotating testing with axial positions of thermocouples and pressure taps labeled.	67

Figure	Page
48. Thermocouple and static pressure tap placement at Station 2 for the rotating testing as viewed from the front of the engine.....	68
49. Thermocouple placements inside of the combustor for the rotating testing as viewed from the back of the combustor.....	68
50. Thermocouple and pressure tap placements at Stations 5 and 7 as viewed from the exhaust duct.	69
51. Velocity vectors (a) colored by velocity magnitude (m/s) on the center cut plane (b) at the design point, with recirculation zones behind the impingement plate highlighted (c). Outlined in purple are the dilution holes, which contribute 63% of the total air flow into the combustor.	72
52. Two views of flow pathlines, differentiated by color, entering through a forward dome inlet hitting the impingement plate.	72
53. Contours on the plane cutting through the fuel air mixing tube and the propane inlet tube, showing how the propane cracked once it reached the recirculation one and the mixing of fuel and air in the combustor.	73
54. Total pressure (Pa) contours on the center cut plane at the design point.....	74
55. Temperature (K) contours on the center cut plane at the design point. The cooling effect of the dilution holes is highlighted in purple.	75
56. Temperature (K) contours on the surface of the combustor for on and off design conditions.....	76
57. Comparison of the temperature (K) contours on the center cut plane at the mid-power and design conditions.....	77
58. Circumferentially averaged temperature profile before and after the turbine nozzle guide vane at the design condition, with the exit temperature contour from which it was derived in the top right corner.....	78

Figure	Page
59.	Pathlines, colored by temperature, showing the horseshoe vortex that formed off of the leading edge of the turbine nozzle guide vane on the outer diameter. On the inner diameter, the small cooling jets push the flow off the surface and stop a vortex from forming. 78
60.	Circumferentially averaged temperature profile at the pressure outlet plane after the turbine nozzle guide vane with average temperatures for each condition represented by the dashed lines. 79
61.	Comparison plots for the stock JetCat P90 RXi data, computational results from Bohan et al., and data from the present research. 81
62.	A photograph of the nozzle guide vane exit immediately following ignition in the non-rotating configuration. 85
63.	Average exit gas temperature as measured by the three thermocouples at the combustor exit plotted against air mass flow rate with equivalence ratio as a secondary axis. 86
64.	A photograph during Run 2 of the heated nozzle guide vanes with recorded temperature values reaching 1324 K. 86
65.	Temperature (K) contours from the thermocouple rake data. 88
66.	Comparison of the computational and experimental turbine nozzle guide vane exit temperature (K) contours at the idle condition. 89
67.	A photograph of the nozzle guide vanes with Vane 3 heated. 90
68.	The front of the stock engine diffuser with the smaller vane passage highlighted. 90
69.	A side view of the engine, highlighting the location of the large diffuser vane, where the screw holds the diffuser to the case. 91
70.	A rear view of the engine, highlighting the location of the diffuser irregularity with respect to turbine nozzle guide Vane 3. 91

Figure	Page
71. Several views of the combustor post non-rotating testing compared to the surface temperature contours from the computational results.	94
72. Temperature and fuel mass flow rate data against the engine speed from the first run of rotating testing.	95
73. Temperature and fuel mass flow rate data against the engine speed from the second run of rotating testing, up to 25,000 RPM.	96
74. Pressure data against the engine speed from the second run of rotating testing.	97
75. Compressor and turbine pressure ratios against the engine speed from the second run of rotating testing with predicted trendlines.	98

List of Abbreviations

Abbreviation		Page
UCC	Ultra Compact Combustor	1
UCC	Ultra-Compact Combustor	5
CFD	Computational Fluid Dynamics	5
ITB	Inter-Turbine Burner	14
HGC	High-g Cavity	14
TVC	Trapped Vortex Combustor	14
SLPM	Standard Liters per Minute	17
RPM	Revolutions per Minute	17
SST	Shear Stress Transport	19
RANS	Reynolds-Averaged Navier-Stokes	19
FGM	Flamelet Generated Manifold	21
PF	Pattern Factor	24
CAD	Computationally Aided Design	27
AFIT	Air Force Institute of Technology	28
COAL	Combustion Optimization and Analysis Laser	28
IGES	Initial Graphics Exchange Specification	39
T-Rex	Anisotropic Tetrahedral Extrusion	39
VI	Virtual Instrument	53
FS	Full Scale	65

List of Symbols

Symbol	Page
Φ	Equivalence Ratio 5
S_t	Local Turbulent Flame Speed (m/s) 7
\dot{m}_r	Reactant Flow Rate (kg/s) 7
\bar{A}_f	Time Smoothed Flame Area (m ²) 7
ρ_u	Unburned Gas Density (kg/m ³) 7
Q	Volumetric Flow Rate (m ³ /s) 10
A	Orifice Cross-Section (m ²) 10
K	Orifice Discharge Coefficient 10
Da	Damköhler Number 11
τ_{flow}	Characteristic Flow Time (s) 11
τ_{chem}	Characteristic Chemical Time (s) 11
A_{exit}	Combustor Exit Area (m ²) 11
V_{flow}	Local Flow Velocity (m/s) 11
V_f	Flame Propagation Speed (m/s) 11
l_0	Integral Length Scale (m) 12
u'_{rms}	Root Mean Square Velocity Fluctuation (m/s) 12
δ	Flame Thickness (m) 12
S_L	Laminar Flame Speed (m/s) 12
ρ	Mixture Density (kg/m ³) 13
\dot{m}	Mass Flow Rate (kg/s) 13
V	Combustor Volume (m ³) 13
H/d_f	Cavity Length 16

Symbol		Page
k	Turbulent Kinetic Energy (m^2/s^2)	19
ω	Specific Turbulence Dissipation Rate (1/s)	19
ϵ	Turbulent Dissipation Rate (m^2/s^3)	19
y^+	Non-Dimensional Wall Distance	20
T_{tmax}	Maximum Total Temperature at the Combustor Exit (K).....	25
T_{t4}	Average Total Temperature at the Combustor Exit (K)	25
T_{t3}	Average Total Temperature at the Combustor Inlet (K)	25

DESIGN AND ANALYSIS OF A COMPACT COMBUSTOR FOR INTEGRATION WITH A JETCAT P90 RXI

I. Introduction

1.1 Ultra Compact Combustors

Innovation drives all scientific pursuits, and in engineering innovation performance is king. Performance comes in many different forms, whether it is the power output of a basic internal combustion engine or the thrust-to-weight ratio that many jet turbine engines are measured by. The Ultra Compact Combustor (UCC) looks to increase performance in jet turbine engines by decreasing the overall length of the combustor, and thereby the total engine length as a means of reducing engine weight, providing space for other systems. Previous UCC research has seen successful combustion utilizing highly loaded circumferential flow to increase mixing and complete combustion in a short axial length, while maintaining comparable residence times. Most recently, Bohan et al. [1] was the first to integrate a UCC into a jet turbine engine. Bohan et al. utilized the JetCat P90 RXi small gas turbine engine as the integration platform. With this platform, the UCC was able to achieve self-sustained operation with rotating turbomachinery at 14,000 RPM, a low engine speed for small gas turbine engines. At higher engine speeds, and thereby higher air mass flow rates, the UCC experienced flameout where reactions were pushed out of the primary zone and off of its step-stabilized flame holders.

Bohan et al. [1] were able to prove the viability of a UCC in a small gas turbine engine, with some necessary changes. The UCC contained a constriction that increased

the flow velocity significantly, quenching the reaction. They recommended designing a combustor with a larger chamber volume and stable flame holding mechanisms. The larger volume would create lower chamber flow velocities, ensuring combustion reactions continued through the combustion chamber. In addition, a different flame holding mechanism would allow for a change in combustor flow paths, not requiring high velocity swirl in the combustion chamber. The present research looked to further develop the UCC for integration with the JetCat P90 RXi to achieve self-sustained operation at higher mass flow rates than the Bohan et al. [1] combustor was able to reach by utilizing a larger primary zone volume and more stable flame holding.

1.2 Small Gas Turbine Engine Integration

Small gas turbine engines utilize their small form factor in both the compressor and turbine stages. Due to their low mass flow rates, a single radial compressor stage is appropriate and provides a pressure ratio comparable to several staged axial compressors. In addition, this single compressor stage requires only a single turbine stage to drive it, reducing the necessary turbomachinery, mechanical losses, and complexity, when compared to large gas turbine engines. However, the combustor suffers from the scalability of combustion reactions. Figure 1 demonstrates the space taken up by the combustor with a cutaway of the JetCat P90 RXi, approximately 40% of the total engine length. A reduction in the combustor size would benefit the small gas turbine engine community with an increase in thrust-to-weight ratio as well as a reduction in combustor length up to 33%.

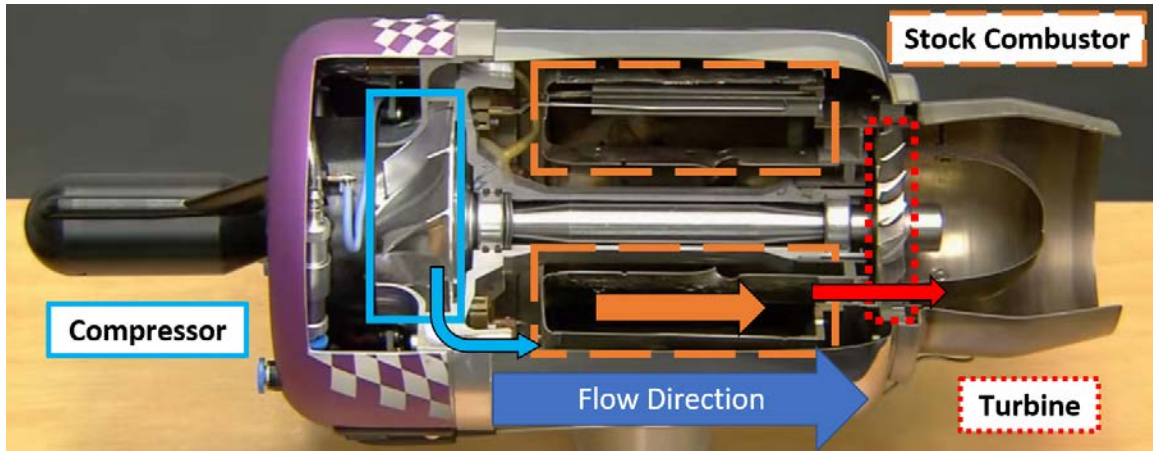


Figure 1. A cutaway of the JetCat P90 RXi showing key components of the engine.

1.3 Objectives

The primary goal of this research was determined based on previous work done by Bohan et al. [1][2][3], who demonstrated the viability of a UCC in a small gas turbine engine. As Section 2.2.1 discusses, Bohan et al. were able to achieve self-sustained combustion in a JetCat P90 RXi with a UCC, but were not able to achieve idle engine speeds due to combustor flame out. Therefore, utilizing the recommendations from Bohan et al., the primary goal of this research was to design a combustor that would maintain the same 33% length savings relative to the stock JetCat P90 RXi combustor that would operate in a self-sustained mode at full power. There were several sub-objectives necessary to accomplish this goal, to include:

1. Design a UCC, using computer aided software, that would integrate with the existing JetCat P90 RXi hardware, to provide an increase in combustor volume relative to the Bohan UCC while maintaining the same length savings of 33%, and incorporate stable flame holding mechanism.
2. Analyze the designed combustor with computational fluid dynamics at several

operating conditions to ensure the combustor provides a near ideal thermal profile to the turbine with similar or improved turbine inlet temperatures and combustor pressure drop relative to the stock combustor.

3. Manufacture and test the UCC in a non-rotating configuration of the JetCat P90 RXi up to the idle condition, to experimentally identify the exit profile of the combustor and its viability for use in a rotating configuration and turbine survivability.
4. Test the combustor in the JetCat P90 RXi with rotating turbomachinery to achieve self-sustained operation up to the maximum sustainable engine speed.

1.4 Novelty of Research

The research presented here built off of the previous work of Bohan [3]. Bohan achieved successful self-sustained engine operation powered by a UCC at low mass flow rate conditions, which fell below the stock engine's idle condition. Bohan was the first to achieve this form of operation with a UCC. This research looked to achieve self-sustained engine operation at higher mass flow rates, pushing past the previously reached engine speed of 14,000 RPM, all with a novel compact combustor design.

II. Background

The objective of this work was to design a compact combustor to operate at full engine power in a JetCat P90-RXi with a 33% length savings. To accomplish this objective several topic areas are needed to be researched. Among these topics included flame stabilization due to the turbulent flames in gas turbine combustors. Flame stabilization is discussed in Section 2.1, along with unsteady combustion and how to avoid it. Due to the small size of the 100 N thrust class JetCat P90 RXi, an Ultra Compact Combustor (UCC) is required to realize a length savings. Previous work has been done to study the UCC concept in the JetCat and is presented in Section 2.2. Computational Fluid Dynamics (CFD) was used to reduce time between design iterations for the new combustor. CFD is a helpful design and evaluation tool, that has been used for previous combustor research. Section 2.3 goes into detail about the relevant models and grid structures necessary for computational analysis of a combustor. As with any design, certain parameters need to be met to determine a suitable end state. For combustors, exhaust metrics exist to evaluate combustor performance and efficiency and to provide a favorable exit temperature profile to the turbine hardware. Section 2.4 introduces the circumferentially averaged exit temperature profile and pattern factor.

When designing a new combustor geometry, an understanding of conventional combustor geometry and performance metrics is required. According to Mattingly [4], in a conventional combustor the primary zone introduces fuel into the combustor, as shown in Fig. 2. In this region, a small portion of the core air flow mixes with the fuel and experiences a rich-burn ($\Phi > 1.5$). The fuel-air mixture then transitions into the secondary zone where the flame quenches with dilution air and continues to burn lean. This process allows the combustion event to skip over stoichiometric burning to achieve better emissions and lower heat loading to the metal components. The hot

products must then exhaust through the combustor exit. With modern combustors reaching temperatures greater than 2000 K [5], the exhaust gas characteristics are of significant interest to keep turbine blades from melting.

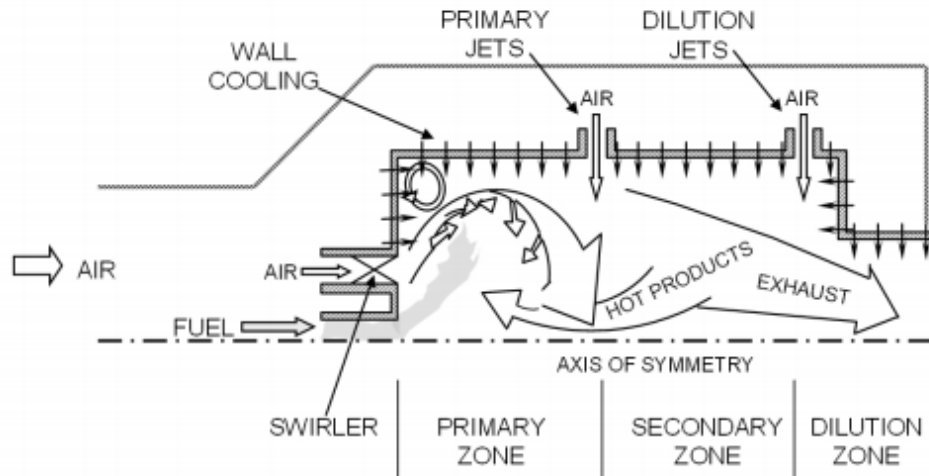


Figure 2. Generic gas turbine engine combustor geometry [6].

2.1 Turbulent Flame Stabilization

Stable flames drive performance and efficient operation of jet turbine engine combustors. Turns [7] describes a stable flame as “one that is anchored at a desired location and is resistant to flashback, liftoff, and blowoff over the devices operating range.” Flashback occurs when a flame enters and propagates back up a fuel tube, burner tube, or port without quenching. This can result in fuel sources igniting or flame propagation into unwanted regions upstream of the combustion chamber. A flame experiences liftoff when it is attached at a point some distance away from a burner tube or port. Lifted flames are hard to control and can generate large amounts of noise. Lastly, the extreme case of liftoff, where the flame has lifted off to the point that it is no longer supplied by a fuel or air source and quenches is called blowoff.

Turns also noted that it is important for a stable flame that the local turbulent flame speed (S_t), defined in Equation 1 [7], is matched to the local mean flow velocity.

$$S_t = \frac{\dot{m}_r}{\bar{A}_f * \rho_u} \quad (1)$$

In Equation 1 \dot{m}_r is the reactant flow rate, \bar{A}_f is the time smoothed flame area, and ρ_u is the unburned gas density. Due to the chaotic nature of turbulent flames, \bar{A}_f is difficult to determine theoretically or measure experimentally and leads to ambiguity in turbulent flame speed between different experiments [7].

The balance of turbulent flame speed and local flow speed drives flame stabilization. Recirculation zones are implemented to create regions where the flame speeds match the local flow speeds and achieve stable combustion. The wake region of a bluff body in a reacting flow forms a fixed vortex, the aforementioned recirculation zone [8]. Figure 3 shows the recirculation zone behind a flat disk bluff body. The recirculation zone is the area between the back of the bluff body and where the flow reverses direction in the wake of the bluff body. The gasses within the recirculation zone are burned products at a constant (near adiabatic) temperature [7]. The flame front resides on the edges of the body's wake and the incoming fuel-air mixture is ignited by the burnt gasses in the recirculation zone.

Williams [8] cataloged the findings of several bluff body studies. He found that the length of a recirculation region was independent of the upstream flow Reynolds number above a critical Reynolds number of 10^4 and became a linear function relative to the body diameter in fully turbulent flows. In addition, the flame spreading rate in the wake of the bluff body was found to be independent of increases in the incoming flow turbulence, increases in the bluff body diameter, and changes in the bluff body shape; however, an increase in incoming flow velocity was noted to result in a decrease of flame spreading angle [8].

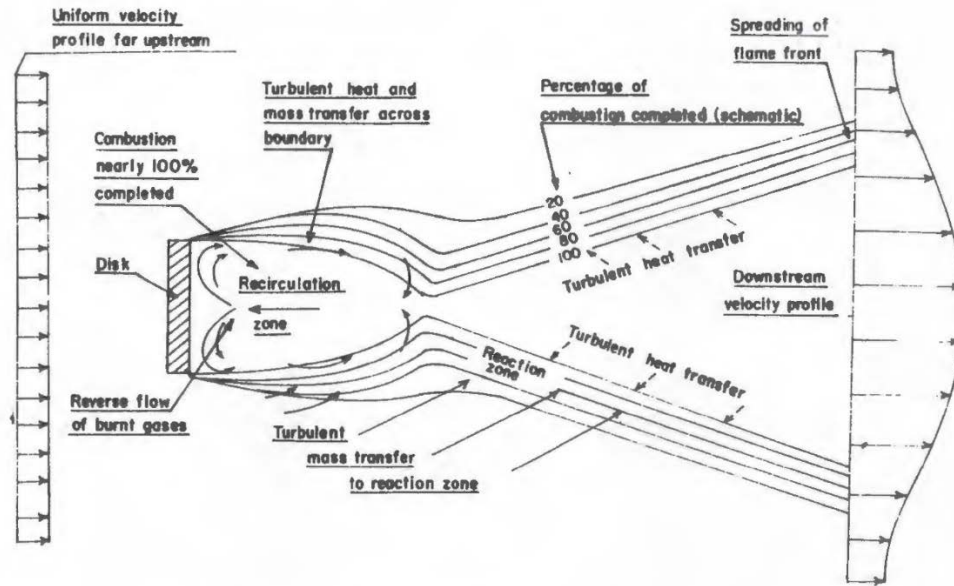


Figure 3. The recirculation zone and flame spreading region in the wake region of a bluff body in fully developed turbulent flow [8].

Other geometries also create recirculation regions. A rapid increase in flow area, such as steps or cavities, sets up a recirculation zone where the burned products sit, igniting the unburned reactants [9]. The local turbulent flame speed and local mean velocity are matched in these regions, similar to the area behind a bluff body. Steps and cavities are most often used in situations where the mean flow velocity is high and the fuel needs a shielded region to mix with the oxidizer and ignite. The benefit of a step or cavity geometry is the access to jets in the wall of the hardware. By implementing jets into the walls of the step/cavity, fuel or air can be injected directly into the recirculation zone at a desired mass flow rate. This constantly supplies the recirculation region with products rather than relying on a mixed core flow to supply products to the recirculation region. Recirculation zones can also be generated by free standing swirl or jet induced recirculating flows. Jets further enhance the recirculation zones within cavities. By setting up counter-opposing jets in a cavity, a

strong recirculation zone can be achieved. A potential use for counter-opposing jets is the Trapped Vortex Combustor discussed in Section 2.2.

2.1.1 Combustion Fluctuations

Unsteady flames within the combustor can lead to flame blowout and material deformation. When unsteady combustion develops, pressure waves form within the closed volume of the combustor and generate undesirable loading. Huang et al. [10] discussed five main mechanisms for unsteady combustion: acoustic motion in the combustion chamber, flame surface variation, equivalence ratio fluctuation, vortex shedding due to hydrodynamic instability, and oscillatory liquid fuel atomization and droplet evaporation. Due to the closed acoustic environment and large energy production within the combustion chamber, the most problematic of these fluctuation inducers is acoustic waves. These acoustic waves propagate through the entire combustor and drive unsteady heat transfer and pressure fluctuations, which cause fluctuations in combustor exit profiles to the turbine.

The most effective guard against these fluctuation mechanisms, especially for the limited space in small engines, is passive suppression. Passive suppression is meant to interrupt the feedback loop that develops between acoustic waves and unsteady heat release, as one causes the other. Huang et al. [10] states, “Passive control involves changes of fuel or hardware designs...either to reduce the rate at which energy is transferred to unsteady motions, or to increase losses of energy.” By reducing energy transfer rate and increasing energy loss, the acoustic waves causing fluctuations have less energy with which to disrupt the heat release, leading to more steady combustion.

Acoustic dampeners are a useful passive suppression system when acoustic waves dominate the unsteadiness within the combustor. The simplest method of acoustic dampening is dilution holes. Dilution holes create an outlet for the acoustic waves

and help dampen unsteady heat release through the introduction of cool, unburnt air.

Since the combustor liner is thin, the dilution holes through the liner are governed by orifice flow theory. Flow through these holes is driven by the pressure differential on either side of the liner. Equation 2 displays the importance of the pressure difference in determining the volumetric flow rate, Q , through the orifice. The cross-sectional area of the orifice, A , can be varied to control the flow through the hole and the variable K is an orifice discharge coefficient that accounts for the non-ideal effects present. For flow through thick walls this coefficient is approx 0.8 and for thin walls the coefficient is closer to 0.6 [11].

$$Q = KA\sqrt{\frac{2\Delta P}{\rho}} \quad (2)$$

Orifice flow theory is the mechanism by which dilution holes transport cool, unburnt air to the combustion chamber. This dilution air takes energy away from the reacting flow by cooling the flow temperature and reducing the equivalence ratio of the mixture. When this air dilutes the reacting mixture, either the reaction will quench from too much dilution or will complete combustion at a lean condition. Therefore, dilution holes can dampen unsteady combustion reactions by reducing the mixture temperature, thereby taking away energy, and by furthering the combustion process. In addition, dilution holes provide an ideal location for flames to stabilize off of due to their constant fresh air supply and the shear layer formed by the orifice's jet penetrating into a fuel-air mixed flow.

Hunag et al. [10] also discussed methods to resolve flame instabilities relative to fuel flow. A method known as fuel staging can be introduced, where a pilot fuel source is added to help stabilize the main combustion process. The author warns that these methods tend to decrease combustor performance and are not recommended as they are complicated to implement correctly for each individual combustor. In addition,

acoustic waves create an unstable feedback loop with the fuel-air mixing mechanisms within the combustor and result in equivalence ratio fluctuations. A potential solution is mixing the fuel and air before introducing it to the chamber and installing good injection systems for the mixture. When gaseous fuel is used and the nozzles are not choked, a back-pressure fluctuation can occur where the fuel flow rate changes as the pressure inside the combustor fluctuates. Bohan et al. [12] observed this situation in their experimental setup, causing fluctuations in equivalence ratio. To stop these fluctuations, a liquid fuel can be used to stop the back-pressuring effect or the gaseous fuel can be choked close to the combustor inlet.

2.1.2 Damköhler Number

Just as the turbulent flame speed and local flow speed need to be balanced for stable flames, the combustion mixture’s flow time and chemical time balance determines the type of turbulent flame structure. Damköhler number, Da , is a non-dimensional parameter relating the characteristic flow time, τ_{flow} , to the characteristic chemical time, τ_{chem} , of a reacting mixture [7]. Damköhler number is given in Equation 3. The flow time reflects a fluid’s mixing rate where the chemical time describes the mixture’s reaction rate. Bohan [3] provided generic definitions of τ_{flow} and τ_{chem} in Equations 4 and 5, where A_{exit} is a combustor’s exit area, V_{flow} is the local flow’s velocity, and V_f is a flame’s propagation speed.

$$Da = \tau_{flow} / \tau_{chem} \tag{3}$$

$$\tau_{flow} = \frac{\sqrt{A_{exit}}}{V_{flow}} \tag{4}$$

$$\tau_{chem} = \frac{1cm}{V_f} \tag{5}$$

Equations 4 and 5 allow for a simplified calculation of flow and chemical times applicable to a generic combustor, where all the presented variables can be determined through experimentation or computational methods.

Damköhler number helps describe the characteristics of a turbulent premixed flame. Figure 4 shows the different turbulent flame structures, driven by Damköhler number. A flame with $Da \gg 1$ indicates fast chemistry, where the chemical reaction rate is faster than the flow's mixing rate, and a $Da \ll 1$ would represent a slow chemistry reaction [3]. A common way to represent Damköhler number for premixed turbulent flames is shown in Equation 6 and involves the integral length scale l_0 , the root mean square velocity fluctuation u'_{rms} , the flame thickness δ , and the laminar flame speed S_L [7].

$$Da = \frac{l_0/u'_{rms}}{\delta/S_L} \quad (6)$$

This relationship is useful for determining the flame structure of a turbulent premixed flame when being compared to the turbulent Reynolds number, defined in Equation 7 [3],

$$Re_{l_0} = \frac{l_0 u'_{rms}}{\nu} \quad (7)$$

where ν is kinematic viscosity. Figure 4 can be used to compare these two parameters and determine the turbulent flame structure. When the flame parameters fall within area B, the turbulent flame structure is considered flamelets in eddies. Most practical combustion devices fall in this region [7]. The flames in this region reside within the turbulent eddies of the flow, between the integral and Kolmogorov length scales.

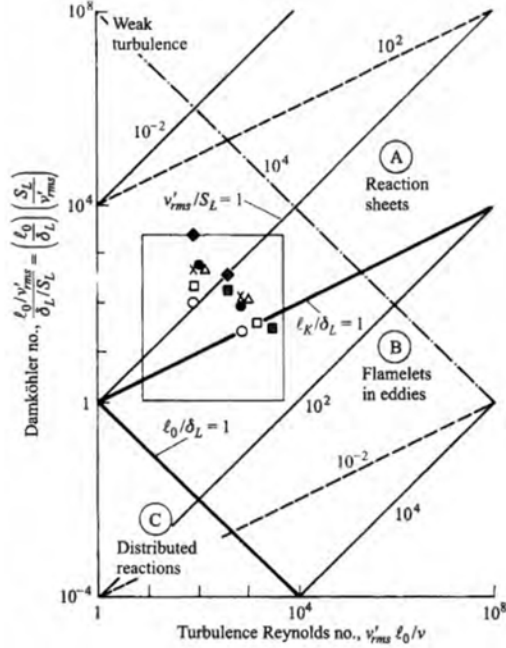


Figure 4. Turbulent premixed flame regimes related to Damköhler number [7]

Another relevant combustion parameter is residence time. While Damköhler number looks at the ratio of flow and chemical times, residence time looks only at the amount of time a mixture spends inside of the reaction area, without relating it to chemical time. Residence time is defined in Equation 8 and is a function of the mixture density ρ , the mass flow rate through the reaction area \dot{m} , and the combustor volume V [7]. Residence time can be a useful parameter for comparing how long reactions remain inside different combustors that utilize the same operating conditions and reactants.

$$t_r = \frac{\rho V}{\dot{m}} \quad (8)$$

Residence time has been a parameter of interest for previous UCC related research [13], due to its importance in combustor efficiency and performance. When the residence time is less than the chemical time, a mixture cannot achieve full combustion. However, a high residence time traps reaction products and decreases combustor per-

formance. There are no obvious sources confirming residence time values for the small scale combustor; however, values would be on the order of tenths of a millisecond, based on the geometry and full power mass flow rate of the JetCat P90-RXi stock combustor. Section 2.2.1 discusses recent findings that emphasized the importance of considering residence time in UCC design.

2.2 Ultra-Compact Combustor

The UCC developed from the initial findings of Sirignano et al. [14]. The study suggested the use of a constant temperature burn cycle where the fuel-air mixture would burn in between turbine stages, dubbed an inter-turbine burner (ITB). Due to the small spacing between turbine stages, the ITB would burn in a cavity on the outer diameter of the engine. The ITB grew into the UCC concept: that a combustor's overall length could be reduced by burning circumferentially rather than axially [15].

Both high-g loaded combustion and trapped vortex combustion designs have been used for the UCC. The benefits of circumferentially swirled high-g loaded combustion were initially studied by Lewis [16]. Lewis showed a 3% pressure drop across the swirl, no reliance on flame stabilizers that blocked the flow, high mixing properties, combustion efficiency on the order of 97%, and higher flame speeds and shorter flame lengths than those of conventional combustors. Briones et al. [17] studied the same effects as Lewis but through Computational Fluid Dynamics (CFD). The data obtained computationally by Briones et al. matched closely with the experimental data obtained by Lewis. Briones et al. also explained that the increased centrifugal forces led to higher Rayleigh-Taylor instabilities which drove the increased flame propagation.

A UCC that utilizes the concept of high g-loaded circumferential combustion can be referred to as a high-g cavity (HGC). Figure 5 compares the HGC concept to the Trapped Vortex Combustor (TVC). An HGC employs centrifugal forces to push the

flow outwards and swirl it in a cavity around the central axis in a circumferential manner, where the fuel and air were introduced on the outer diameter at angles in the desired direction of swirl, imparting a tangential velocity component. This design forces the reactants to the outside of the cavity and the products inward towards the core of the engine [17]. The TVC employs a cavity where the fuel and air are introduced into the cavity parallel to the flow but at different heights and in opposite directions to create a recirculation vortex within the cavity that wraps around the circumference of an engine. This design does not involve high centrifugal forces within the combustor cavity [17].

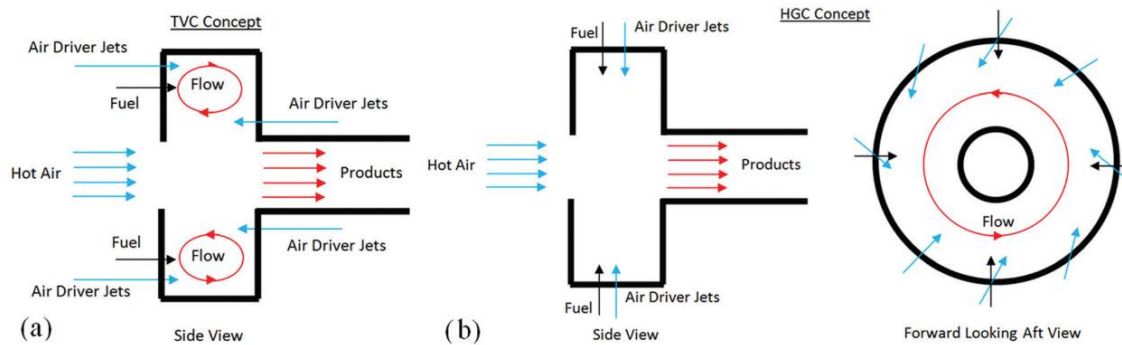


Figure 5. Comparison of the (a) TVC and (b) HGC concepts from Briones et al. [17].

Hsu et al. [18] determined that a TVC had both low lean blowout limits and high flame stability. The combustor experienced lean blowout at overall equivalence ratios between 0.01 and 0.04, depending on cavity length and cavity air flow velocity with a cavity equivalence ratio of 1.2, as shown in Fig. 6. Hsu et al. attributed the low blowout limit to the cavity being hidden from core flow and the stable vortex that was set up in the cavity. The vortex setup was relatively independent of primary air flow, cavity air flow, and fuel flow conditions. This also led to high flame stability [18].

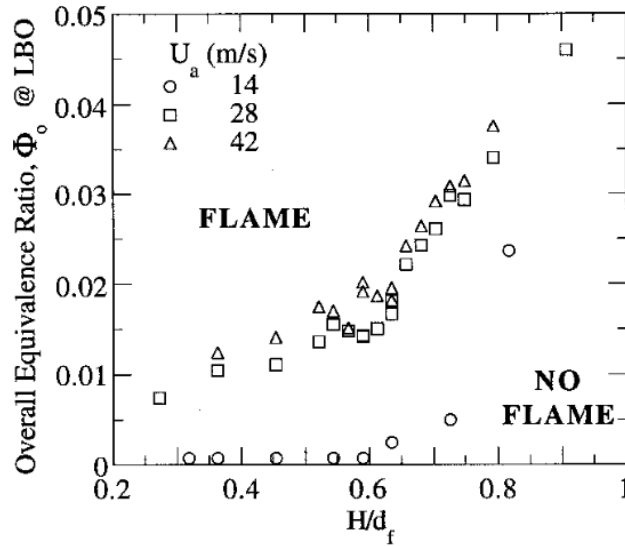


Figure 6. Lean blowout limit for a TVC studied under various annular-airflows by Hsu et al. relative to cavity length, H/d_f [18].

2.2.1 Recent UCC Implementations

Recent UCC applications at AFIT have focused on creating HGC designs to shorten the overall combustor length. Demarco et al. [13] utilized an HGC-UCC with a front driver plate and a 12 step outer cavity ring. The steps injected fuel and air on their back faces and acted as flame holders. Demarco et al. conducted tests where air flow was split between the driver plate, the step ring, and the core air flow. Through this testing, they were able to determine that the centrifugal loading where the combustor operated best fell between 18 g's and 125 g's. This range of values was significantly lower than the recommended range of Lewis [16] or Briones [17]. Demarco et al. concluded that the best combustion occurred at these lower loading values due to the slower cavity speeds, leading to a higher cavity residence time. This implied that the benefits of increased residence time for the burning mixture outweighed the mixing benefits of high centrifugal loading.

Bohan et al. [1][2] developed the first HGC-UCC for integration with the JetCat P90 RXi, shown in Figure 7. The UCC design featured air inlet ramps and scoops that fed the primary zone through backward-facing steps that also injected fuel and acted as flame holders. This method of feeding the primary zone induced a circumferential swirl, hence the high-g nature of the combustor. Following the primary zone, the fuel-air mixture passed through a constriction into the dilution zone, in which holes on the inner and outer diameter diluted to the mixture to complete combustion and tailor the profile for the turbine. The UCC ran on propane rather than the stock choice of kerosene and therefore required a custom designed fuel manifold and injection system separate from that of the stock engine. Propane was utilized for its ease of control and availability in the lab for combustor testing.

Bohan et al. replaced the stock combustor with the UCC which was integrated into the existing hardware of the JetCat P90 RXi (discussed in more detail in Chapter III). This UCC measured 44.1 mm, granting a 33% axial length reduction over the stock combustor length of 70 mm (as measured from the forward edge of the combustor to the forward edge of the turbine nozzle guide vane). The combustor was tested on a small engine test stand in the COAL laboratory at AFIT. The test stand was able to measure thrust and spool the engine with an air starter up to 6,000 RPM. The engine was instrumented to collect both temperature and pressure data using K-Type thermocouples and pressure taps leading to a pressure transducer. Bohan et al.'s combustor powered the JetCat P90 RXi in a self-sustained rotating configuration at 14 SLPM of propane and 14,100 RPM, the half-idle condition for the engine. This was the highest self-sustained condition the engine achieved with the HGC combustor. The UCC was able to achieve a 10% increase in exit temperature compared to the stock combustor at this condition. However, the HGC-UCC would not sustain combustion above this condition. Bohan et al. determined that this

was due to the loss of flame stabilization in the primary zone. When higher mass flow conditions were tested, the flame was pushed out of the primary zone and into the dilution zone, as shown in Figure 7, where it blew out from a lack of flame stabilization. The cause of the flame migration was attributed to high tangential velocities in the primary zone and the relatively small volume of the primary zone (discussed in more detail in Section 3.2). Ultimately, Bohan et al. suggested a new design that accounted for the loss of primary zone reactions through an increased primary zone volume and more stable flame holding mechanisms, to hold the reactions rather than having them migrate away from the flame holders. This was the influence for the present research.

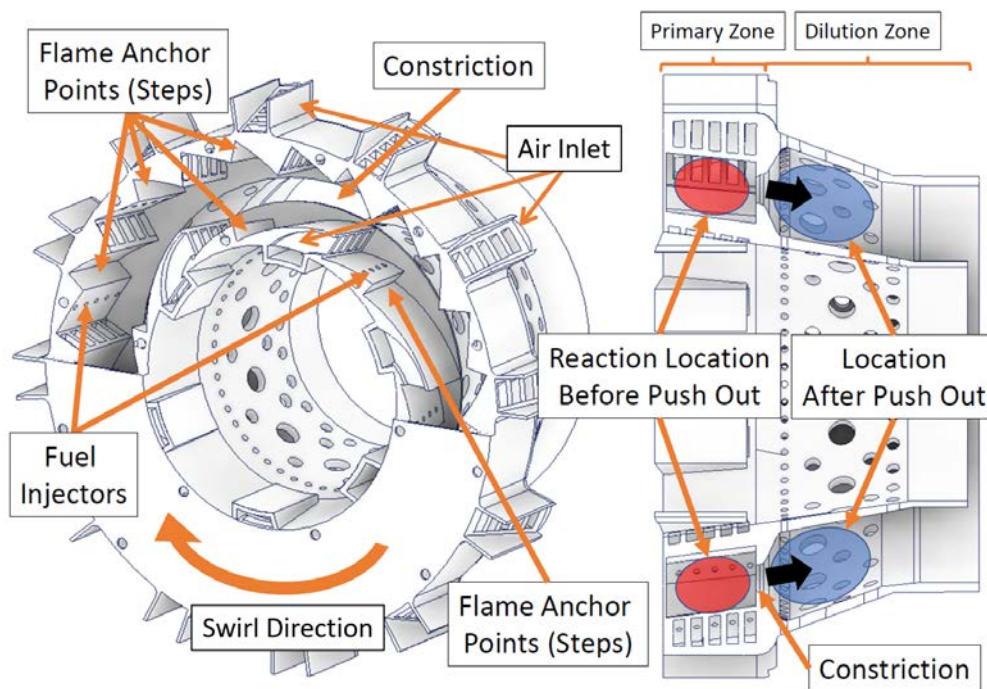


Figure 7. The UCC configuration used by Bohan et al. for the JetCat P90 RXi (adapted from [1] by highlighting the primary zone cross-section with flame holders and fuel injectors).

2.3 Computational Fluid Dynamics

Today there exist many different Computational Fluid Dynamics codes and software packages that help engineers make design decisions and evaluate hardware. ANSYS FLUENT is a common commercially available CFD software package with a robust program and verified code. FLUENT is capable of three-dimensional numerical solutions involving turbulence, heat transfer, species transfer, and combustion reactions [19]. These areas are critical for numerical analysis of a new combustor design. In addition, Bohan et al. [3] [2] [1] utilized FLUENT for his numerical analysis, providing a methodology to follow. This section will discuss the $k - \omega$ Shear Stress Transport (SST) turbulence model, conjugate heat transfer modelling, the partially premixed combustion model, and computational grid structures. This research implemented these computational models to provide comparable results to Bohan et al. [2].

2.3.1 Turbulence Modelling

Several validated turbulence models are utilized within the FLUENT software [20]. Bohan [3] provided a discussion of the turbulence models used in previous combustion research. He determined that the $k - \omega$ SST model would be best suited for computational analysis of his combustor design, due to its implementation for wall bounded flows.

The $k - \omega$ SST turbulence model is a two equation eddy-viscosity Reynolds-averaged Navier-Stokes (RANS) model that breaks the computational fluid domain into two regions: the near-wall region and the far-field region [21]. In the near-wall region, the model solves the turbulent kinetic energy (k) and the specific turbulence dissipation rate (ω) equations. In the far-field region, the model switches to using the $k - \epsilon$ equations which solves the turbulent dissipation rate (ϵ) as opposed to the

specific turbulence dissipation rate. When $k-\omega$ is applied, the model does not require a damping function and has better treatment of compressibility and adverse pressure gradients. The $k-\epsilon$ model provides better solutions for wake regions and free shear flows and performs best in favorable pressure gradients, hence its use far from the wall. By applying the SST developed by Menter [22], the $k-\omega$ SST turbulence model is better able to predict when separation occurs and keeps the model from over-predicting eddy-viscosity. With the addition of SST, the model is more viable for use in adverse pressure gradient flows [20].

When using $k-\omega$ SST, the non-dimensional wall distance, y^+ , of the first fluid cell must be between one and 500 and enhanced wall treatments should be engaged to accurately model the viscous effects near the wall [3]. The small y^+ value also allows for accurate modeling of the heat transfer between the walls and the fluid with conjugate heat transfer.

2.3.2 Conjugate Heat Transfer

Conjugate heat transfer is required when the heat transfer through a solid, fluid, and the solid-fluid interface need to be considered. To carry the calculation of heat transfer through all the surfaces, the same computational domain is used for the solid and the fluid. By doing so, the fluid experiences the correct heat transfer boundary conditions, without the need for a user input temperature [23].

The conjugate heat transfer model is important for combustors due to hot gases interacting with metal surfaces. This interaction draws heat from the fluid into the wall and can contribute to flame quenching at a cold wall interface or fuel vaporization at a hot wall interface. In addition, modeling the wall temperature helps determine if fluid temperatures near the wall are too high and would result in a loss of wall structural integrity.

Bohan [3] recommended the use of conjugate heat transfer when modeling combustors. He stated that when an adiabatic model was used, the fluid’s temperature was over-predicted from a lack of heat transfer into the surrounding metal walls. By not allowing for heat transfer into the walls, the computational model was not able to account for quenching of the combustion process and would lead to higher exit temperatures. Downstream temperatures would see as much as 500 K drop in temperature between the conjugate and adiabatic models. Although the temperature magnitudes varied, the profile shapes remained constant. From this analysis, the conjugate model was better able to predict combustor exit temperatures that matched experimental results.

2.3.3 Combustion Modeling

The FLUENT partially premixed combustion model with flamelet generated manifold and diffusion flamelets was implemented to match the methods employed by Bohan [3]. The partially premixed combustion model is useful for “lean premixed combustors with diffusion pilot flames and/or cooling jets” [20]. This means that the model can predict flame quenching due to heat extracted by the combustor walls and dilution air holes.

The flamelet generated manifold (FGM) option of the partially premixed combustion model assumes that the thermochemical processes occurring in the turbulent flames are the same as those that occur in the laminar flame. The processes are tracked with two parameters: mixture fraction and reaction progress. The reaction progress, or progress variable, ranges from zero to one and represents the effects of flame fluctuations, intermediate chemical reaction progress, and incorporates the mixture fraction. FGM allows for natural modelling of flame quenching as it captures the effects of mixture fraction changes from dilution air jets with the diffusion flamelets

sub-option. The diffusion flamelets setting determines quenching using the progress variable and checks it against an extinction number calculated from the thermochemical properties of an extinguished diffusion flamelet. This sub-option also allows for quenching due to cold walls. FGM is limited to two inlet streams which can be any mixture of fuel and air [20]. The limitation does not affect combustor analysis as only two inlets are required: one for air and the other for fuel.

2.3.4 Grid Structures

When constructing a computational model, there are two main grids to choose from: structured and unstructured. In a structured grid, each node is related to its neighbors in each dimension through a direct connection, resulting in a structured network. Cells in a structured grid can appear as rectangles (2D) or hexahedra (3D). Structured grids are most useful for finite differencing schemes due to the relationships between neighboring nodes. Unstructured grids can be created with many different cell shapes to include tetrahedra, prisms, pyramids, and hexahedra. Unstructured grids are most useful for finite volume formulations, where the control volume is the cell structure [21].

Often, a hybrid grid is used with models that contain complex geometries. Figure 8 shows an example of a hybrid grid around an airfoil. Structured grids are used close to the wall of bodies to capture the viscous effects using turbulence models. This will also allow for accurate modeling of heat transfer at the wall. Then, unstructured grids are used farther from the wall to fill the remaining volume where a structured grid is not necessarily required [21]. A hybrid grid provides both the $k-\omega$ SST turbulence model and the partially premixed combustion model with the proper computational model for analysis of combustors.

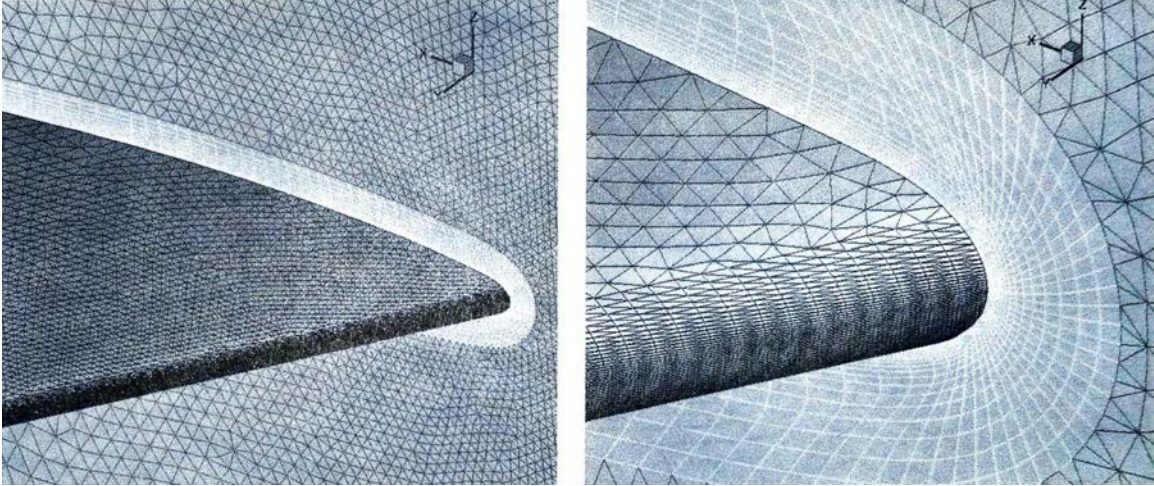


Figure 8. An example of a hybrid grid around an airfoil [21].

2.3.5 Computational Modeling of Combustors

Both Briones et al. [17] and Bohan et al. [2] [3] utilized CFD to model the complex, volatile combustion environment. Briones et al. validated and expanded upon previous experimental research by Lewis [16] with FLUENT. This allowed Briones et al. to visualize the combustion processes related to high-g combustion, including flame front propagation, a difficult task to accomplish experimentally. Bohan et al. utilized CFD as a design tool. CFD allowed Bohan et al. to rapidly examine multiple design iterations of a UCC for use within a JetCat P90 RXi. With this information, Bohan et al. selected several designs for experimentation and validated CFD results with physical hardware [1].

2.4 Combustor Exhaust Metrics

Due to the high temperatures of modern combustors, turbine blades need relatively even temperature distributions to preserve blade integrity. When hot spots are introduced, turbine blades experience thermal deformations. Therefore, post-

combustion mixing with dilution air is often required for the combustor exit gases to provide a reasonable temperature distribution to the turbine section [6].

A circumferentially averaged temperature profile examines a combustor's exit temperature from the inner diameter to the outer diameter around the exit's circumference, and can be seen in Figure 9. This provides insight to where the maximum temperature resides on the exit profile and the temperature differences seen by the turbine. Samuelsen [6] discusses that the maximum temperature on the profile presented to the turbine should occur close to the midspan but slightly outboard. This peak temperature location allows for maximum power extraction while keeping both the hub and tips of the turbine blades cool and resistant to material deformation.

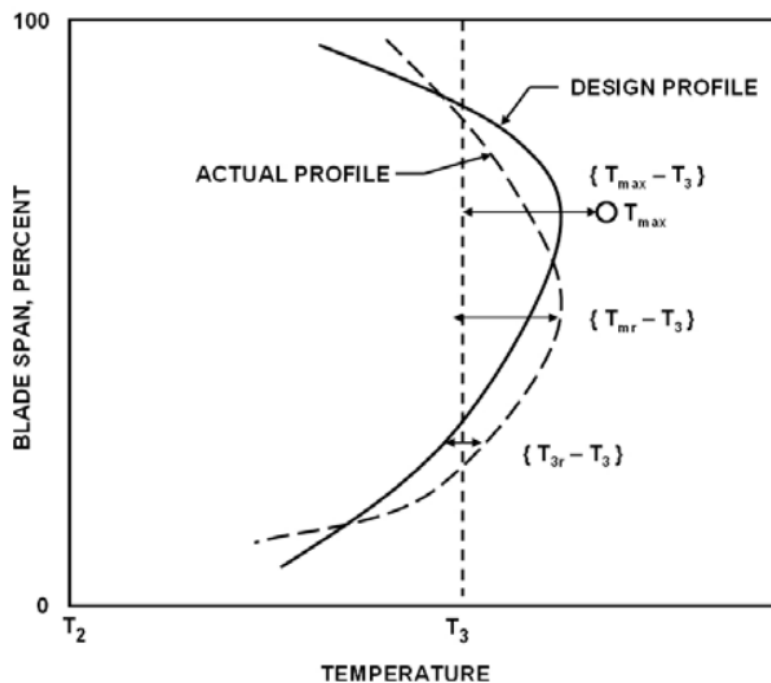


Figure 9. Combustor exit temperature profiles [24]

The pattern factor (PF) helps to determine the temperature uniformity of the combustor exit temperature profile in the transition to the turbine section. Pattern

factor is calculated using the combustor maximum total exit temperature (T_{tmax}), average total exit temperature (T_{t4}), and average total inlet temperature (T_{t3}) using Equation 9.

$$PF = \frac{T_{tmax} - T_{t4}}{T_{t4} - T_{t3}} \quad (9)$$

Traditionally, good pattern factor values ranged from 0.2 to 0.45, but with advancements in combustor design and increased exit temperatures values have become more restrictive with a range from 0.15 to 0.25 [4].

Previous small engine UCC research [2] [1] incorporated pattern factor as a measure of combustor viability. When the pattern factor matched the recommended ranges and the exit profiles matched those discussed by Samuelson [6], the combustor's exit profile was considered acceptable for a rotating turbine. Experimentally, Bohan [2] determined pattern factor with a radial thermocouple probe on a circumferentially traversing rake, with PF values of 0.15 and 0.16. The results were used to generate Figure 10, an exit temperature contour, and show a temperature distribution similar to the desired case.

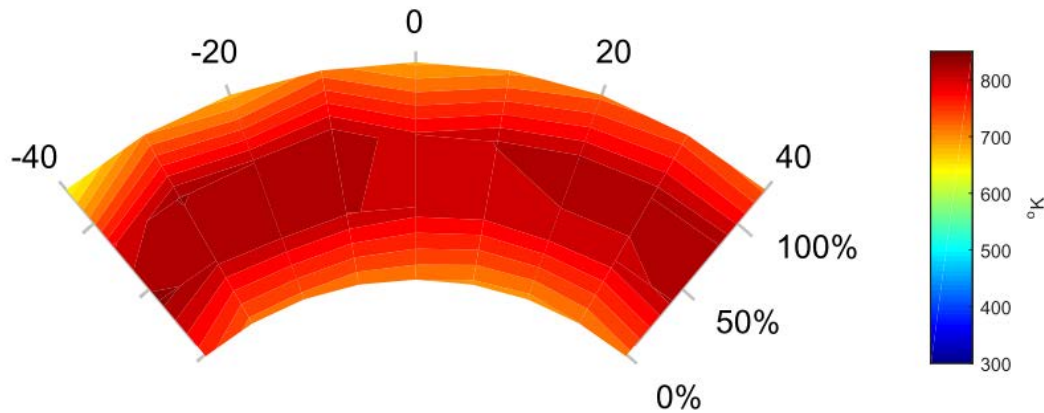


Figure 10. UCC experimental exit contours [3].

When calculating pattern factor from CFD results, an individual cell's maximum temperature may exceed that of the surrounding cells, resulting in an abnormal temperature spike. This condition is not seen experimentally as the temperature differences are gradual across small areas and continuous. CFD presents discontinuities that result in unreasonable cell values. To resolve this issue, the exit plane can be broken up into equal sections and each section can be averaged, then the maximum average is used as the maximum temperature for the exit region. This allows for a more accurate pattern factor calculation from CFD that more closely matches experimental values [25].

III. Methodology

The present research looked to design a new Ultra Compact Combustor (UCC) for use in the JetCat P90 RXi, shown as a cutaway in Figure 1, to operate at full power in a self-sustained mode, while achieving a 33% length reduction from the stock combustor. The flow path through the JetCat P90 RXi followed the arrows as depicted in Figure 1, where the air was compressed by the annular compressor, which then flowed into the dump diffuser and burned in the combustor with kerosene as the fuel. Once the fuel-air mixture burned, the mixture traveled through the turbine nozzle guide vane to set up the appropriate flow angle to drive the axial turbine and exit through the nozzle. The existing hardware had several constraints for the UCC including: an engine casing diameter of 107.5 mm, an engine shaft cowling that drove the inner diameter of the combustor annulus, an annular interface with the turbine nozzle guide vane consisting of an inner diameter of 42.7 mm and an outer diameter of 68.8 mm, and the fuel delivery system. These constraints drove the design of the new UCC with one exception, the new UCC used propane instead of kerosene for its fuel, due to propane's ease of control and availability.

The JetCat P90 RXi was used as the test bed for this research due to its simple design and use by Bohan et al. [1][2]. The UCC replaced the stock combustor and was required to integrate with the existing JetCat P90 RXi hardware discussed above. Bohan et al. previously tested the UCC in the JetCat P90 RXi and established existing hardware for future testing. This equipment is discussed further in Section 3.1. Computational analysis in the form of CFD was used to analyze several design iterations, the set up of which is discussed in Section 3.3. Each design iteration was generated using the Computationally Aided Design (CAD) program called Solidworks 2018. This CAD software allowed for rapid design changes when CFD results showed design flaws or unfavorable characteristics. The changes made between iterations

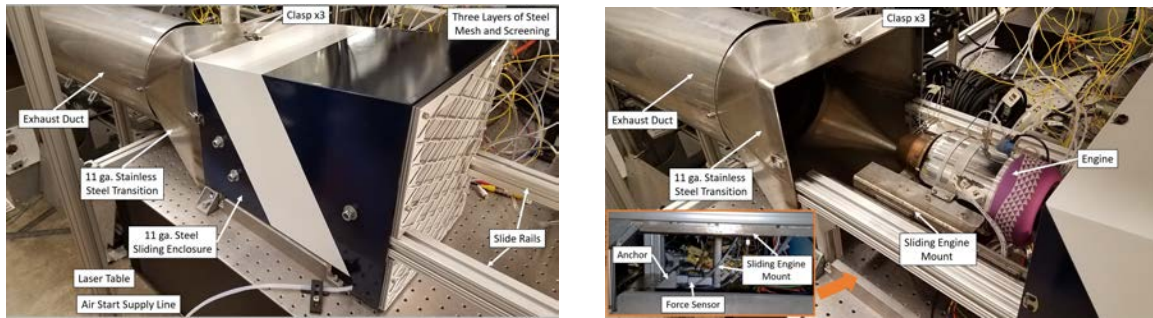
varied from shaping walls to rearranging dilution hole placements and is discussed later in Section 3.2. Once a final design was decided upon based on the CFD results, physical hardware was built. A circumferential, metal, engine-scale combustor was manufactured for reacting flow tests and integrated into the JetCat P90 RXi. Section 3.4 describes the physical hardware fabrication and integration process. The Air Force Institute of Technology (AFIT) Combustion Optimization and Analysis Laser (COAL) lab facility that allowed for this experimentation is discussed in Section 3.5 and the instrumentation and uncertainty analysis is covered in Section 3.6.

3.1 Previous JetCat P90 RXi Combustor Testing

Bohan et al. [1][3] tested their small engine UCC in the COAL laboratory on the AFIT campus. An in depth description of the set up was presented by Bohan [3] and a summary will be presented here. The experimental testing was done in two stages: a non-rotating and a rotating configuration. The non-rotating configuration was run in the non-rotating test stand with force fed air from the lab's compressed air supply. This configuration replaced the engine radial compressor with a smooth body to avoid rotating hardware and the turbine was removed. This allowed for the combustor to be studied with more instrumentation that would not be available in a rotating configuration, to include a thermocouple rake placed behind the turbine nozzle guide vane to determine exit profiles and pattern factor. Both configurations had propane fed to them through a manifold connected to the lab propane supply.

Figure 11 shows the engine test stand that was used for the Bohan et al. rotating turbomachinery testing. This configuration used a jet of air directed at the engine compressor to spool up the engine and start it. The engine stand was instrumented to measure engine thrust and the engine was instrumented to take pressure and temperature measurements at each engine station, with Station 4 measurements taken

before the nozzle guide vane assembly. All instrumentation was routed to a computer running LabView. The same computer also controlled the air flow rate to the non-rotating configuration and the fuel flow rate to the engine for both configurations.



(a) Enclosure in the closed configuration for running tests on the JetCat P90 RXi.

(b) Enclosure opened to access the engine and instrumentation.

Figure 11. Experimental engine test stand.

3.2 Combustor Design Iterations

The goal of this research was to design a JetCat P90 RXi UCC that would operate at the design condition in a self-sustained mode. In total, over 20 iterations were designed with the intent to accomplish this goal. This section covers the major points through the design process of the UCC and how the final version was arrived at.

The initial designs for the UCC involved dividing the combustor physically into a primary and a secondary zone with a constricted channel between the two, as seen in Figure 12. This form followed from the research conducted by Bohan et al. [1] in which the combustor had a centrifugally loaded primary zone with an axial secondary dilution zone, shown in Figure 7, to complete the burning process and prepare the flow for the axial turbine. The division of the UCC into the two zones went through two major phases in this research. The first phase involved a curved wall extending

from the outer diameter of the combustor with a small ramp and constriction close to the inner diameter, as seen in Figure 12a. This design allowed for a large bulk swirl in the primary zone due to the physical barrier from the secondary zone. The swirl in the primary zone was good at achieving high reaction temperatures and mixing the reactants. In addition, the propane fuel was introduced by way of injection jets from a plenum in the outer wall. However, when the flow traveled through the constriction to the secondary zone, it did not fill the secondary zone volume and simply left the combustor through the nozzle guide vanes.

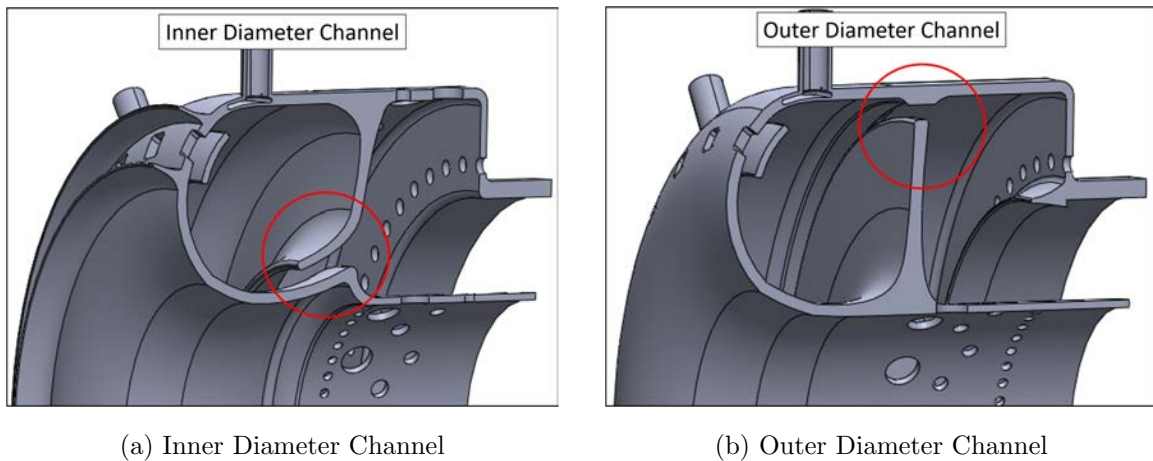


Figure 12. Transition from inner diameter channel to outer diameter channel.

The undesirable flow path in phase one led to the second phase of the chamber division designs, where the transition channel was moved to the outer diameter of the combustor, shown in Figure 12b. The placement of the channel on the outer diameter was meant to force the flow to fill the secondary zone volume, continue reacting, and then exit through the nozzle guide vane. Through this design's analysis cycle, dilution hole placements were changed, the transition gap was widened, several configurations of cooling holes for the center wall were attempted, and holes were added in the hopes of keeping flow attached at certain locations. In total, the main fault with this design

was the large pressure losses incurred through the combustor. Figure 13 shows total pressure contours on the center plane of the combustor for one of these iterations. The large low pressure region behind the center dividing plate, circled in Figure 13, resulted in unrecoverable pressure losses for this design. Ultimately, the primary zone cavity in this design performed well, however the pressure losses due to the dividing plate and the rapid flow constriction in the channel resulted in the need for a different design moving forward.

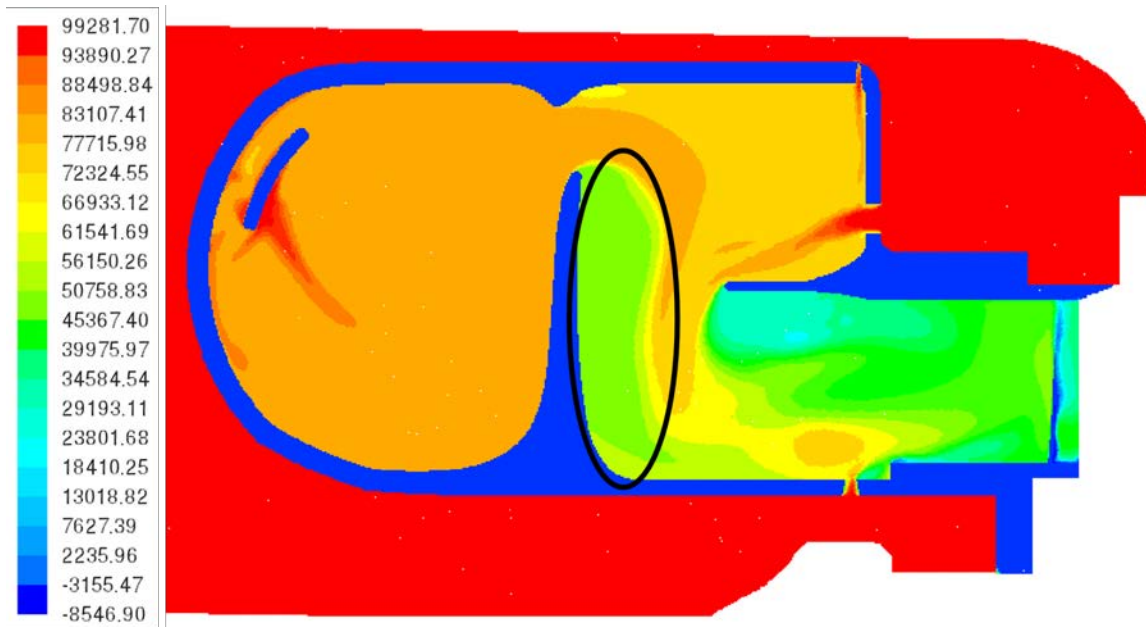


Figure 13. Computational result of a cutaway from an early outer diameter channel UCC model with total pressure contours.

The next design moved away from the two zone idea and removed the physical barrier in the center of the combustor as shown in Figure 14. This iteration followed the design of conventional gas turbine combustors with one large cavity and many dilution holes. The difference in this design from conventional combustors came from the inlets on the forward curved dome and the impingement plate behind these inlets. The inlets provided air directly to the primary zone of the combustor. They

allowed for control over the amount of air that initiated reactions with the fuel. The inlets were sized such that at the design point, 20% of the air exiting the compressor would flow through 24 inlets in the forward dome. The 20% split allowed for a rich fuel-air mixture to be present in the primary zone. The impingement plate followed the contour of the forward dome and was spaced 2.75 mm from it with an inner diameter of 76 mm, an outer diameter of 91 mm, and a thickness of 0.508 mm. The plate was placed in the primary zone to reduce the incoming air velocity and allow for combustion to occur. The impingement plate acted as a bluff body where a recirculation zone would form behind it and provide a flame holder for the combustor. In addition, the plate split the primary zone inlet air such that it would flow along the walls of the combustor rather than act as strong jets penetrating into the combustion chamber.

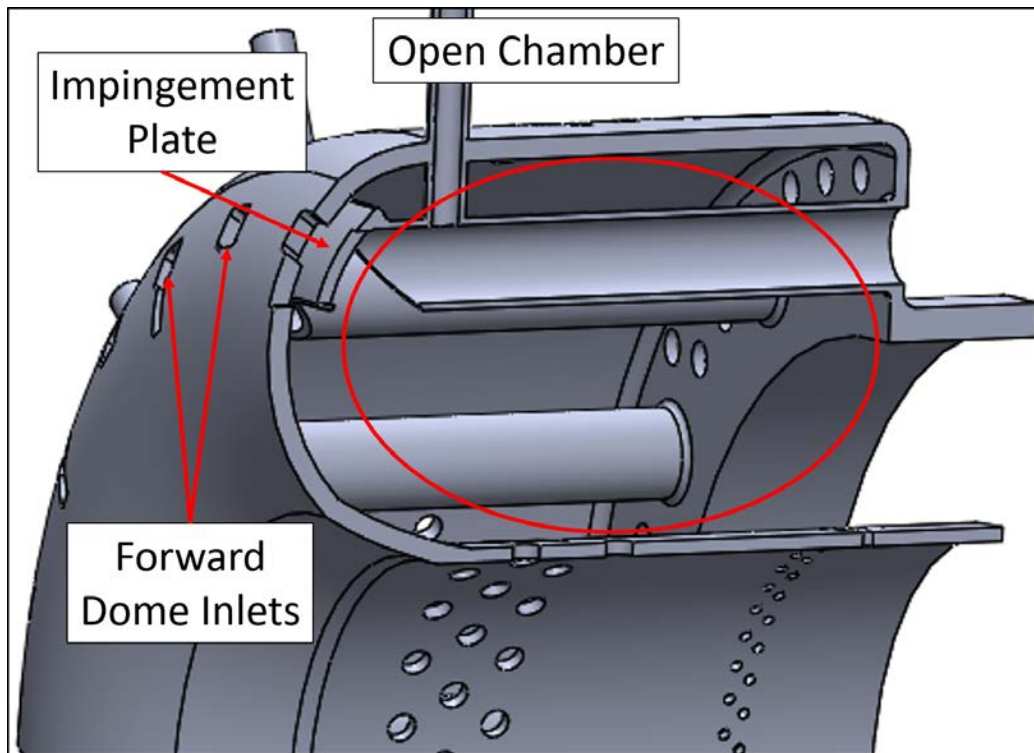


Figure 14. Open chamber design of the UCC for the JetCat P90 RXi.

Figure 15 introduces the final design integrated into the JetCat P90 RXi, a finely tuned version of the open chamber design shown in Figure 14. The core air flow left the radial compressor and entered the dump diffuser plenum to the combustor. Here the air split three ways: part of the air entered into the combustor through the primary zone air inlets on the forward dome, part went to the outer diameter of the combustor, and part went to the inner diameter. The air that entered through the inlets, placed at the stagnation point on the forward dome of the incoming compressor air, impinged on the plate there and split to the outer and inner diameter flow paths around the plate. These paths helped set up the recirculation zones on either edge of the plate to act as flame holders.

On the aft side of the plate, a propane-air mixture exited the fuel-air mixing tubes. The propane inlet was fed externally, as depicted by the green arrow in Figure 15, while the air entered through the aft of the combustor, like a reverse flow combustor, as shown by the purple arrow. The fuel-air mixture burned off of the flame holders at the impingement plate and the mixture continued to burn axially through the length of the combustor while being fed by dilution holes, sized to 2.0 mm in diameter, on the inner and outer diameters of the combustor. The dilution holes on the inner diameter were staggered and spaced 5.0 mm apart to allow for flames to anchor in between them. On the outer diameter, a similar pattern was followed with 6.0 mm spacing, but the holes were not placed above the fuel-air tubes such that the tubes would maintain hot surface temperatures. The hot tubes would allow future combustor iterations to switch to kerosene fuel, where the tubes would vaporize the liquid fuel. Finally, the hot reaction products exited the combustor through the nozzle guide vane and drove the turbine. The computational and experimental results analyzing this final design are presented in Chapter IV.

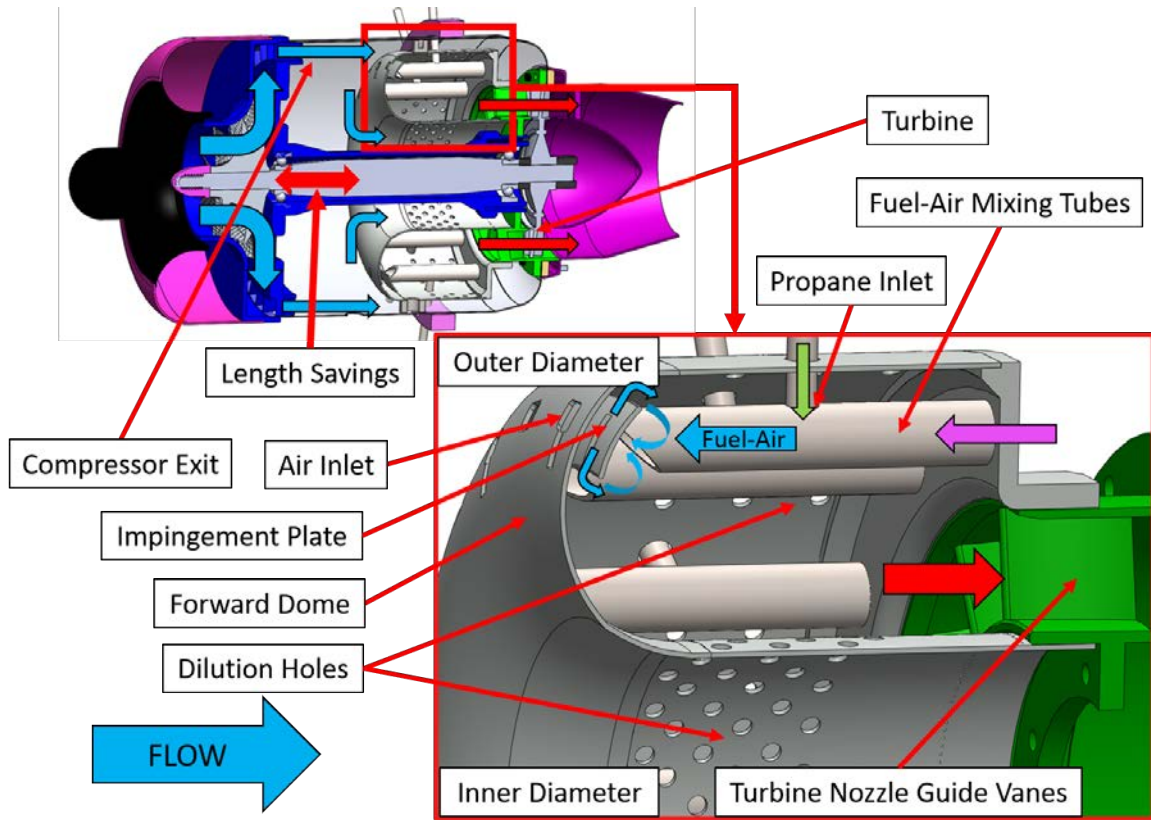


Figure 15. JetCat P90 Rxi final combustor design integrated into the engine.

As discussed in Section 3.1, Bohan et al. [1] experienced problems with their combustor due to the small combustor volume, which was a major point of influence for the present research. Figure 16 shows a side-by-side comparison of the Bohan et al. combustor, Figure 16a, and the present research's combustor, Figure 16b, with both combustors integrated with the engine case (grey), turbine nozzle guide vane assembly (green), and the engine centerbody (blue). The fluidic volume of both combustors were found from the Solidworks models to be 199 and 263 cubic centimeters, respectively, with the new combustor resulting in a 32% increase. The increased volume was possible due to the flame stabilization provided by the impingement plate, which allowed the UCC to move away from step-stabilization and the need to turn the flow circumferentially. The step-stabilization technique was not conducive to the space

requirement at this small-scale. Additionally, the new combustor contained no flow constrictions that would increase the flow’s velocity and quench reactions. Both the increase in volume and the lack of flow constrictions made the velocities inside of the combustor favorable for combustion to occur.

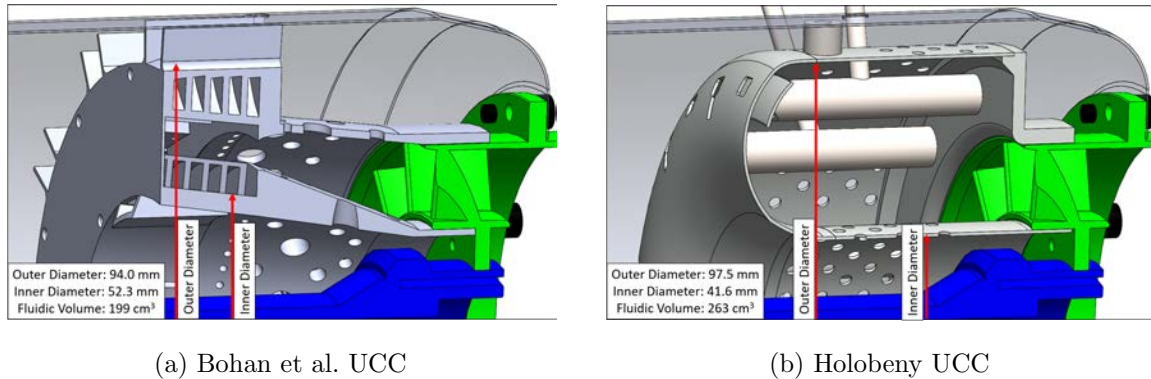


Figure 16. Cutaways of the JetCat P90 RXi UCC from Bohan et al. and the present research with engine casing and centerbody included.

The new JetCat P90 RXi UCC design shortened the combustor length relative to the stock combustor by 33%, similar to the Bohan design. While the stock combustor was removed, the remaining hardware of the JetCat P90 RXi was intended to be integrated into the UCC design as much as possible. However, one additional change from the stock design was implemented. The stock fuel delivery system used kerosene to start and run the engine. This research looked to propane as its fuel source, for two main reasons: ease of access in the AFIT COAL lab and propane’s ease of control for varying mass flow rate. Propane was initially incorporated into the design using a plenum in the outer wall of the combustor. This plenum introduced propane into the combustor through shear jets that mixed with incoming primary zone air. However, a new fuel delivery system was designed that would utilize propane fuel now but provided the potential to switch to kerosene in the future. This system

mimicked the stock combustor’s fuel-air mixing tubes, with slits in the forward dome and impingement plate to allow for liquid fuel injection. When using propane, the fuel-air mixing tubes received propane from tubes inserted through the engine casing and the combustor outer diameter. The propane tubes injected gaseous propane into the fuel-air mixing tubes, where the fuel-air mixture heated up from the surrounding reactions and deposited behind the impingement plate. If kerosene were to be used, the engine’s fuel manifold would deposit kerosene in the fuel-air mixing tubes with hooked hypodermic tubes. The heated fuel-air mixing tubes would then cause the liquid kerosene inside them to vaporize, fueling the recirculation zones.

3.3 Computational Analysis Setup

Computational analysis was used to analyze combustor designs at the full power and off-design conditions prior to fabrication. This section outlines several key steps involved in the computational analysis process of the JetCat P90 RXi UCC and follows closely to the process in Section 8.3 of Bohan [3]. First, the Solidworks model was imported into Pointwise (Version 18), where the computational domain was generated. Section 3.3.1 develops the grid generation process for the computational model. From Pointwise, the domain was converted to a case file for ANSYS FLUENT 17.2. The FLUENT user interface was utilized to set up the CFD case for the design and off-design conditions. Setup included applying boundary conditions, choosing solvers and models, and determining other various settings that are discussed in Section 3.3.2. To ensure that the CFD results were not influenced by the grid generation process, a grid independence study was then conducted. The study included three computational grids for the same model design, but with varying cell counts and density. Section 3.3.3 shows that the solution was grid independent.

3.3.1 Grid Generation

The computational grid was made to capture the fluid flow path from the compressor exit to the turbine nozzle guide vanes incorporating the engine case and centerbody. Each iteration of the Solidworks combustor model was adapted for CFD before being exported to Pointwise. Figure 17 shows a section view of a scale combustor model created using the CAD program. The models used for CFD needed to have the engine casing surrounding the combustor in place, as shown in Figure 18. To accomplish this, a simple sketch of the engine casing and centerbody were drawn around the combustor, matching the JetCat P90 RXi geometry. Including the engine casing around the combustor allowed for boundary conditions to be set that matched the known exit conditions of the compressor. This allowed FLUENT to solve the combustor inlet and dilution hole flow conditions rather than having user defined inputs. In addition, the turbine nozzle guide vanes needed to be included so that the flow conditions at the turbine station would be accurate. Once these two pieces were integrated into the Solidworks model, a negative of the model was created. This step was useful in generating a database for Pointwise, where the database lines would be generated on the model's surfaces.

Lastly, due to the periodic nature of circumferential combustors, the model was cut into a 30° wedge. This wedge was periodic around the centerline of the engine twelve times, to complete a 360° rotation. The stock engine had a turbine nozzle guide vane that consisted of 15 vanes and in order to keep the computational model simple only one guide vane was modeled, implying that the computational model only had 12 vanes rather than 15. During experimental testing, the 15 vane nozzle guide vane was used. The only difference in these two vane counts would be smaller vane passages in the experimental testing with higher gas velocities.

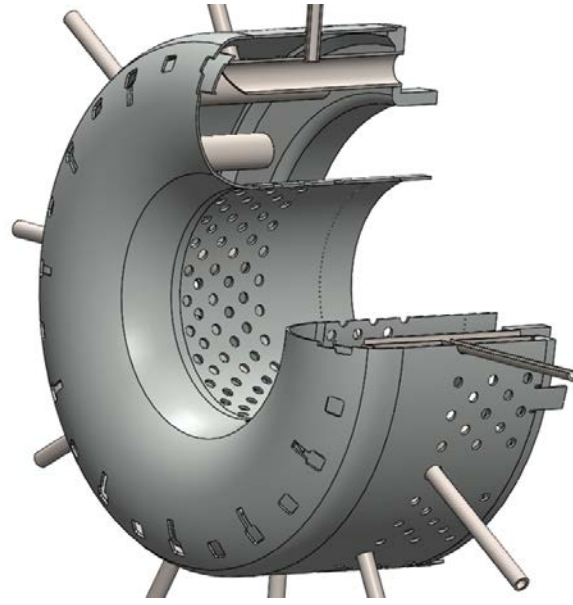


Figure 17. UCC Solidworks model.

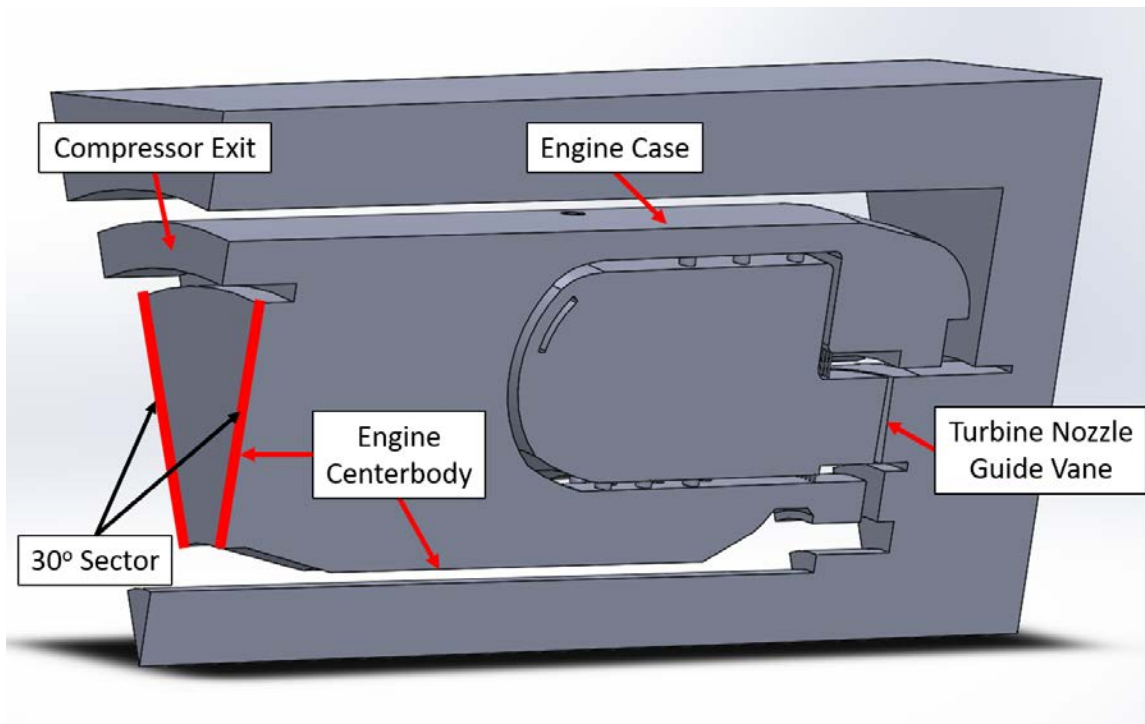


Figure 18. UCC Solidworks model used for CFD incorporating the compressor exit, engine case and centerbody, and turbine nozzle guide vanes.

When the necessary steps in Solidworks were completed, the file was saved in the Initial Graphics Exchange Specification (IGES) format and imported into Pointwise as a database. In Pointwise, the connectors on the combustor walls were placed with a node spacing of 0.127 mm, while the case connectors used a 0.762 mm spacing. The connectors that joined the two areas were distributed to provide a smooth transition. The domain inside the combustor walls was generated using the Pointwise anisotropic tetrahedral extrusion (T-Rex) tool to ensure proper y^+ off the wall (average of five across the model). T-Rex generates a hybrid grid as discussed in Section 2.3.4. The modified settings for the fluid T-Rex domains included setting: max layers to 10, full layers to 10, growth rate to 1.2, cell types to triangles & quads, and a establishing boundary condition of “wall” with $\Delta s = 0.0254$ mm for the interior combustor walls. All the fluidic domains and blocks that were generated, inside and outside the combustor, had boundary layer decays of 0.92 where the solid (material) domains and blocks used a boundary decay of 0.8. The computational model incorporated periodic domains on the edges of the 30° rotational sector. In addition, the connectors that fell between the two periodic domains had a node spacing of 0.254 mm. Unstructured domains were used for all remaining domains, with one exception. Domains that wrapped around small rounded edges (fillets) were created using a structured grid, shown in Figure 19, as these did not generate well as unstructured grids.

Once all the domains were generated, the boundary condition types were set. By setting the boundary condition types in Pointwise, the imported case file to FLUENT would recognize the types and provide the proper interface for each one to input conditions. The various boundary conditions are shown in Figure 20 with their corresponding domains. Section 3.3.2 discusses the conditions at each boundary in detail.

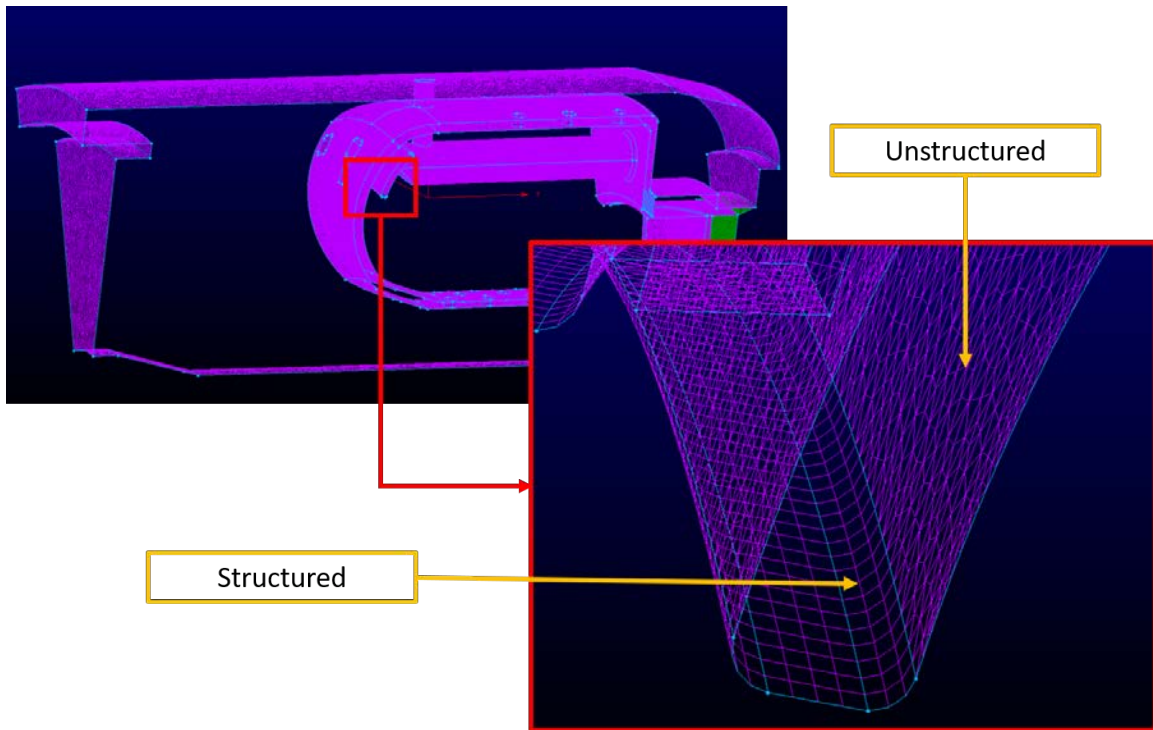


Figure 19. An example domain where a structured grid was required instead of an unstructured grid.

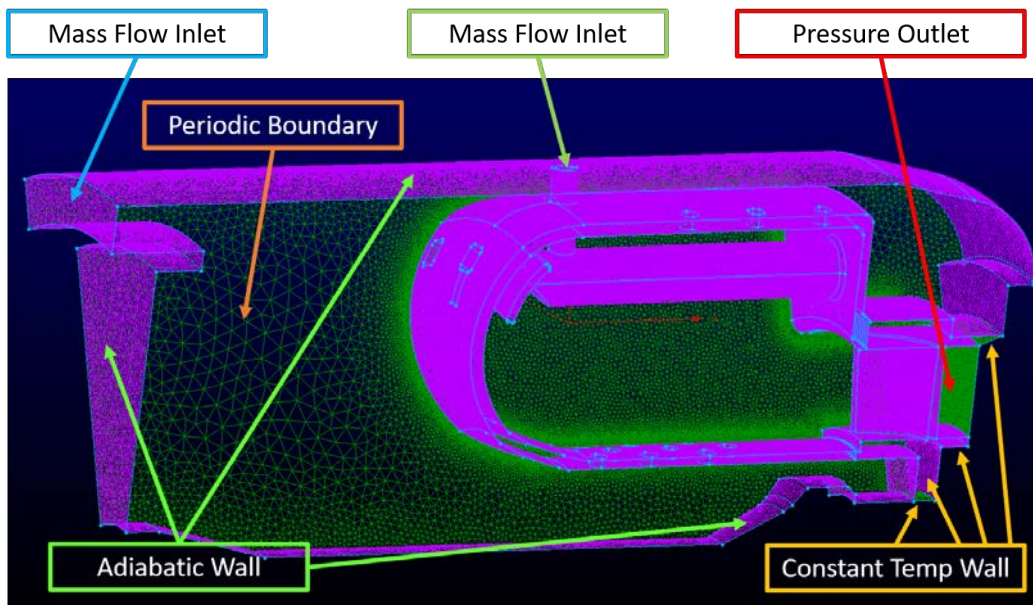


Figure 20. Computational domain with boundary condition types identified.

The domains that formed the surfaces that connected the solid and fluid blocks were assigned the coupled boundary condition by Pointwise. These domains enabled conjugate heat transfer, as discussed in Section 2.3.2. The solid and fluid blocks were created with the auto-generation tool in Pointwise. The solid block was solved using an unstructured block and the default settings (apart from the boundary decay). The fluid block was solved using T-Rex and matching the wall spacing on the periodic boundaries. The hybrid block was applied to the passages of holes and tubes leading into the combustor and the inner walls of the combustor. This would allow for the turbulence model selected to model near wall effects appropriately in the desired analysis areas. The modified settings for the fluid T-Rex block included setting: max layers to 10, full layers to 10, growth rate to 1.2, collision buffer to 2.0, max angle to 160, and establishing boundary conditions of wall with $\Delta s = 0.0254$ mm for the interior combustor walls and a match condition selecting the interior periodic fluid domains.

The combustor model was checked for the average y^+ off the wall, to ensure proper values for the turbulence model. It was found that the average value of five was too high for the $k - \omega$ model that needed a y^+ of one or less. However; the high y^+ values were concentrated in regions where the flow was not of interest to this research and y^+ values close to one were seen in the forward dome, where the highest heat release would occur on the combustor wall. For future iterations, the Δs spacing should be reduced by an order of magnitude to ensure complete y^+ compliance.

The last step before generating a FLUENT case file was to set the block volume conditions. This would allow FLUENT to recognize where the solid and fluid volume existed and to create interior volumes for each, as well as an interface between the two to enable conjugate heat transfer. At the completion of this gridding process, each design iteration generated approximately 14 million cells in the volume.

3.3.2 FLUENT Case Setup

FLUENT was used to determine the performance of a UCC in the JetCat P90 RXi in the configuration shown in Figure 15. The case file that was generated from the process outlined in Section 3.3.1 was read into FLUENT and the user interface was then used to set boundary condition values, choose solution methods and models, and analyze the results.

Figure 21 shows the 30° sector computational domain for the JetCat P90 RXi UCC. Included in the domain are the engine outer case and centerbody (green boundary) as adiabatic walls, an air inlet from the compressor (blue boundary), and the exit into the turbine through the turbine nozzle guide vanes (red boundary). This approach was consistent with Bohan et al. [2].

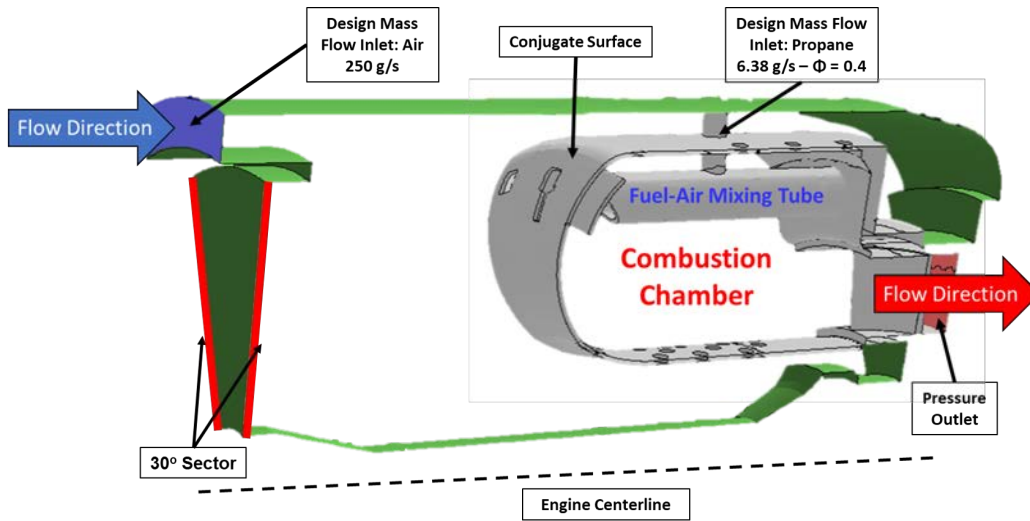


Figure 21. The CFD domain with boundary conditions.

The computational model incorporated conjugate heat transfer on the walls of the combustor. In addition, the combustor walls were modeled as Inconel [26], with the same material properties as would be used in production. Combustion events were modeled using a partially premixed propane-air mixture with flamelet generated

manifold and diffusion flamelets, to match the methods employed by Bohan et al. [2]. As discussed in Section 2.3.3, this model could predict quenching due to wall contact and dilution jets, which worked well with the addition of conjugate heat transfer at the walls of the combustor model. The GRI-Mech chemical kinetic mechanism files were used to provide the necessary information for FLUENT to generate a probability density function of species for chemical reactions. The solution was run using a pressure-based steady-state solver and turbulence was incorporated using a $k - \omega$ Shear Stress Transport (SST) turbulence model, which was selected for its success with wall-bounded flows and heat transfer [3]. More information on the models used can be found in Chapter II.

Before calculating the solution, hybrid initialization was used to set the case up for a smoother start. The initialization process was set to use initial pressures on the air and propane inlets, which were both set to 5,200 Pa gauge. When the initialization process was completed, the solution was calculated out to 3000 iterations, with saves being done every 250 iterations, to check variations in the solution data due to the combustion model. In addition, monitors were set for average temperature and velocity at the exit plane to track changes across iterations. The monitor data for three runs at the design condition is displayed in Figure 22. These three runs contained different grid resolutions for the grid independence study, discussed in Section 3.3.3. The monitors showed that the solutions fluctuated continuously; however, all the fluctuations, after the first 100 iterations, fell below a 12% difference about the mean. Considering the unsteady nature of combustion there was variation between iterations making the steady state solution oscillatory. Solutions were usually run out to 3000 iterations to gather more fluctuation data.

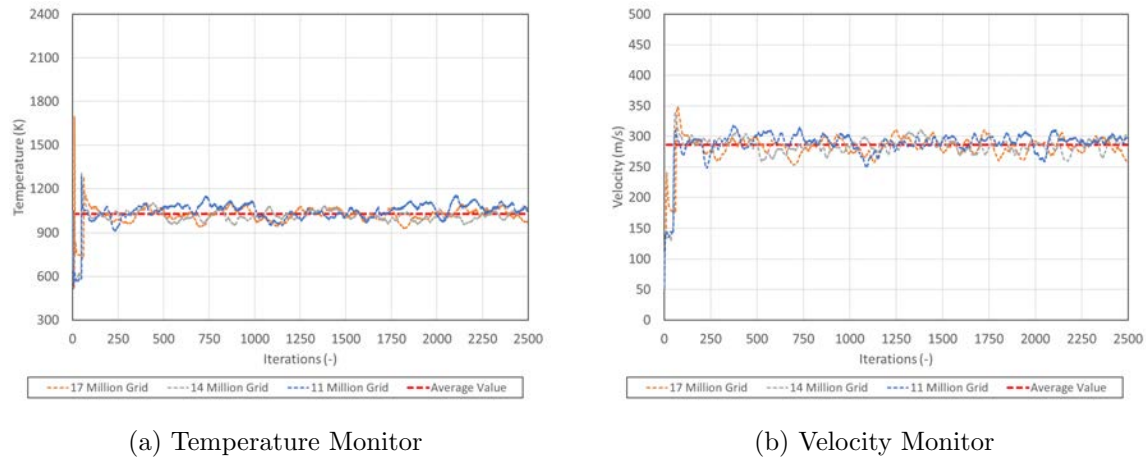


Figure 22. Monitor data taken at the nozzle guide vane exit for three different grids at the design condition.

The final combustor design was analyzed at three main engine conditions chosen to match the stock engine data made available by Mr. Jacob Wilson: idle, mid-power, and the design condition. The previous combustor geometries were all analyzed only at the design condition. The design condition consisted of an air mass flow rate inlet of 250 g/s (20.83 g/s per sector) at 375 K. A pressure outlet was placed at the exit to the turbine section with an initial back-pressure of 5% of the operating pressure of 253 kPa. Propane was introduced to the combustor at a mass flow rate of 6.38 g/s (0.532 g/s per sector), resulting in a global equivalence ratio of 0.4. The design condition was chosen as it was close to a cruise-like condition for the engine at an engine speed of 100,000 RPM. The idle condition had an air mass flow rate of 70.2 g/s (5.85 g/s per sector) at 310 K, an operating pressure of 110 kPa, and a propane mass flow rate of 1.525 g/s (0.1271 g/s per sector), resulting in a global equivalence ratio of 0.34 and a relative engine speed of 36,000 RPM. The drop in equivalence ratio was representative of the conditions observed in the stock JetCat P90 RXi. The mid-power condition had an air mass flow rate of 157.2 g/s (13.1 g/s per sector) at

345 K, an operating pressure of 152 kPa, and a propane mass flow rate of 4.428 g/s (0.369 g/s per sector), also with a lower equivalence ratio of 0.335 and a relative engine speed of 61,000 RPM.

3.3.3 Grid Independence Study

The computational grid used for the solution contained 14 million cells. The solution was checked for grid independence by running cases with 20% more and 20% less cells at 17 million and 11 million cells, respectively. Lines were placed along the geometry of the combustor in four locations, as shown in Figure 23, to evaluate velocity profiles across each grid resolution.

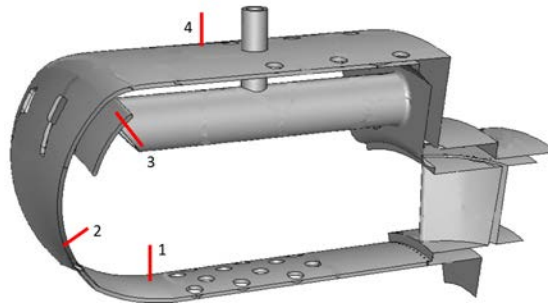


Figure 23. The four lines used to determine grid independence.

The velocity profiles for Lines 1 and 4 are shown in Figures 24a and 24b. Of the four lines, three (Lines 1-3) were placed in areas of the combustor where combustion occurred, resulting in non-uniform profiles across converged iterations, due to the unsteady nature of combustion. To mitigate the unsteadiness, the profiles were averaged across several iterations to eliminate fluctuations and allow for a proper comparison. All of the four line profiles of the 14 million and 17 million cell grids matched closely with only 4.2% maximum variation in profiles, and the 11 million cell grid matched within 18% of the 14 million. There was only 1% maximum variation for the non-combusting profile across all three grids. In addition, temperature pro-

files were evaluated on Line 4, in the non-combusting region. Figure 24c shows the temperature profiles on Line 4 and confirms that there was little deviation between grid sizes regarding temperature in non-combusting regions. Therefore, the 14 million cell grid was chosen for computational analysis to save computational expense when compared to the 17 million cell grid.

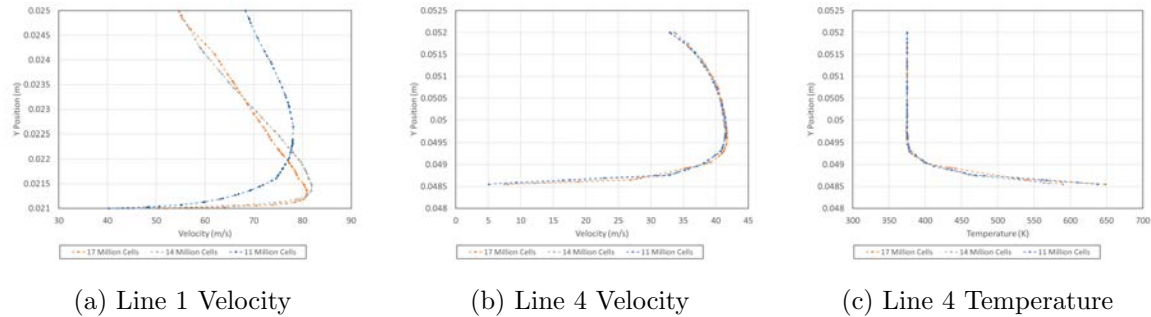


Figure 24. Velocity and temperature profiles from the grid independence study.

3.4 Physical Hardware Production

Once the computational analysis of the new UCC design was completed, a physical metal model was created to evaluate the computational results through experimentation. The physical combustor was constructed by the AFIT Model shop from the Solidworks model. Figure 25 shows the seven pieces used to build the combustor: the forward dome, the impingement plate, the outer diameter, the inner diameter, the back plate, the 12 fuel-air mixing tubes, the 12 propane feed tubes, and a ring that held the 12 propane tubes in place.

Inconel 600 0.508 mm thick sheet metal was selected as the primary material for the build due to its favorable thermal properties and stainless steel was selected for the pieces that could not be acquired in Inconel or would not see high temperatures to include the propane feed tubes and the holder ring. The back plate of the combustor

was machined out of Hastelloy, a name brand of Inconel, due to its availability and favorable thermal properties.

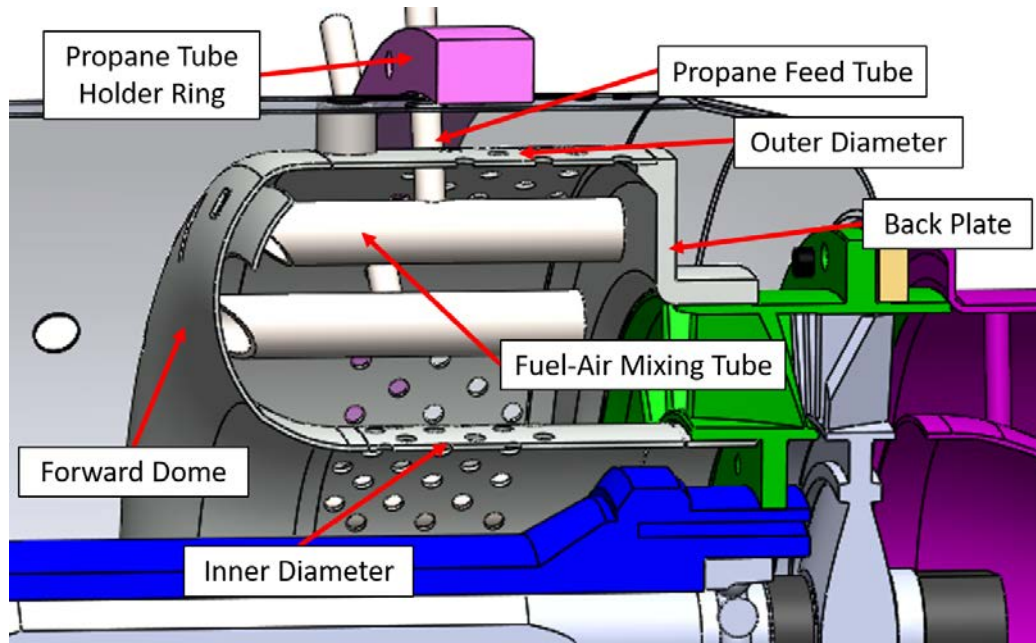


Figure 25. The seven parts used to build the UCC.

In production, a water jet was used to cut the outer shapes and internal holes of the outer diameter, inner diameter, forward dome, and impingement plate as flat sheets. Both the forward dome and the impingement plate were then stamped using a die and press. Figure 26 shows the stamped sheet metal of these two pieces. The stamping process ensured that the curvature of both pieces matched. The inner and outer diameter pieces were rolled such that a weld could be placed along a seam, creating concentric sheet metal hollow cylinders pictured in Figure 27. These two rolled pieces were welded to the forward dome on the inner and outer diameters and mated with the back plate and nozzle guide vane assembly as seen in Figure 28a. The impingement plate pictured in Figure 26b was welded on the tips of the fuel-air tubes, shown in Figure 28b.



(a) Forward Dome



(b) Impingement Plate

Figure 26. Two pieces from the combustor stamped from Inconel 600 sheet metal.



(a) Outer diameter pictured with the back plate and fuel-air mixing tubes.



(b) Inner diameter pictured with the nozzle guide vane assembly.

Figure 27. Pieces from the combustor featuring the two rolled sheet metal parts.

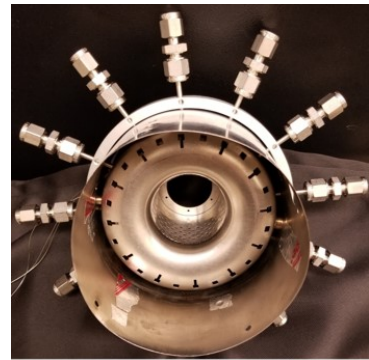
The complete assembly with welded parts and propane feed system is shown in Figure 28c. When assembled, the fuel-air mixing tubes were aligned such that propane feed tubes were inserted through the engine case, through the combustor outer diameter, and into holes in the fuel-air mixing tubes. These propane tubes were held in place by set screws in a holder ring fit over the engine casing. After fabrication and assembly, the combustor, without the fuel assembly, measured 47.5 mm in length (from the forward dome to the back plate) and had an outer diameter of 97.6 mm with an inner diameter of 41.6 mm. The stock combustor had a length of 70 mm, and outer diameter of 95.2 mm, and an inner diameter of 41.4 mm. The new combustor had a mass of 230 grams and was 5.7% lighter than the stock combustor, which had a mass of 244 grams and only six fuel tubes as opposed to the twelve present in the new combustor.



(a) The forward dome with inner and outer diameters welded.



(b) The back plate with fuel-air mixing tubes and impingement plate welded.



(c) The assembled combustor in the engine case with fuel delivery system inserted.

Figure 28. The complete experimental combustor with welded pieces and propane feed system.

3.5 AFIT Facility

This section discusses the equipment that was present in the COAL lab at AFIT at the time of this study. All of the equipment setup that was used for this research was the same hardware and software utilized by Bohan [3] in his investigation of the UCC in the JetCAAt P90 RXi. Bohan discusses the lab’s equipment in Sections 3.1, 8.4.2, and 9.2 as well as Appendices B and D. The lab systems that were utilized in this experimentation included: the compressor air supply, the propane fuel supply, the LabView control station, the UCC rig, and the JetCat test stand. Each of these systems were comprised of multiple parts which are discussed in the following sections.

3.5.1 Air Supply

Both the non-rotating and rotating experimentation utilized the lab’s compressed air supply provided by an Ingersoll Rand H50A-SD compressor and an associated air dryer. Bohan [3] states that the compressor was practically limited to a flow of 0.1 kg/s at atmospheric conditions to allow for constant operation. The compressed air was directed through the lab by the manifold pictured in Figure 29 using the “COAL Supply”. The “AFIT Supply” was an air supply that was shared between multiple labs and was used for the air starter discussed later in Section 3.5.5. Also pictured are four distribution lines with diameters of 7.62 cm, 3.81 cm, 1.91 cm, and 0.635 cm (in order from 1 to 4, of which Lines 1 and 4 were used in testing).

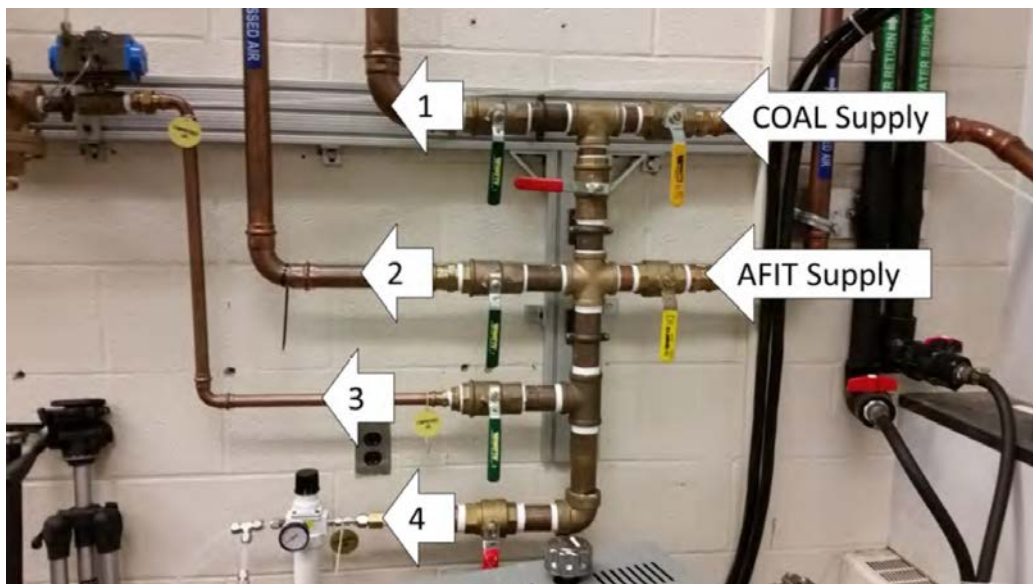


Figure 29. The air supply manifold for the AFIT COAL lab [3].

Line 1 was used for the forced air supply for the non-rotating testing and included a computer controlled pneumatic solenoid valve, a manually controlled pressure regulator, a flow meter, and a computer controlled MaxFlo 3 flow controller (rated to 0.6 kg/s) with an accuracy of ± 3.3 g/s. The flow meter interfaced with the LabView control station via a Eurotherm 2404 PID controller. This line fed to the UCC rig 7.62 cm air supply line adapter that then integrated with the JetCat P90 RXi. The UCC rig is discussed in Section 3.5.4. Line 4 supplied air to the air starter and was controlled by a solenoid to either full on or off, with the pictured pressure regulator controlling the maximum engine speed from the air starter.

3.5.2 Fuel Supply

The COAL lab had access to many fuels via the AFIT fuel farm, but of interest to this study was the gaseous propane fuel supply. The fuel farm housed four liquid propane tanks that fed the lab through two in-line electric Zimmerman LPG liquid-to-gas vaporizers that ensured the fuel was supplied in gaseous form. The fuel flowed

from the fuel farm to the AFIT COAL lab and was directed to an Alicat MCR-250SLPM-D-40X55 mass flow controller capable of flowing up to 200 SLPM with an accuracy of $\pm 0.8\%$ reading. The Alicat was controlled through the LabView control station and fed the engine's propane manifold discussed pictured in Figure 30. The propane manifold had twelve fuel distribution lines arranged on its six sides.



Figure 30. The propane manifold used to fuel the new combustor fed by the Alicat controller.

3.5.3 Control Station

Figure 31 shows the control station with interfaces for the aforementioned air and fuel control systems as well as the yet to be discussed engine glow plug and thermocouple rake. The LabView interface controlled the air supply for the non-rotating testing, the Alicat controller for the fuel supply, the engine glow plug, and was able to display and record the data from the thermocouples and pressure tubes within the engine and the thermocouple rake data. The Raspberry Pi interface controlled

the motors for the thermocouple rake and allowed for circumferential movement of the rake. The CCTV screen allowed for monitoring of the engine testing and provided optical access to the diffuser section upstream of the combustor to watch for flames exiting the front of the combustor.

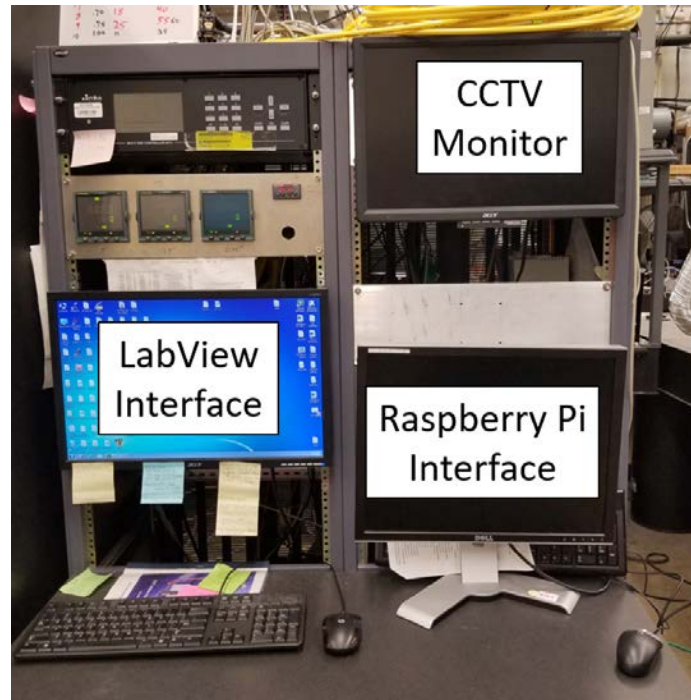


Figure 31. The COAL lab control station.

The LabView interface incorporated two primary virtual instruments (VI), one for the air flow control and thermocouple rake feedback data (*BrianBohan UCC RIG CONTROL11 No Alicat Control*) and one for the engine control systems to include the Alicat flow control and glow plug as well as feedback data for the thermocouple, pressure, and engine speed measurements (*BrianBohan UCC RIG CONTROL7jetcat Auto Start and Shutdown V8*). Both of these VIs were able to record the data displayed on them in addition to their control aspects. *BrianBohan UCC RIG CONTROL7jetcat Auto Start and Shutdown V8* is shown in Figure 32, with the used interfaces labeled and highlighted. This was the same type of VI used by Bohan et

al. [1] [3], but here the engine speed data was collected by a different RPM sensor and required additional VI integration with an Arduino to read the sensor data. The RPM sensor is discussed more in Section 3.5.5.

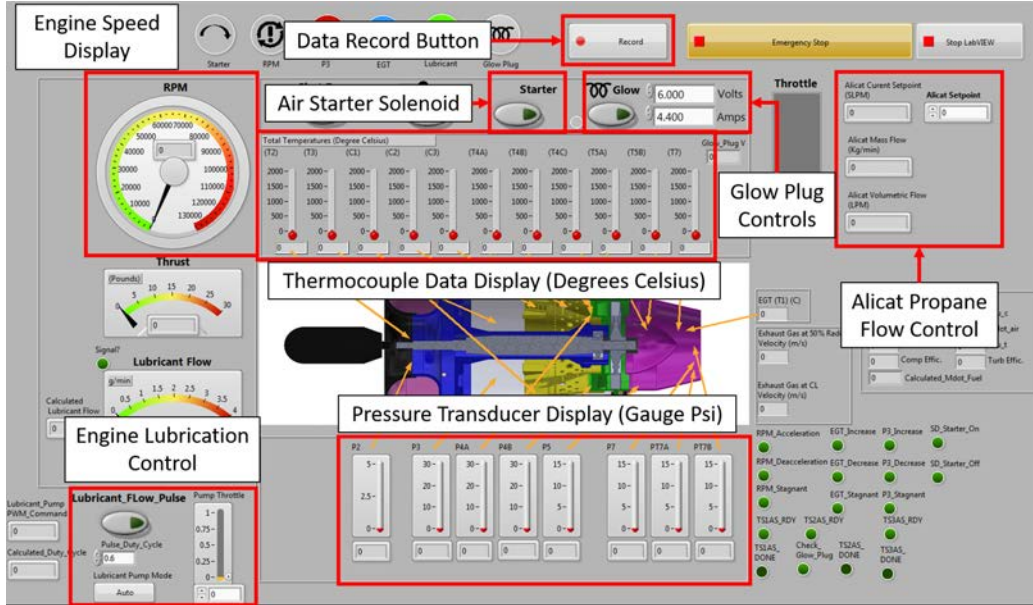


Figure 32. The LabView VI used for the engine control and data acquisitions systems.

3.5.4 Non-Rotating Test Setup

For the non-rotating testing, the engine was supplied with air by the lab’s 7.62 cm line (controlled via LabView VI) that fed the blue tube in Figure 33, which interfaced with the 7.62 cm air supply line adapter mounted to the front of the JetCat P90 RXi. The combustor testing in this configuration was limited to running at or below the engine idle condition of an air mass flow rate of 70.2 g/s at an operating pressure of 110 kPa and a temperature of 310 K. The testing was limited to this condition because the air supply could not reach pressures, mass flow rates, and inlet temperatures for higher engine speed conditions.

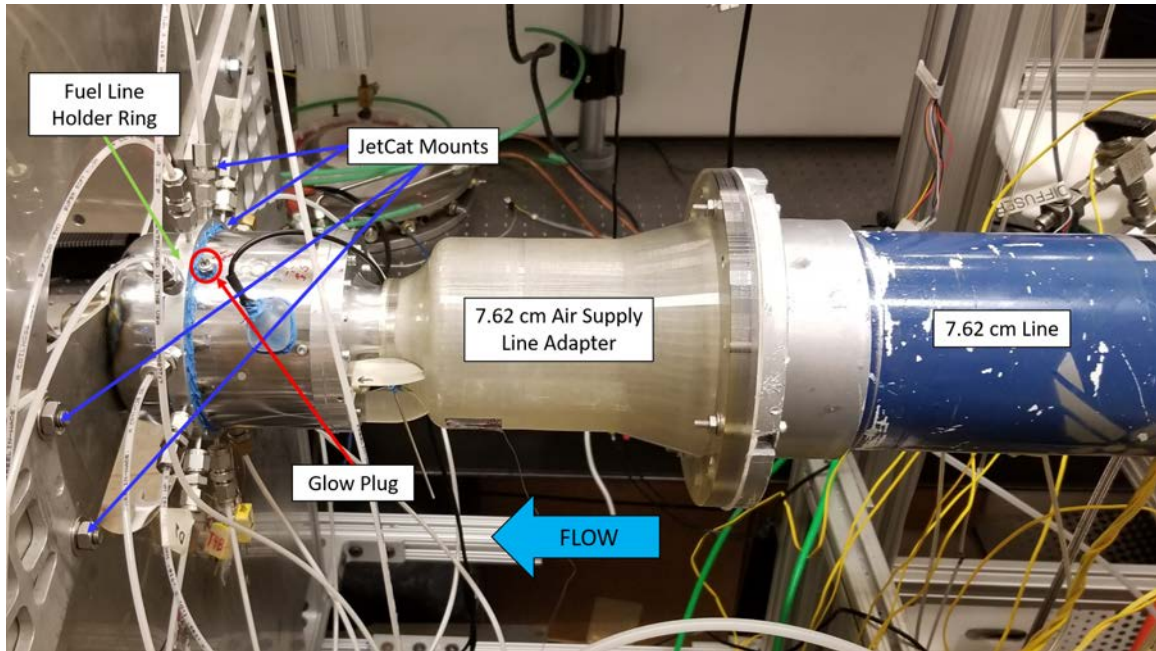
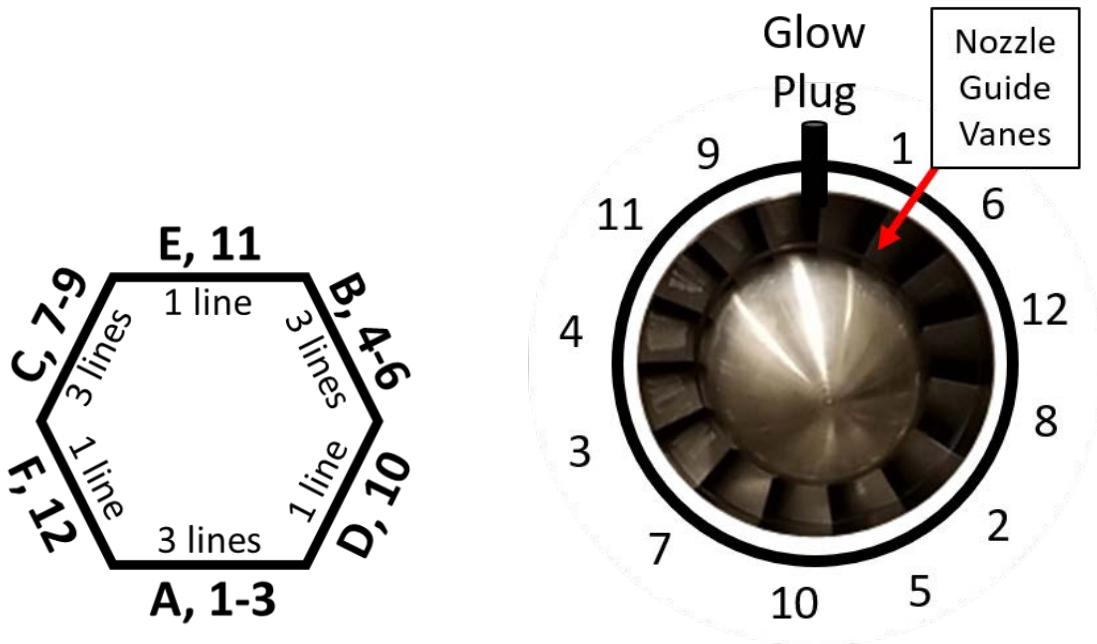


Figure 33. The JetCat P90 RXi installed without rotating turbomachinery.

The engine was attached to the test stand by a mounting plate with four bolts as seen in Figure 33. Also visible in this picture are the 12 propane inlet tubes aligned via the propane tube holder ring. These 12 tubes were fed by the propane manifold discussed in Section 3.5.2. The propane lines exiting the manifold were arranged around the engine such that the fuel entering the combustor was not biased by any one side of the manifold. Figure 34 shows both the labeling method that was used and the line placements for the initial non-rotating testing that allowed for an unbiased fuel distribution.

In this testing, the Bohan [3] custom non-rotating bladeless compressor wheel and non-rotating shaft and tail cone were used along with the stock JetCat compressor shroud, centerbody, and nozzle guide vanes to ensure proper flow paths through the engine. The custom components as well as the air supply adapter and engine mounting plate seen in Figure 33 are pictured in Figure 35.



(a) The labeling and numbering system used for the propane lines that fed the combustor.

(b) The propane line placement around the engine as viewed from the rear of the engine with glow plug and turbine nozzle guide vanes for reference.

Figure 34. The propane manifold line labeling system and configuration for the initial non-rotating testing.

The engine was ignited via a glow plug that screwed into a hole through the engine's outer casing and into the combustor, shown in Figure 36. This was a McCoy MC-9 Glow Plug that required 2.0 volts and 4.4 amps for operation. The power requirements were met via a BK Precision 1688B power supply controlled remotely through the LabView VI.

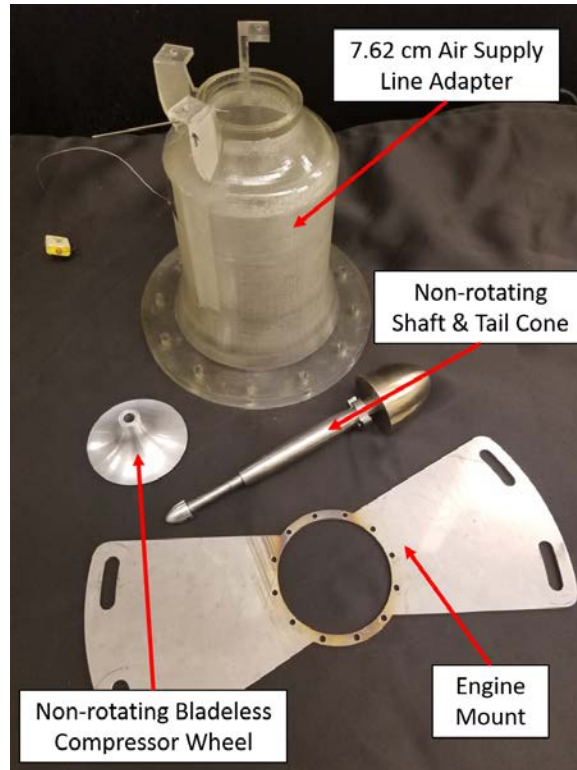


Figure 35. The custom pieces from Bohan [3] that were used during the non-rotating experimental testing.

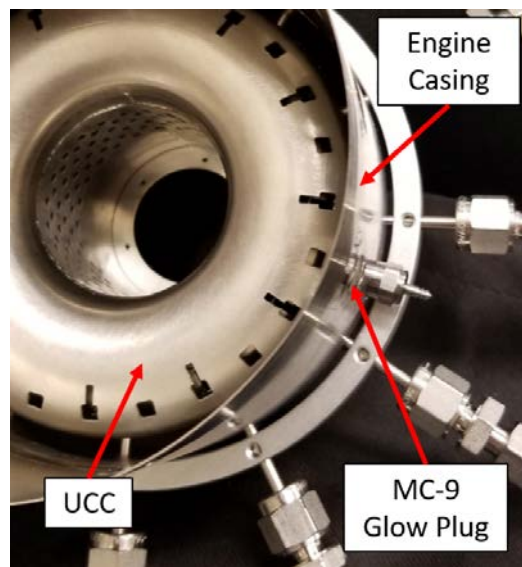


Figure 36. The engine's glow plug placement.

Engine temperature data was collected using Omega K-type sheathed thermocouples (SCAIN-020G-12 for Stations 2-4) connected to the thermocouple panel in Figure 37 that outputted temperature data in degrees Celsius to the LabView VI. The port numbering corresponded directly to the order of the thermocouple measurements in the LabView VI where Channel 2 was T2, Channel 3 was T3, and Channel 7-9 were T4A, B, and C. These channels were used for the non-rotating testing. The locations and accuracy of the thermocouples are discussed in Section 3.6.1.

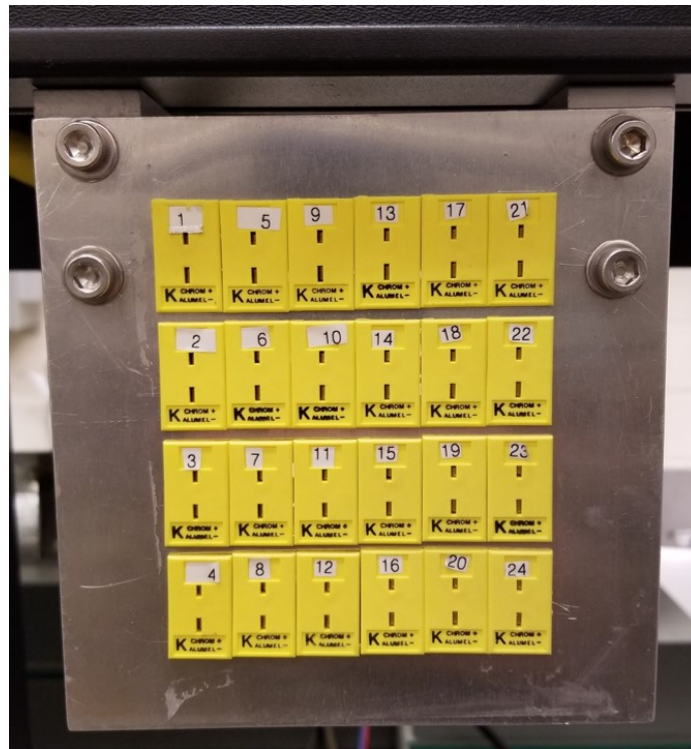


Figure 37. The thermocouple panel used to collect engine temperatures.

Pressure data was also collected from the engine using the pressure transducer assembly that Bohan [3] covers in his Appendix D. Figure 38 shows the assembly and its numbering scheme that corresponded to the pressure measurements in the LabView VI. Three different Omega High Performance Pressure Transducers were used to include a Model PX409-005G5V with a 0-5 psig range (Transducer 1), a Model PX409-

015G5V with a 0-15 psig range (Transducers 2-4), and a Model PX409-030G5V with a 0-30 psig range (Transducers 5-8). Only Transducers 1-4 were used for the non-rotating testing. The pressure transducers were connected to 1.59 mm diameter metal pressure taps in the engine via 1.59 mm diameter tubing. The locations and accuracy of the pressure transducers are discussed in Section 3.6.1.

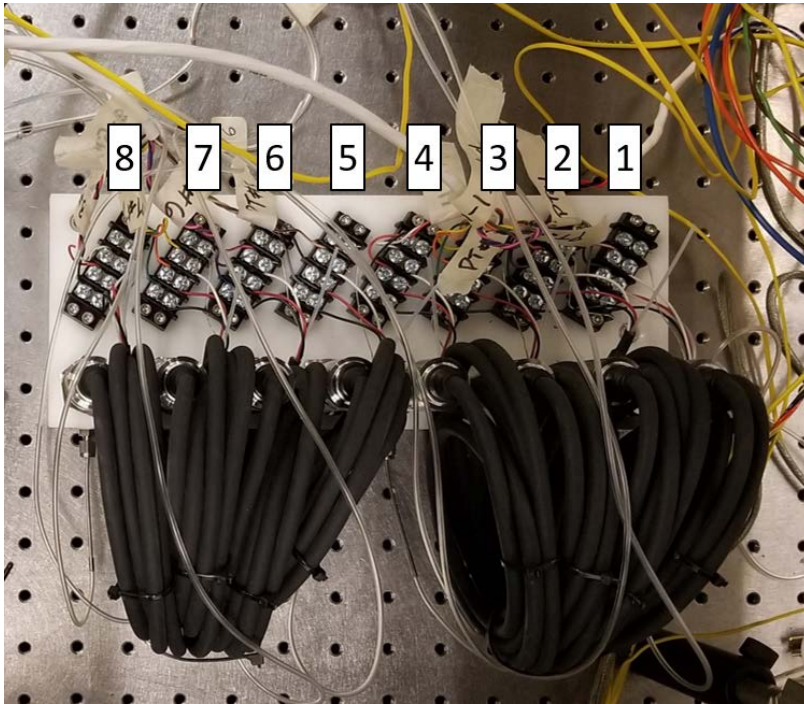


Figure 38. The pressure transducer assembly.

The thermocouple rake was used to gather temperature data at the exit of the turbine nozzle guide vanes. The rake was attached to the back of the non-rotating test stand as pictured in Figure 39. This temperature data provided a comparable result for an experimental turbine inlet profile. The rake used four Omega B-type exposed thermocouples to collect temperature data, output in Kelvin, at radial locations of 21%, 59%, 97%, and 135% on the turbine nozzle guide vane exit. The thermocouple outside of the exit passage was meant to capture exit gas products as they swirled circumferentially out of the turbine nozzle guide vanes because there was no nozzle

that confined the gases. The rake was slanted at a 70° angle to match the exit angle of the turbine nozzle guide vanes. The rake was controlled by the Raspberry Pi interface at the control station and was moved about an 80° sector, with measurements taken from 0° to 80° at 10° increments. The 80° sector physically crossed 4 vane passages; however, due to the rake's placement about one centimeter away from the exit, the rake saw exit gas temperature data from vanes outside of the 80° sector. The effects of this are discussed more in Section 4.2. Rake position and temperature data was recorded by the LabView VI.

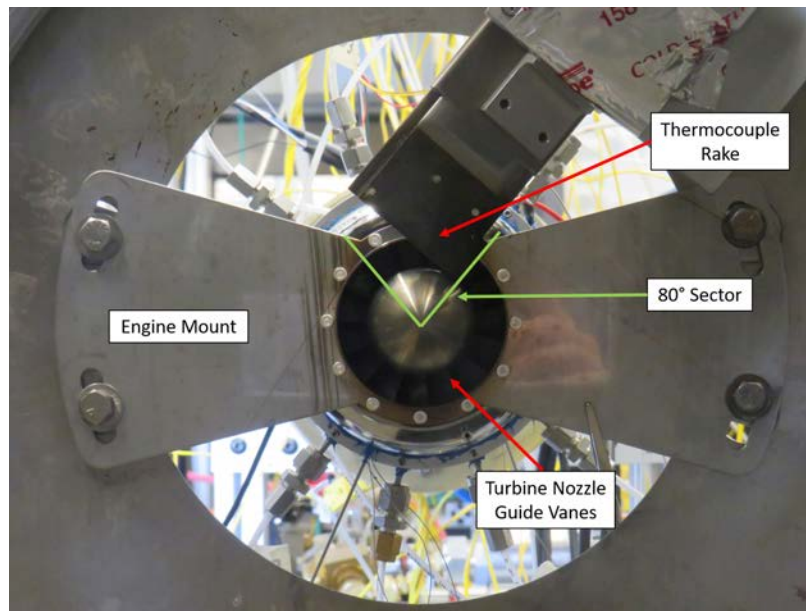


Figure 39. The thermocouple rake used to gather exit temperature profile data.

The engine's exhaust gasses were ventilated in a similar way to that of Bohan [3], where the gasses were directed through an emissions box attached behind the engine. From this box, the gasses exited the lab through an attached ventilation duct with a suction force driven by two fans. The same emissions safety equipment outlined by Bohan was utilized.

3.5.5 JetCat Test Stand

This section discusses the JetCat test stand put in place by Bohan et al. [1] [3]. The JetCat test stand allowed for safe operation of the JetCat engine with rotating hardware, providing a debris free flow path to the engine as well as an exhaust ventilation interface. The test stand also included an air starter for the engine and a kerosene pump for engine lubrication.

Much of the hardware used by Bohan [3] was reused for this engine testing. From Figure 11, the only difference was the engine mount system. The propane distribution system for the new UCC would not fit on the engine mount used by Bohan, which was therefore removed in place of another engine mounting system. Figure 40 shows the new mounting system which consisted of four lab table pylons attached to the engine bracket. Since this system did not involve a sliding engine mount, the force transducer that measured thrust was removed and thrust was not measured for this experimentation. While the thrust measurement was lost, removing the sliding mount allowed for sufficient room for the engine and the propane distribution system.

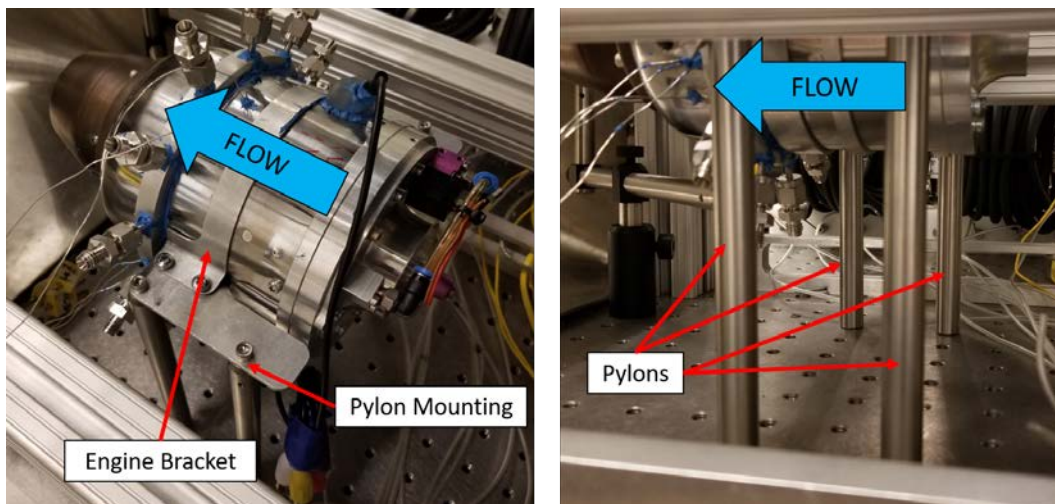


Figure 40. Engine mount system for the rotating testing.

Another difference from the Bohan [3] setup was the engine speed sensor. During Bohan's experiments, the engine speed sensor was overpowered by the signal from the lubrication pump and therefore both systems could not be run at the same time [3]. To mitigate this, Bohan designed the engine speed sensor shown in Figure 41, which ran off of an Arduino and communicated with the LabView VI via USB cable. The engine speed sensor was custom built with a magnet on the shaft for once per revolution measurements using a latching hall effect sensor (P/N US1881) with an accuracy of $\pm 0.1\%$ reading. The housing for the engine speed sensor seen in Figure 41 was designed to match the contour of the JetCat P90 RXi inlet, while providing a space to place the sensor. Figure 42 shows a side-by-side comparison of the new and stock inlets. The new inlet was axially shorter as it did not need to house an electric starter for the engine, since an air starter was used.

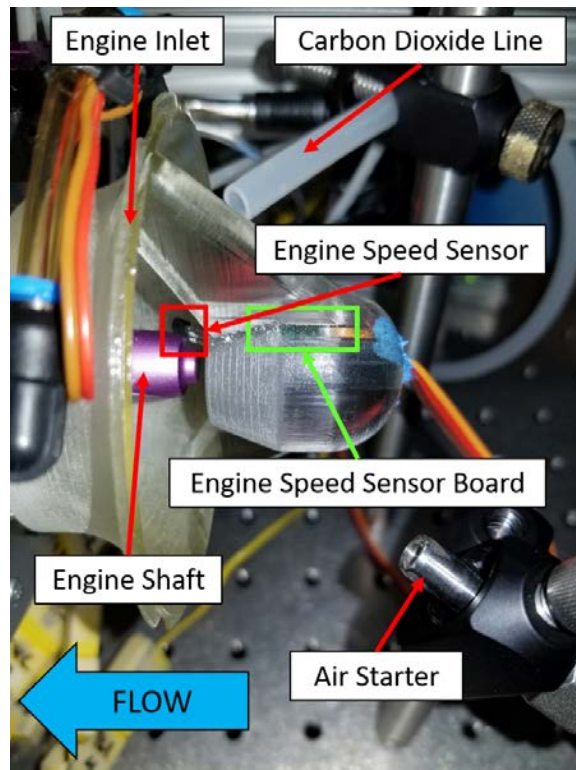


Figure 41. Engine speed sensor integrated with the engine.

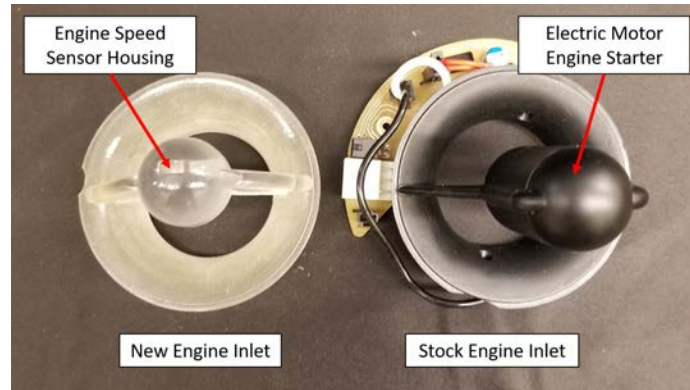


Figure 42. Side-by-side view of the newly designed and stock engine inlets.

The air starter was mounted on a lab table pylon in front of the engine, as seen in Figure 41. The air starter was directed at the engine's compressor such that when it was turned on the air jet would drive the compressor and spool up the engine. The air starter was fed by the 0.635 cm air supply line using the "AFIT Supply" of air and had either a full on or full off command with a solenoid controlled through the LabView VI. With this configuration, engine speeds of 3,600 RPM were reached with the air starter prior to ignition. An additional pylon was added to support a carbon dioxide line, from the COAL lab's fuel farm, pointed at the engine inlet that would act as a fire suppressant in case of an emergency.

The engine test stand included the same liquid kerosene lubrication pump used by Bohan [3], shown in Figure 43. The pump cycled kerosene from an outside container to a duplicate JetCat P90 RXi fuel manifold, which fed back to the container, and the lubrication ports in the engine's diffuser, which fed the engine shaft with kerosene that was forced to the bearings by secondary air flow. The pump was controlled by the LabView VI and was operated at or above 50% of the pump duty cycle once secondary flow through the engine was thought to have started (10,000 RPM and above).



Figure 43. The pump used to flow lubrication to the JetCat P90 RXi during rotating testing.

The thermocouple panel and pressure transducers for the rotating testing were identical to the setup described in Section 3.5.4 for the non-rotating testing; however, the rotating testing utilized Channels 2-12 on the thermocouple panel and all eight pressure transducers, as opposed to the reduced number for the non-rotating testing. The rotating testing used thicker diameter Omega K-type sheathed thermocouples (SCAIN-125G-6) for Stations 5-7. The placements of the temperature and pressure measurements are discussed in Section 3.6.2. The propane manifold was also reused from the non-rotating testing. During the non-rotating testing, the configuration of the propane tubes around the engine was changed to test a hypothesis regarding a hot turbine nozzle guide vane. This problem is discussed in more detail in Section 4.2. The rearranged propane tubes were kept in the same order for the rotating testing and are shown in Figure 44. In addition, the ventilation system was identical to the non-rotating testing, except now the exhaust duct interfaced with the 11 gauge stainless steel transition, shown in Figure 11.



Figure 44. The rearranged propane line placement around the engine as viewed from the rear of the engine with glow plug and turbine nozzle guide vanes for reference.

3.6 Instrumentation

This section covers the placement of the thermocouples and pressure taps in both the non-rotating and rotating configurations of the JetCat P90 RXi. Also discussed here is the expected accuracy from each of these measurement devices.

3.6.1 Non-Rotating Instrumentation

The non-rotating testing incorporated five K-type thermocouples and four pressure taps. The instrumentation was placed in the axial locations shown in Figure 45. The physical instrumentation is shown in Figure 46 and all connections fed back to the systems discussed in Section 3.5.4. The positions of the thermocouples in Figure 46b were 25%, 50%, and 75% radial span. The K-type thermocouples had an accuracy of $\pm 0.4\%$ full scale (FS) and the pressure transducers had an accuracy of $\pm 0.08\%$ FS. The B-type thermocouples used in the thermocouple rake testing had an accuracy of $\pm 0.5\%$ FS and the rake circumferential positioning had an accuracy of ± 0.5 degrees.

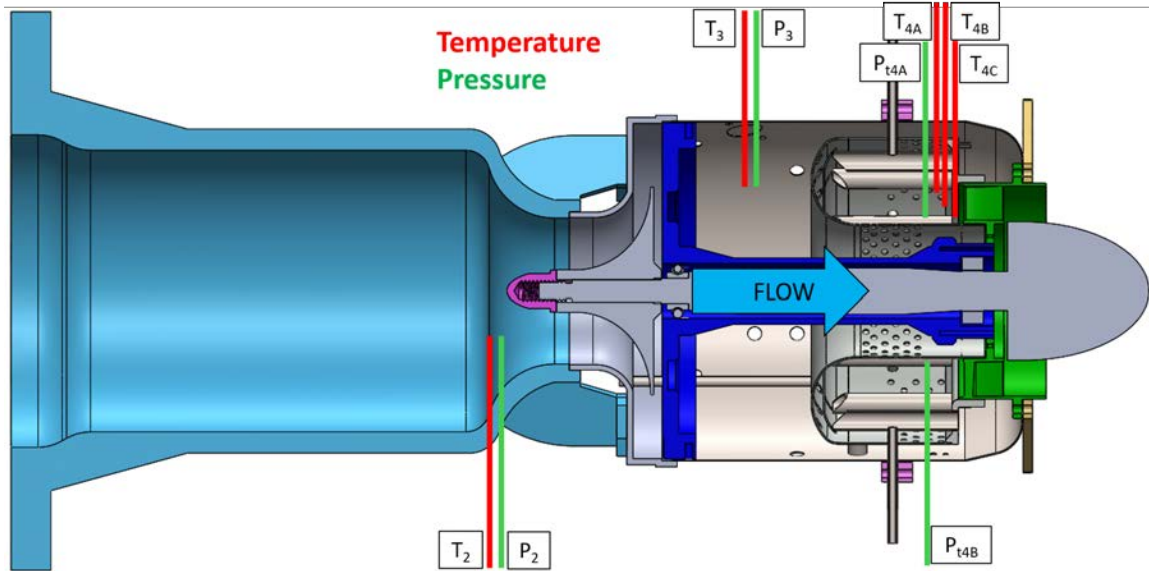
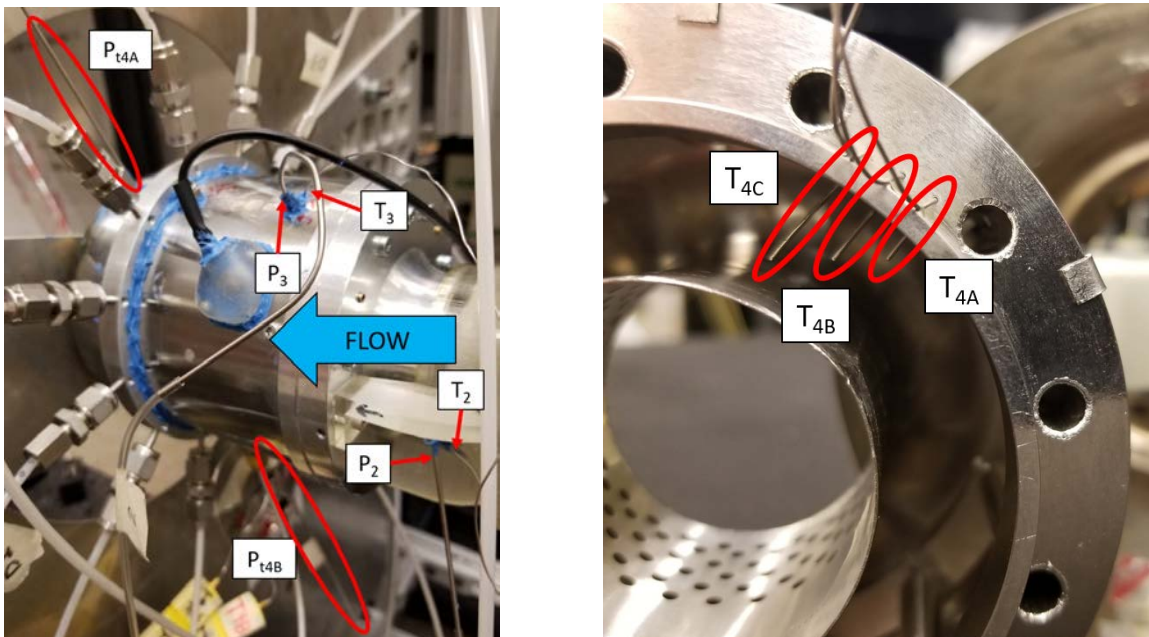


Figure 45. A cutaway of the components present in the non-rotating testing with axial positions of thermocouples and pressure taps labeled.



(a) Stations 2, 3, and 4 measurements.

(b) Station 4 thermocouple placement.

Figure 46. The physical instrumentation placed in the non-rotating configuration.

3.6.2 Rotating Instrumentation

The rotating testing used the same engine instrumentation from the non-rotating testing but added six K-type thermocouples and four pressure taps. Figure 47 shows the axial locations of the instrumentation. The placements of Stations 3 and 4 instrumentation remained unchanged from the non-rotating configuration. Figures 48, 49, and 50 show the physical instrumentation at Stations 2, 3.5, 4, 5, and 7. During the rotating testing, the C2 thermocouple, seen in Figure 49, burned out and did not provide usable data for the results. The thermocouples and pressure transducers used in this testing had the same accuracy as stated in Section 3.6.1. In addition, equivalence ratio was calculated from the air and fuel flow rates and had an accuracy of ± 0.001 .

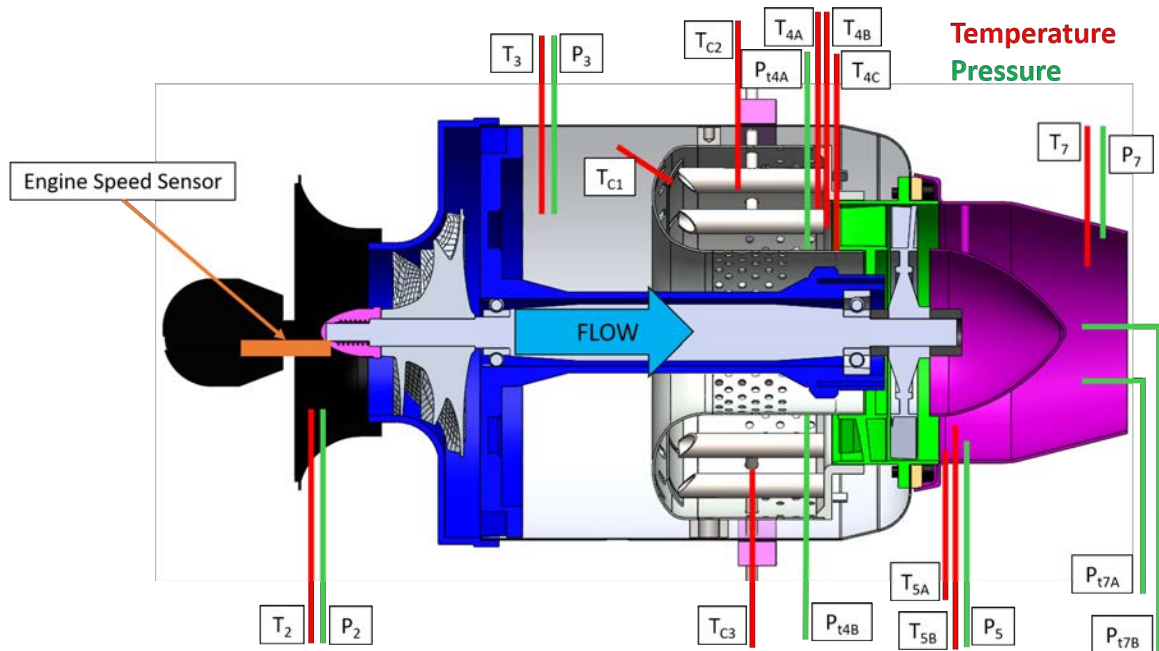


Figure 47. A cutaway of the components present in the rotating testing with axial positions of thermocouples and pressure taps labeled.

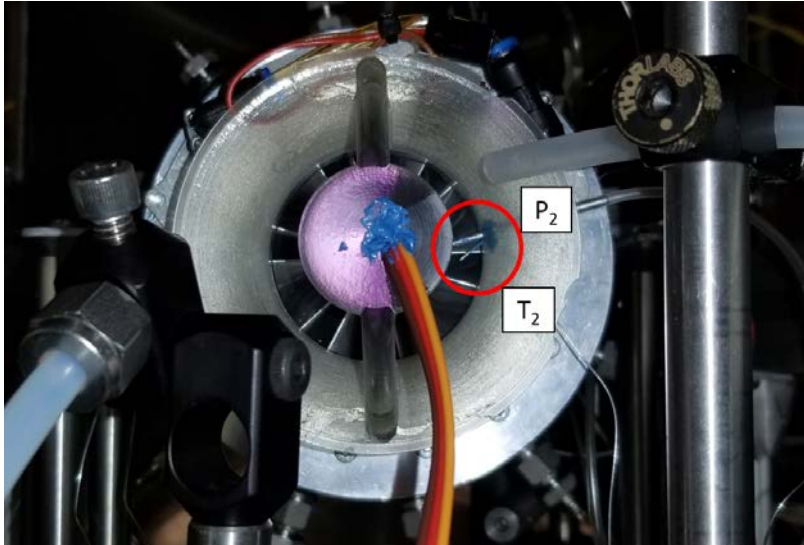


Figure 48. Thermocouple and static pressure tap placement at Station 2 for the rotating testing as viewed from the front of the engine.

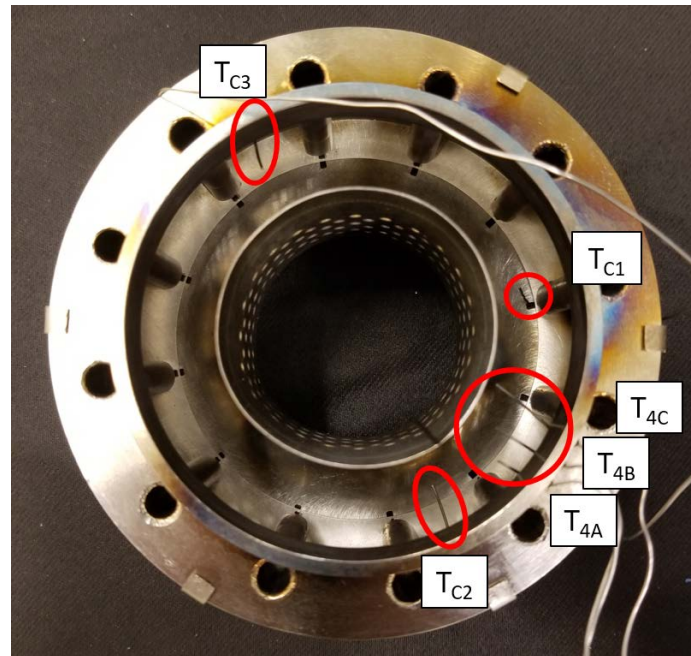


Figure 49. Thermocouple placements inside of the combustor for the rotating testing as viewed from the back of the combustor.

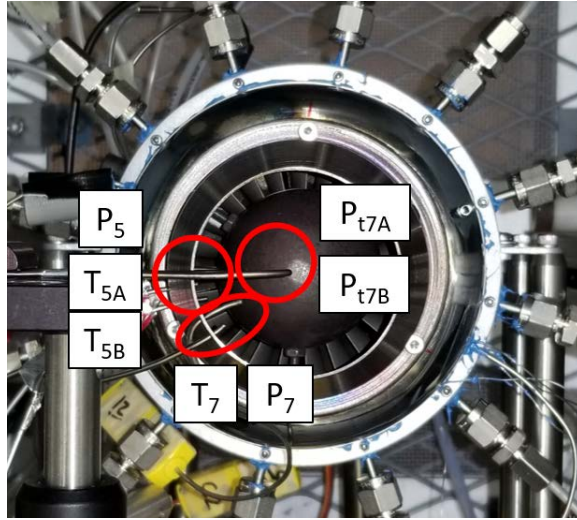


Figure 50. Temperature and pressure measurements at Stations 5 and 7 as viewed from the exhaust duct.

IV. Results

The objective of this research was to design, integrate, and test the new Ultra Compact Combustor (UCC) into the JetCat P90 RXi to achieve self-sustained operation while maintaining a 33% length reduction. This was accomplished using both computational and experimental methods. The results presented in this chapter summarize the findings of the present research regarding the stated objective. Section 4.1 discusses the computational analysis results. This analysis studied the UCC as it would be integrated into the JetCat P90 RXi at several test conditions across the engine's operating range. Section 4.1.1 looks at the flow of fuel and air through the combustor to include the effect of dilution holes as well as the exit temperature profile of the combustor. Section 4.1.2 compares the computational results of the new UCC to the stock JetCat P90 RXi combustor data, as well as to the Bohan et al. [2] computational data.

The experimental results are discussed in Sections 4.2 and 4.3. Section 4.2 covers the non-rotating testing that was done, where the UCC was tested within the engine but without rotating turbomachinery. In this configuration, air was force fed into the engine to simulate air entering into the compressor. This configuration allowed for temperature measurements to be taken with a thermocouple rake at the exit of the turbine nozzle guide vane. In addition, the combustor performance metrics of the exit profile and pattern factor were evaluated. Section 4.3 discusses the testing done with rotating turbomachinery. This testing allowed for higher pressures to be reached within the engine to test higher operating conditions. In the rotating configuration, measurements were taken at each engine station to determine engine performance and was compared to the stock performance data.

4.1 Computational Results

The computational analysis was completed using the domain discussed in Section 3.3.1 and the FLUENT set up and flow conditions (chosen from stock engine operating data) from Section 3.3.2. The flow path through the domain, shown in Figure 20, followed that of Figure 15 with air entering through the compressor exit and fuel entering through the propane tube. The combustion products exited through the combustor exit and the turbine nozzle guide vanes into what would have been the turbine section. This exit plane was the main point of interest for the combustor metrics. In addition, the combustor flow path was looked at to determine if flame holding was evident off of the impingement plate.

4.1.1 Combustor Flow Path and Profile Analysis

Figure 51a illustrates the flow through a center plane of the combustor utilizing velocity vectors colored by magnitude, at the design (cruise) condition of 250 g/s of air at an equivalence ratio of 0.4. The center plane cut was taken between the two forward dome inlets and extended to the nozzle guide vane, as outlined in Figure 51b. The recirculation region behind the impingement plate is highlighted in Figure 51c. This region is indicated by two black circles inscribing small flame-holding recirculation pockets behind the plate. The vector colors in this region indicated that the velocity magnitude was low, thereby allowing combustion to occur while exchanging burnt products with new reactants. The impingement plate provided the combustor with not only a flame holder but also a means to decrease incoming flow velocity to facilitate combustion. In addition, the swirling behind the plate promoted mixing of the air and fuel in this region, furthering combustion reactions. Figure 52 shows pathlines for flow entering a forward dome inlet and hitting the impingement plate, distributing the flow to the inner and outer diameters and behind the plate.

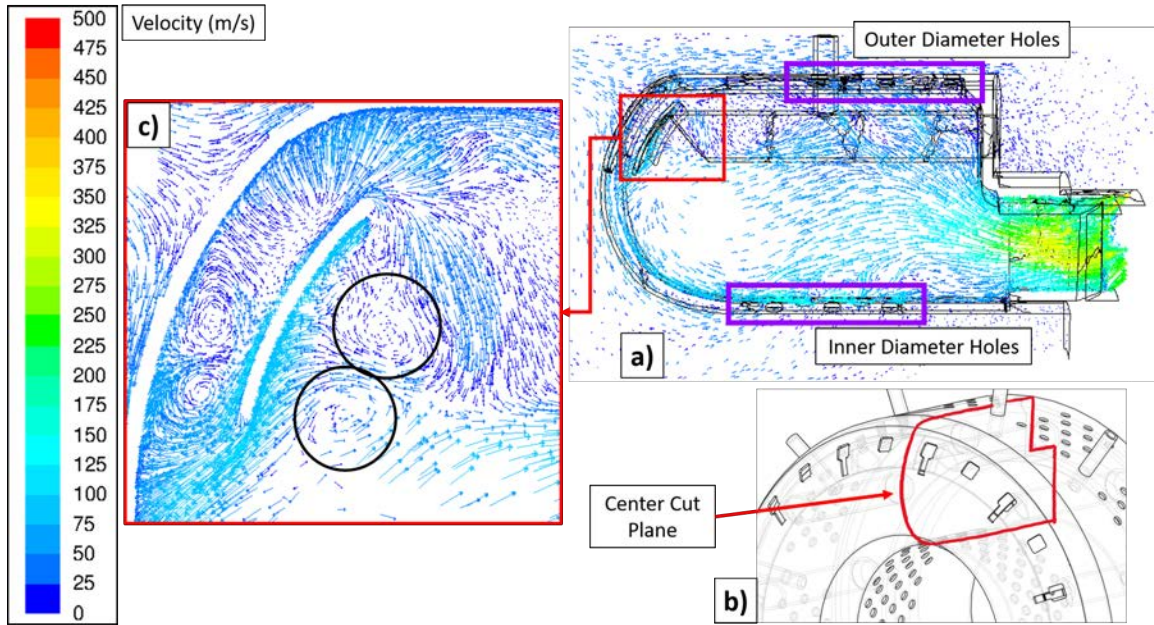


Figure 51. Velocity vectors (a) colored by velocity magnitude (m/s) on the center cut plane (b) at the design point, with recirculation zones behind the impingement plate highlighted (c). Outlined in purple are the dilution holes, which contribute 63% of the total air flow into the combustor.

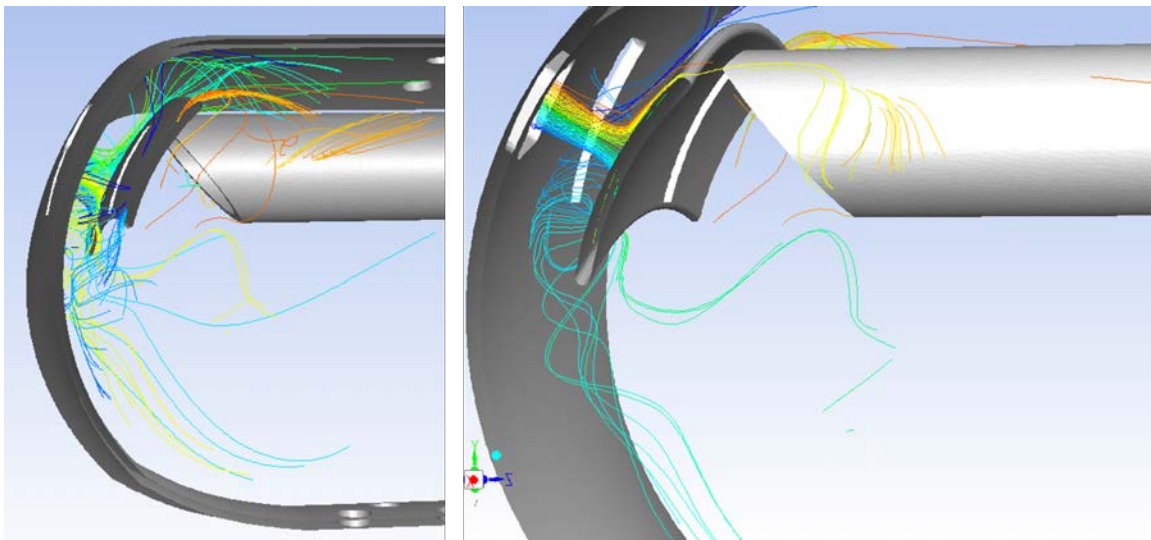
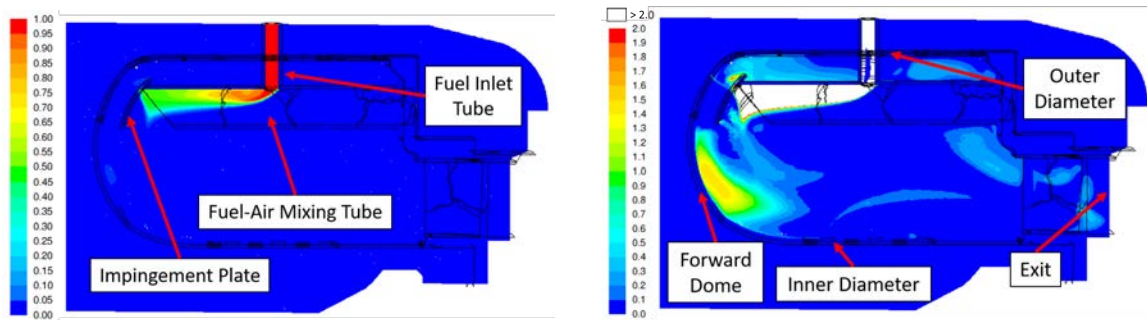


Figure 52. Two views of flow pathlines, differentiated by color, entering through a forward dome inlet hitting the impingement plate.

Figure 53 demonstrates the ability of the circulation zone behind the impingement plate to break up and distribute the propane introduced from the fuel-air mixing tubes. As Figure 53a shows, the propane entered through the fuel inlet into the fuel-air mixing tube, where it was initially mixed with air, but was still very fuel rich as shown by the equivalence ratio contours in Figure 53b, and then dumped behind the impingement plate. At this point, the combustion reactions in the flame holding recirculation zone caused the propane to dissociate into other hydro-carbon species, proving that the recirculation zone provided a sufficient stable flame holding source. In addition, the recirculation zone was able to distribute the fuel throughout the combustor, as shown in Figure 53b. Pockets of fuel were distributed on both the inner and outer diameters of the combustor, with the largest concentration of fuel gathering on the forward dome. This large fuel pocket fell in line with the midspan of the combustor exit, which proved useful when tailoring the temperature exit profile to peak at the midspan of the exit with the help of the dilution holes.



(a) Propane mass fraction contours.

(b) Equivalence ratio contours.

Figure 53. Contours on the plane cutting through the fuel air mixing tube and the propane inlet tube, showing how the propane cracked once it reached the recirculation zone and the mixing of fuel and air in the combustor, based on equivalence ratio.

The purple boxed regions of Figure 51a highlight the dilution holes present in the combustor. The jets exiting the dilution holes sped up the combustor flow and

provided cool, unburnt air to the combustion process. It can be seen that these dilution holes push the flow up and away from the combustor wall, providing cooling to the walls and shaping the combustor exit profile. The high velocity vectors (150 m/s) exiting the dilution holes have a pronounced effect on the flow path through the combustor, contributing 31% of the total air flow into the combustor on the inner diameter and 32% on the outer diameter, as compared to the 22% provided by the forward dome inlets and the 15% by the fuel-air mixing tubes.

The targeted pressure drop through the combustor due to aerodynamic losses was 5%. Figure 54 shows total pressure contours on the center plane at the design point, where the majority of the pressure losses derived from the air inlets and dilution holes. Rayleigh losses were not seen in the combustion regions, where the combustor operated at a constant pressure. At the design condition the combustor flow path resulted in a 4.9% pressure drop from the primary air inlets to the nozzle guide vane inlet. This pressure drop allowed for a favorable pressure gradient across the combustor which forced air through the inlets and dilution holes.

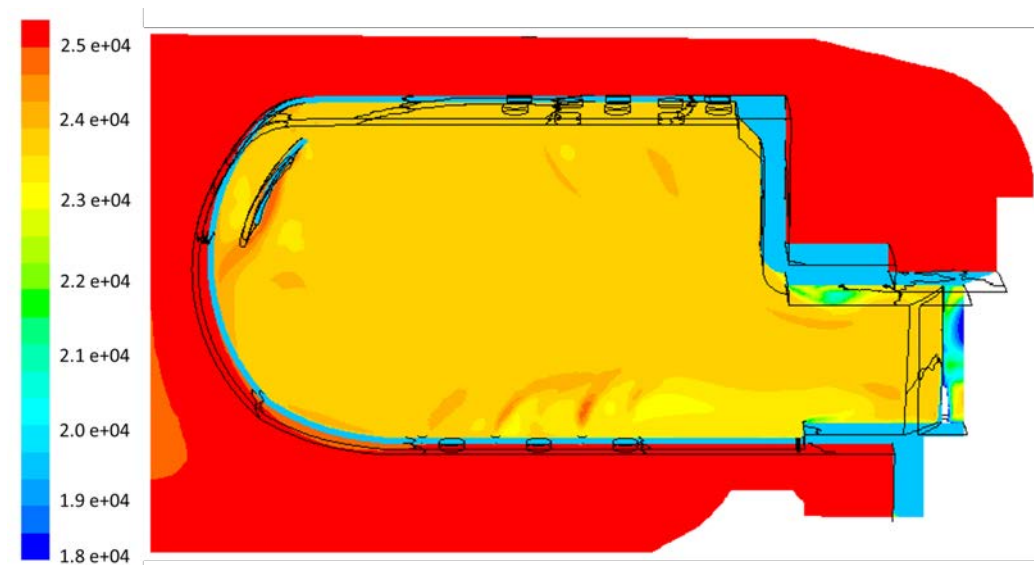


Figure 54. Total pressure (Pa) contours on the center cut plane at the design point.

The dilution holes' effect on the combustor temperature is outlined in Figure 55 which shows a contour plot of temperature on the same center cut plane as Figure 51b, both taken at the design condition. While the temperature contour plot does not directly show where combustion reactions have occurred, it does show the effect that they had on the flow and on the exit temperature profile. In addition, the high temperature areas corresponded well with the fuel distributions shown in Figure 53b, further showing that the recirculation zone performed well at distributing the reactions throughout the combustor volume. Figure 55 also shows the strong effect that the dilution holes had on the inner and outer diameter profiles of the combustor flow. The jets exiting the holes pushed the hot combustion products away from the combustor walls, keeping them cool.

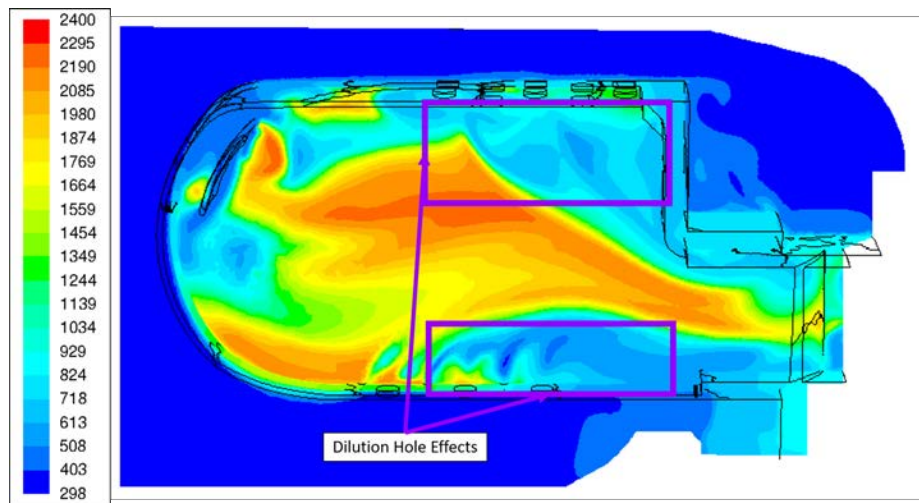


Figure 55. Temperature (K) contours on the center cut plane at the design point. The cooling effect of the dilution holes is highlighted in purple.

Figure 56 shows temperature contours on the surface of the combustor for the on and off design conditions. The temperature scale was set with a maximum of 1600 K because the melting point of Inconel 600 was 1627 K [27]. All surfaces remained below 1600 K, and the fuel-air tubes remained heated through all conditions, validating

their use as kerosene vaporizers as discussed in Section 3.2. Both the inner and outer diameter dilution holes prepared the flow for the turbine by keeping hot gases away from the hub and tip, keeping the hottest combustion products in the center of the exit profile.

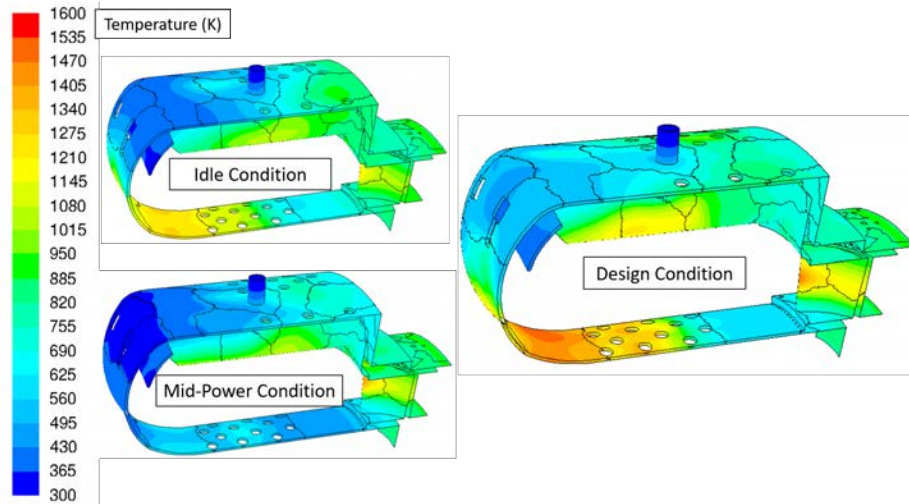


Figure 56. Temperature (K) contours on the surface of the combustor for on and off design conditions.

The mid-power condition in Figure 56 had a much lower surface temperature at the bottom of the forward dome when compared to the idle and design conditions. One cause of this was the lower equivalence ratio at which the mid-power condition operated at. However, the equivalence ratio difference was only 0.005 between the idle and mid-power conditions. Therefore the temperature difference on the combustor surface was more indicative of a difference in locations of high heat release. Figure 57 shows a comparison for temperature contour plots on the center cut plane at the mid-power and design conditions. It is apparent that the general locations of high heat release are the same between the two conditions; however, the mid-power condition experiences less heat release on the bottom of the forward dome when compared to the design condition. The heat release was lifted off of the wall and resided closer to

the impingement plate. The presence of less heat release directly on the wall caused the lower surface temperature at the mid-power condition.

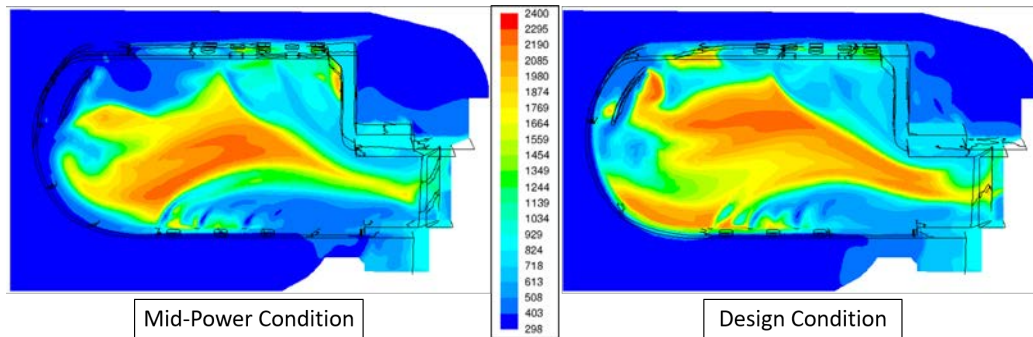


Figure 57. Comparison of the temperature (K) contours on the center cut plane at the mid-power and design conditions.

The flow presented to the turbine through the nozzle guide vanes was analyzed using a circumferentially averaged radial profile. Figure 58 shows the circumferentially averaged exit temperature profile across the radial span at the design condition, before and after the turbine nozzle guide vanes, with the exit temperature contour from which it was derived in the top right corner. It is evident from these profiles that the turbine nozzle guide vane had a considerable effect on the shape of the turbine inlet profile. The temperature peak at 90% radial span was caused by a horseshoe vortex, shown in Figure 59, that formed off of the leading edge of the turbine nozzle guide vane, near the outer diameter. This vortex pulled hot gases from the midspan towards the outer diameter and migrated cooler gas towards the midspan, creating a dip in temperature between the two peaks. Figure 59 shows the high swirl of the vortex that caused the radial profile migration and the radial span of the vortex across the exit passage. In addition, the small cooling jets on the inner diameter pushed the flow over the turbine nozzle guide vane lip and prevented a vortex from forming. With the effects of the turbine nozzle guide vane in mind, the exit profile was shaped by the flow exiting the dilution holes on the inner and outer diameters. Changes to the

dilution hole patterns or sizes would cause shifts in the exit profile shape, providing a means to further refine the profile.

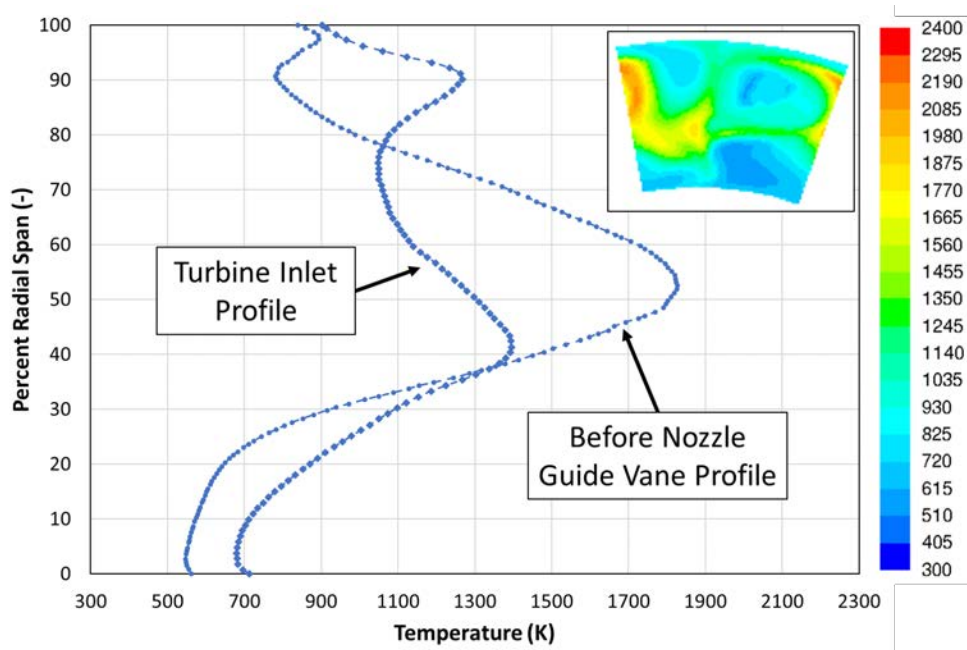


Figure 58. Circumferentially averaged temperature profile before and after the turbine nozzle guide vane at the design condition, with the exit temperature contour from which it was derived in the top right corner.

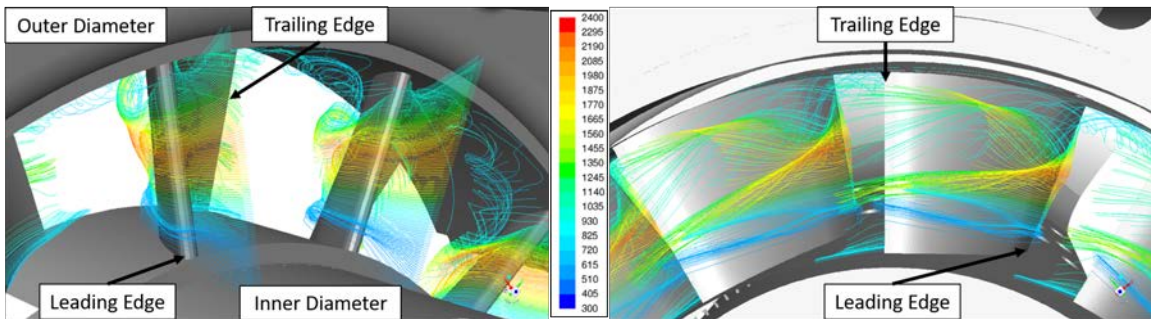


Figure 59. Pathlines, colored by temperature, showing the horseshoe vortex that formed off of the leading edge of the turbine nozzle guide vane on the outer diameter. On the inner diameter, the small cooling jets push the flow off the surface and stop a vortex from forming.

In addition to the design point, the idle and mid power condition profiles were examined. Figure 60 shows the profiles for the three test conditions, with their respective average turbine inlet temperatures represented by the dashed lines. The three profiles were similar, with an expected drop in temperature between the design point and both mid power and idle conditions. The temperature drop was caused by a change in equivalence ratio, where the design condition was run at an equivalence ratio of 0.4, idle at 0.34, and mid power at 0.335. The equivalence ratio changes matched that of the stock engine, as discussed in Section 3.3.2. The changes in equivalence ratio also drove the differences in average exit temperatures for the three cases: 1080 K (design), 875 K (mid), and 910 K (idle). In addition, the more linear profile of the mid power condition was due to 2% less air entering the dilution holes as compared to the idle and design conditions. With less dilution hole air flow, the mid power profile had a less pronounced peak temperature near midspan.

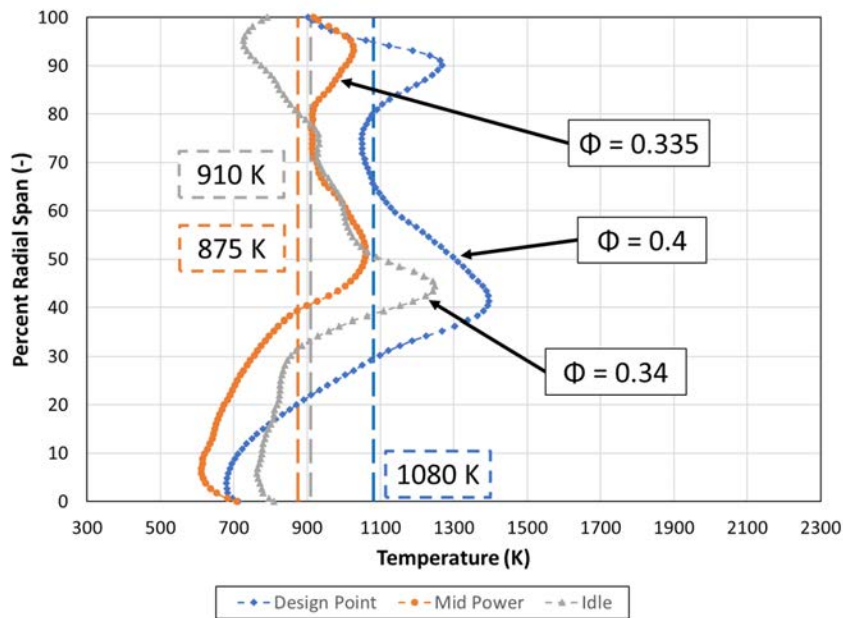
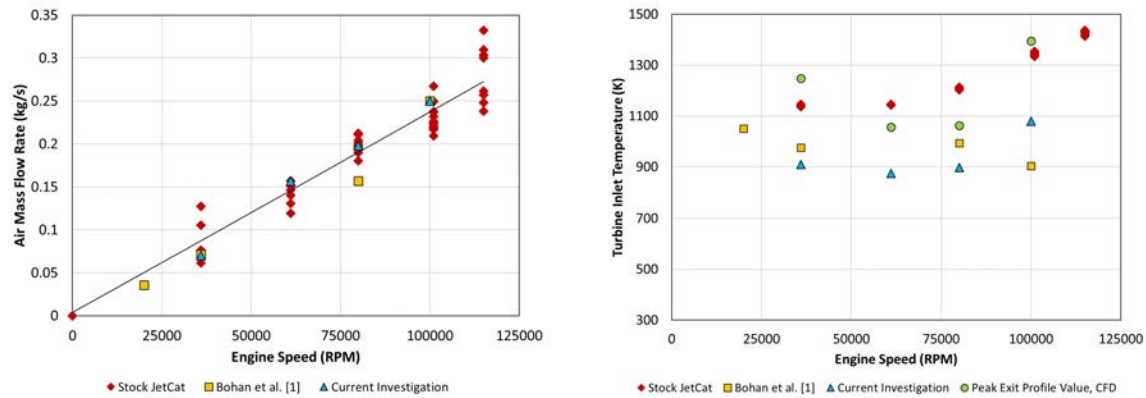


Figure 60. Circumferentially averaged temperature profile at the pressure outlet plane after the turbine nozzle guide vane with average temperatures for each condition represented by the dashed lines.

The exit profile characteristics also drove the pattern factor at the turbine inlet. The pattern factor was calculated to be 0.67 at the design condition. While this value was higher than the desirable value in current literature [4], Bohan et al. [2] experienced a pattern factor drop from 0.6 to 0.15 when comparing computational to experimental results on the same scale. The stock combustor does not have data available for a pattern factor calculation comparison because data was only taken at a single radial point; however, testing of JetCat engines at the Air Force Research Laboratory has shown that the stock engine tends to eject flames out of the turbine section, indicating an undesirable pattern factor and incomplete combustion. Therefore, a pattern factor of 0.67 was determined reasonable from computational analysis and warranted additional research with physical hardware.

4.1.2 Combustor Performance Comparison

As discussed in Section 3.3.2, the analysis conditions for the present research were chosen to match points on the stock engine operating line, provided by Mr. Jacob Wilson. Figure 61a shows the total air mass flow rates into the engine for the stock data, Bohan et al. [2] data, and the present computations. The trendline in Figure 61a represents the trend of the stock engine data across the operating regime. The three data points from the current CFD results represent the three previously discussed test conditions where the idle case corresponds to the 36,000 RPM data, mid-power to 61,000 RPM, and the design point to 100,000 RPM. Additionally, a point comparable to 80,000 RPM, not shown previously, was added to fill in the operating range of the combustor. Figure 61b shows the average turbine rotor inlet temperature for the same data points shown in Figure 61a, where the stock exit temperature data was taken with a thermocouple placed nominally at the midspan of the exit.



(a) Air mass flow into the engine, with the trend-line outlining the stock engine trend.

(b) Average turbine rotor inlet temperatures, with peak temperatures from Figure 60.

Figure 61. Comparison plots for the stock JetCat P90 RXi data, computational results from Bohan et al. [2], and data from the present research.

At the idle condition, the turbine rotor inlet temperature fell below both that of the stock data and the Bohan et al. data; however, when the peak temperature data from the exit profiles in Figure 60 was plotted, the peak temperature matched closer to the stock temperature data, with 112 K increase instead of the previous 226 K decrease. As stated previously, the stock data was taken at the midspan of the exit which is more representative of the maximum temperature seen at the turbine rotor inlet, rather than the total turbine inlet average on the exit plane. The same was true for the mid power and design conditions, where the peak temperature fell closer to the stock data than the average temperature. Therefore, looking at the midspan, or peak, temperature of the CFD data would result in a more accurate comparison to the stock data.

The mid power condition had similar results to the idle condition where the average data fell below that of the stock but the peak profile temperature fell closer with an 84 K decrease. The decrease in temperature from the idle to the mid power

condition was due to the drop in equivalence ratio from 0.34 to 0.335 to match that of the stock data. While the average CFD temperatures were lower than the stock data, due to the nature of the stock measurements, the trend of the average turbine inlet temperatures match with those stock, showing that the UCC reacted similarly to changes in equivalence ratio as the stock combustor. Both the idle and mid power conditions were conducted at an additional equivalence of 0.3 to see evaluate their changes in exit temperature. The mid power case did not noticeably change; however, the idle case experienced a decrease in average turbine inlet temperature by 29 K and in peak temperature by 90 K. This shows that the lower idle condition was more sensitive to changes in equivalence ratio.

At the design condition, the current CFD had a 50 K increase for the peak temperatures over the stock combustor, with both being run at an equivalence ratio of 0.4. When comparing the average temperatures of the CFD data, the present computations achieved a 180 K increase in exit temperature over the previous Bohan et al. [2] design. However, the Bohan et al. design was performed at an equivalence ratio of 0.3 rather than 0.4. When the new UCC was run at an equivalence ratio of 0.3, for comparison, the average turbine inlet temperature matched that of the Bohan et al. design within 6 K. In addition, based on equilibrium combustion calculations, an increase in equivalence ratio to 0.4 for the Bohan et al. combustor would result in a similar exit temperature as the current design. The peak exit temperature at the design condition illustrates that similar performance was achieved by the new UCC when compared to the stock combustor, while incorporating the 33% length savings seen in the Bohan et al. combustor.

4.2 Non-rotating Experimental Results

The non-rotating experimental testing was accomplished to experimentally analyze the exit profile of the new UCC integrated with the JetCat P90 RXi and ensure the fuel-air mixture in the combustor would ignite and sustain combustion. This testing allowed engine operation without rotating turbomachinery up to the engine idle condition because the flow rates, pressures, and temperatures of the higher engine speed conditions were unattainable with the available hardware. The testing was done on the non-rotating test stand in the AFIT COAL lab as described in Section 3.5.4.

The idle condition was already known to be the maximum air and fuel mass flow rates to be achieved, and therefore a lower bound needed to be determined. This lowest condition would be the point at which the engine ignited and began a consistent burn. The light condition was determined by starting at a low air mass flow rate of 31 g/s (an air setting of 5% open on the air mass flow controller) and increasing fuel flow rate by one SLPM with the glow plug on until ignition occurred. Ignition was observed at 13 SLPM of propane, or 0.399 g/s, resulting in a calculated equivalence ratio of 0.202. This condition was then established as the light condition. The engine ignited at this condition for every test, demonstrating repeatability.

Three points were added between the light and idle conditions, with the initial mindset to ramp equivalence ratio up to the expected equivalence ratio at idle of 0.340 from the calculated equivalence ratio at the light condition of 0.202. Test points at air settings of 42.7 g/s (7%), 48.6 g/s (8%), and 60.4 g/s (10%) were picked to fill in the range between light (31 g/s) and idle (72.1 g/s). The chosen equivalence ratios for the three additional conditions were 0.274, 0.313, and 0.334 to ramp up to idle. This would result in fuel flow rates of 23 SLPM, 33 SLPM, and 42 SLPM, respectively, with the idle condition being 50 SLPM.

Four separate tests were completed, with two test runs (1 and 2) done on 17 January 2020 and two more test runs (3 and 4) with the thermocouple rake done on 22 January 2020. Testing began successfully, with ignition occurring consistently at 31 g/s of air and 0.399 g/s of fuel. Figure 62 shows an image of the nozzle guide vane exit directly after ignition. Figure 62 also provides a numbering scheme for the turbine nozzle guide vanes which will be used later in this discussion. As discussed in Section 3.3.1, the experimental testing incorporated the stock engine's 15 turbine nozzle guide vanes, where the computational model only incorporated 12 vanes for ease of modeling the periodic nature of the combustor.

Once the combustor reached a steady state, data was taken, and then the air and fuel mass flow rates were increased to the next condition. Figure 63 plots the average exit temperature against the air mass flow rate with the equivalence ratio plotted on a secondary axis. Runs 1 and 2 were baseline tests that generated a basic understanding of the combustor operability in the non-rotating configuration. When the fuel mass flow rate was pushed to increase the equivalence ratio from the light condition on the first run, the combustor exit temperatures began to reach values over 1100 K, with a maximum recorded value at the midspan of 1324 K and an average exit temperature of 1176 K. This occurred at the air mass flow rate of 42.7 g/s (7%) and fuel mass flow rate of 33 SLPM resulting in a calculated equivalence ratio of 0.259 (corresponding to the second data point for Run 1). These exit temperature values began heating the turbine nozzle guide vanes, coloring them shades of pink and red as seen in Figure 64. When this was observed, the initial equivalence ratios planned for the runs were not used. Instead, fuel flow rates were decreased to maintain the exit temperature below 1000 K. This resulted in a range of equivalence ratios between 0.2 and 0.23 instead of the 0.3 to 0.34 range.

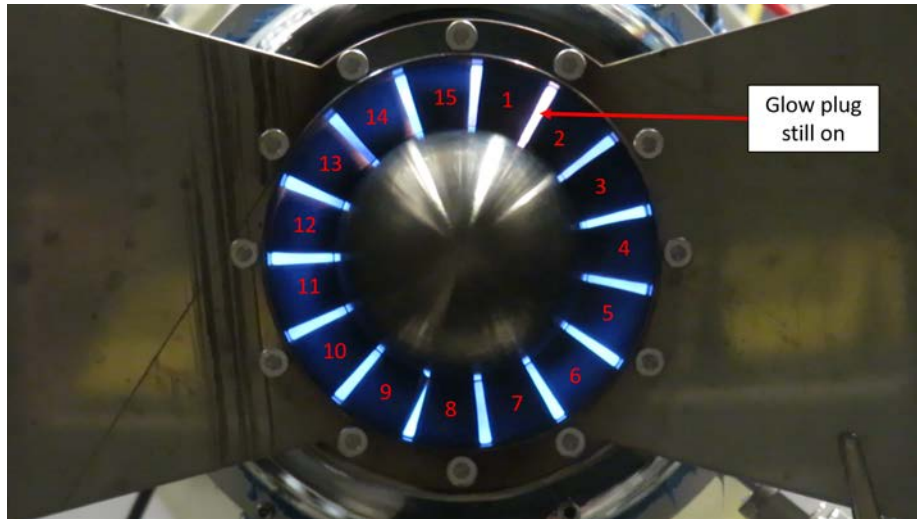


Figure 62. A photograph of the nozzle guide vane exit immediately following ignition in the non-rotating configuration.

To determine the range of the combustor, an equivalence ratio test was done, indicated by the vertical line at the idle condition for the Run 1 data on Figure 63. The fuel flow rate started at 29 SLPM and was increased by increments of one SLPM until a fuel flow rate of 33 SLPM was reached. The average exit temperature at 33 SLPM was 1086 K with a maximum exit temperature of 1222 K at the midspan, marking the highest fuel flow rate before reaching unfavorable exit temperatures. Run 2 was accomplished to further identify the necessary equivalence ratios to achieve desired exit temperatures. Runs 3 and 4 evaluated the performance of the combustor with less variation in equivalence ratio. The fuel flow rates for Runs 3 and 4 did not change in between them, unlike Runs 1 and 2. This is seen in Figure 63 by the overlapping equivalence ratio data. The associated fuel flow rates during Runs 3 and 4 for each condition starting from light were 13 SLPM, 18 SLPM, 21 SLPM, 26 SLPM, and 31 SLPM at idle. These fuel flow rates resulted in a fairly constant equivalence ratio around 0.205. There was little variation between runs, with a maximum difference of 25 K between Runs 3 and 4, indicating repeatable results from the combustor.

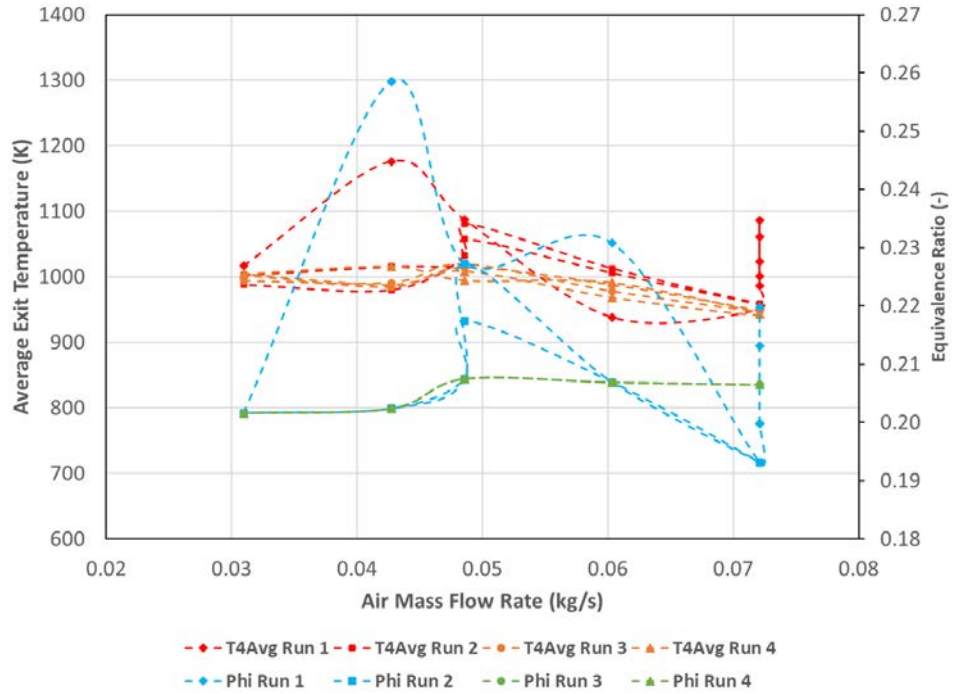


Figure 63. Average exit gas temperature as measured by the three thermocouples at the combustor exit plotted against air mass flow rate with equivalence ratio as a secondary axis.

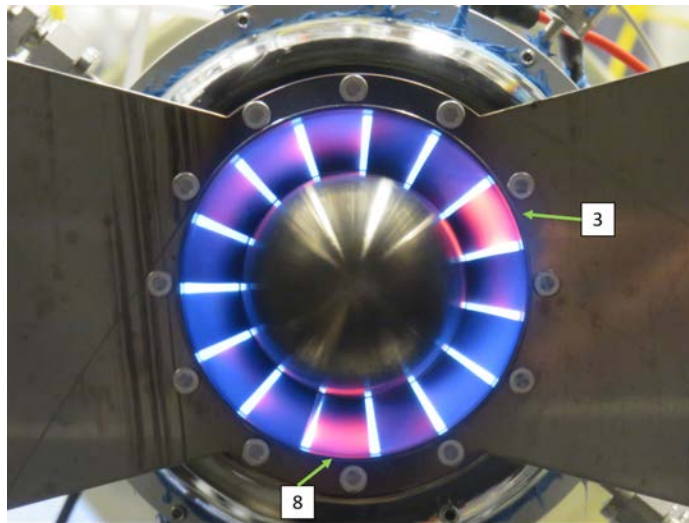


Figure 64. A photograph during Run 2 of the heated nozzle guide vanes with recorded temperature values reaching 1324 K.

Additionally, Runs 3 and 4 incorporated the thermocouple rake behind the turbine nozzle guide vanes as discussed in Section 3.5.4. Figure 65 shows the collected exit profile data from the rake at three conditions: light, idle, and a point between the two (the middle condition) at 48.6 g/s of air and 21 SLPM of fuel. Rake data was taken at the idle condition during both Runs 3 and 4, providing two separate rake profiles. It is important to remember that the thermocouple rake data was used to predict exit temperature patterns and was not a high fidelity tool. In total the contour maps were made up of 36 positions, with 4 radial locations across the 80° sector.

The temperature contours showed that the maximum temperature occurred outboard of midspan with gradual gradients to the cooler inner and outer diameter temperatures. The two idle contours demonstrated the repeatability between testing with a maximum difference in temperature of 17 K. The exit contours appeared fairly uniform for the light and middle conditions with a maximum temperature change of 173 K for the light condition and 192 K for the middle condition, resulting in pattern factors of 0.18 and 0.24 respectively. The idle contour data resulted in a larger temperature spread of 250 K, but still produced an average pattern factor of 0.38, falling within the desired bounds of the literature discussed in Section 2.4.

The profiles were consistently hotter towards the -40 circumferential side, implying a hotspot was present. This could have been the same hot region as seen in Figure 64 by Vane 3 visibly radiating. The vanes had approximately a 70° angle which combined with the one centimeter distance of the rake from the exit caused the hot gases from Vanes 3-6 to travel up to 50° towards the -40 circumferential side of the contour plot. The transport of the hot gases due to the vane angles explained why the gases from Vanes 3-6 were visible in Figure 65 rather than the gases from Vanes 14, 15, 1, and 2. Therefore, the hotspot seen at the idle condition on the contour plots was from the Vane 3 passage and should not be present across the entire combustor exit.

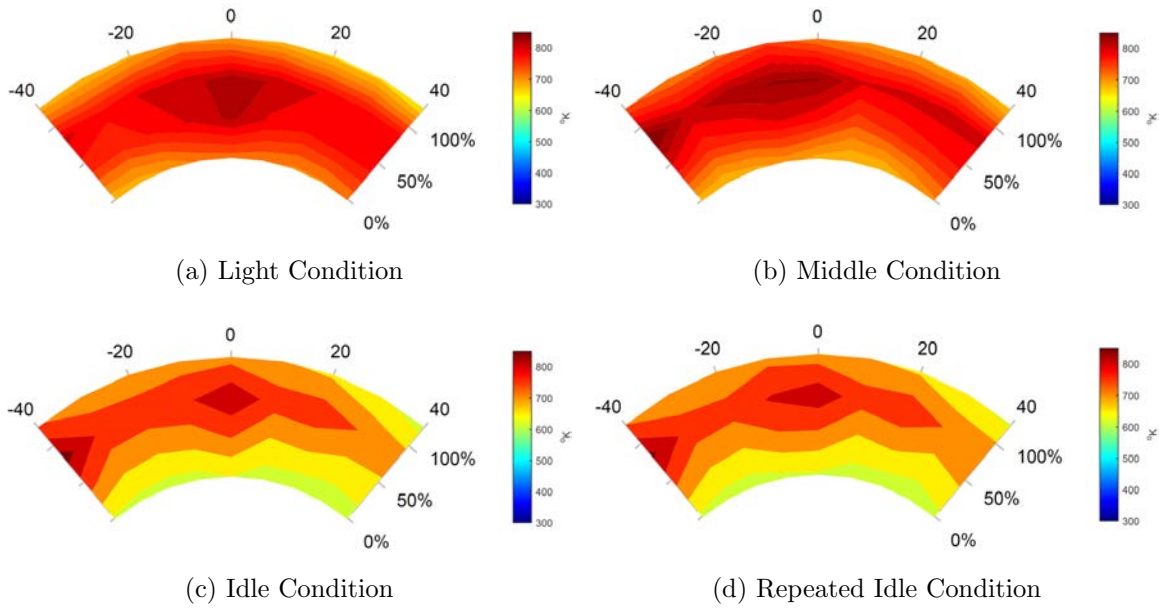


Figure 65. Temperature (K) contours from the thermocouple rake data.

Figure 66 shows the exit temperature contours at the idle condition from the thermocouple rake data compared to the computational results at the turbine nozzle guide vane exit. The computational data is on a larger scale than the experimental data, ranging from 300-1700 K rather than the 300-900 K of the experimental results. In addition, the experimental data was not gathered directly at the turbine nozzle guide vane exit, as discussed above. These two factors made it difficult to compare the two contours, but the comparison was useful to identify similar patterns. The computational analysis predicted a maximum temperature at the midspan location, generated by a hotspot. It also showed a cooler hub and tip temperature relative to the midspan. These trends were observed in the experimental results as well with the hottest region outboard of midspan, and the coolest temperatures on the inner and outer diameters.

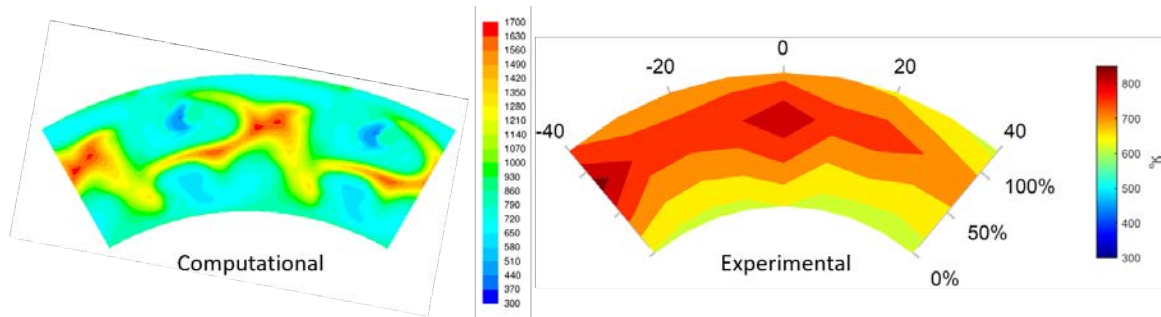


Figure 66. Comparison of the computational and experimental turbine nozzle guide vane exit temperature (K) contours at the idle condition.

The combustor performed well initially; however, there were two observed issues with the combustor’s operation: the hot vanes observed on the two and six o’clock positions of the turbine nozzle guide vanes and the suspiciously low calculated equivalence ratio.

Figure 64 showed how at high exit temperatures the turbine nozzle guide vanes were heating. Two vanes in particular were noticeably hotter than the rest, those labeled 3 and 8. When the engine operated at lower exit gas temperatures, only Vane 3 was visibly radiating, as shown in Figure 67. The hot vanes were initially thought to have been caused by an uneven distribution of fuel from the propane manifold. To mitigate this, all the propane lines were checked for blockages and the lines were rearranged to provide a different fuel distribution to the combustor. The arrangement from Figure 34b was changed to that of Figure 44. After this change, Vane 3 was still visibly radiating.

One possible cause for the uneven hot vanes was the distribution of incoming air to the combustor from the diffuser. The stock diffuser had four vane passages that were 1.0 mm smaller than the rest of the diffuser vane passages, due to four larger vanes with screws that held the diffuser in place, as seen in Figure 68.

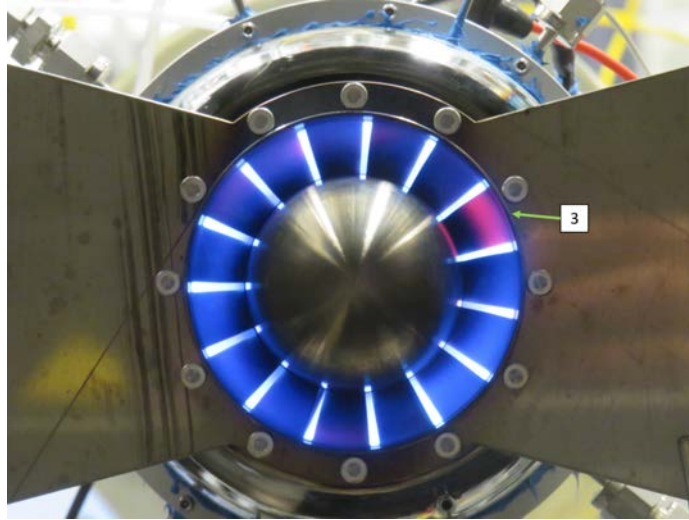


Figure 67. A photograph of the nozzle guide vanes with Vane 3 heated.

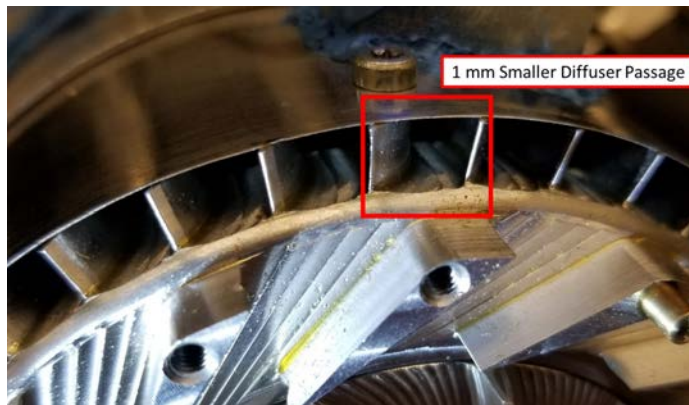


Figure 68. The front of the stock engine diffuser with the smaller vane passage highlighted.

One of these smaller diffuser passages lined up with the general area of Vane 3 of the nozzle guide vane. Figure 69 shows a side view of the engine where the larger vane is highlighted and is line with the second propane air tube after the glow plug. When this information is paired with Figure 70, Vane 3 falls in line with the location of this irregularity in the diffuser passages. The smaller diffuser passage due to the larger diffuser vane was a possible cause for less air to enter the combustor at this location, causing a higher local equivalence ratio. This pattern is most likely not

repeated as there were 40 diffuser passages but only 15 turbine nozzle guide vane passages and the three other smaller diffuser passages did not line up with any guide vane passages. The potential importance of this diffuser characteristic was overlooked when designing the combustor. The high local temperature that caused vane heating was mitigated by ensuring the exit gas temperature stayed below 1200 K.

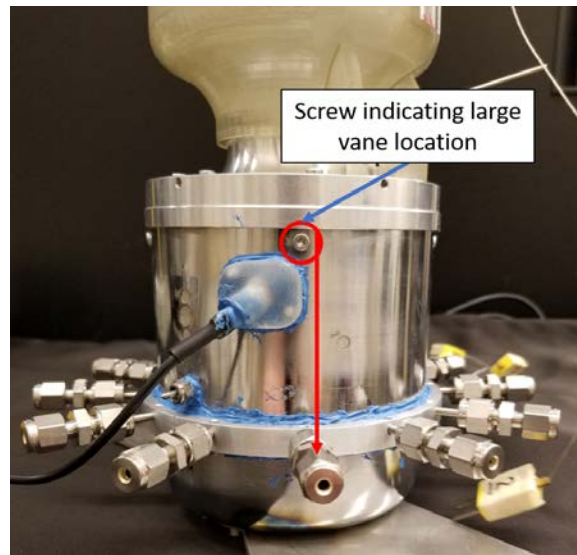


Figure 69. A side view of the engine, highlighting the location of the large diffuser vane, where the screw holds the diffuser to the case.

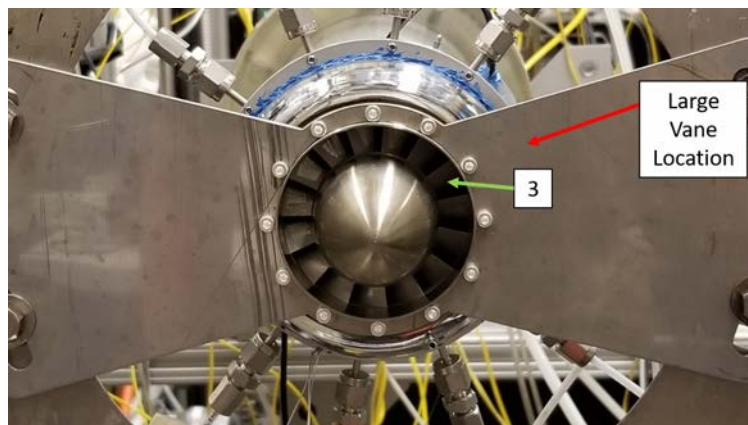


Figure 70. A rear view of the engine, highlighting the location of the diffuser irregularity with respect to turbine nozzle guide Vane 3.

As discussed earlier, the new combustor was operating in the equivalence ratio range of 0.2 to 0.21. At the time of testing, the low equivalence ratio did not raise any immediate red flags. However, this equivalence ratio for air and propane seemed low to produce the high temperatures that were recorded in the combustor. Idealized analysis of a propane-air reaction was done to determine the adiabatic flame temperature at several equivalence ratios. This analysis provided a baseline of what equivalence ratio would be expected for the recorded temperatures. At the equivalence ratio of 0.21, the reported adiabatic flame temperature was 870 K. This did not correspond to the temperatures seen exiting the combustor, implying that a much higher equivalence ratio was present in the combustor. In fact, an equivalence ratio on the order of 0.33 would be more reasonable for the observed exit temperatures. In addition, this was close to the expected equivalence ratio from JetCat and computational data of 0.34 at idle.

The low equivalence ratios led to concerns of whether the fuel or air supply was not providing the commanded flow rates. Initially, the fuel mass flow controller was investigated. However, according to calibration tests done by Bohan and Staton, the fuel mass flow controller was operating properly and reporting the correct flow rate values. The fuel flow lines were examined for leaks and none were found. In addition, a leakage in fuel would not cause the observed rise in temperature, but rather a drop in exit gas temperature. Therefore, the air supply flow controller was questioned. Without the appropriate hardware available in the COAL lab, the mass flow rate downstream of the air flow controller was not able to be verified. In lieu of a downstream mass flow meter, the reported air mass flow rate data was examined and compared to the expected air mass flow rate values. This was done to check if fluctuations in the air mass flow rate were causing the changes to equivalence ratio.

Two conditions were examined from the air mass flow meter data: light and idle. These two conditions would provide the extreme cases for operation of the engine with the light condition having the lowest air mass flow rates and the idle condition having the highest air mass flow rates tested. Before the data was reviewed, calculations were completed to determine how much of a fluctuation would be needed to obtain an equivalence ratio of 0.33 from the commanded 0.21. The result was that fluctuations on the order of 11.8 g/s (0.71 kg/min) at the light condition and 23.5 g/s (1.41 kg/min) at the idle condition were required. When the data was examined, the light condition had a maximum fluctuation of 3.8 g/s (0.23 kg/min) about its average of 30.2 g/s (1.81 kg/min) and the idle had a maximum of 3.2 g/s (0.19 kg/min) about its average of 72.0 g/s (4.32 kg/min). The expected air mass flow rates at these conditions were 31 g/s and 72.1 g/s.

Therefore, the recorded fluctuations and averages from the air mass flow controller at these conditions were not significant enough to cause the discussed changes in equivalence ratio. The only logical conclusions left available were that the air mass flow meter was not within calibration specifications or that there was significant leakage downstream of the air mass flow controller. However, to reiterate the hardware to measure the flow downstream of the controller and meter was not available to determine whether this was the case. All in all, the rotating testing would not require forced air and would provide the appropriate equivalence ratio for engine operation.

After the non-rotating testing was completed, the engine was disassembled in order to integrate the rotating hardware. In this process, the combustor was removed and examined. No material deformation or damage was found and no defining geometric characteristics were noticed that could have altered flow paths and resulted in the hot regions discussed above. However, the combustor was found to have heating patterns that corresponded to regions where flame holding was present. Figure 71 shows

combustor post-test pictures alongside the surface contours for the idle condition from Figure 56. The heated areas on the combustor corresponded to areas on the computational model that reached temperatures above 1000 K.

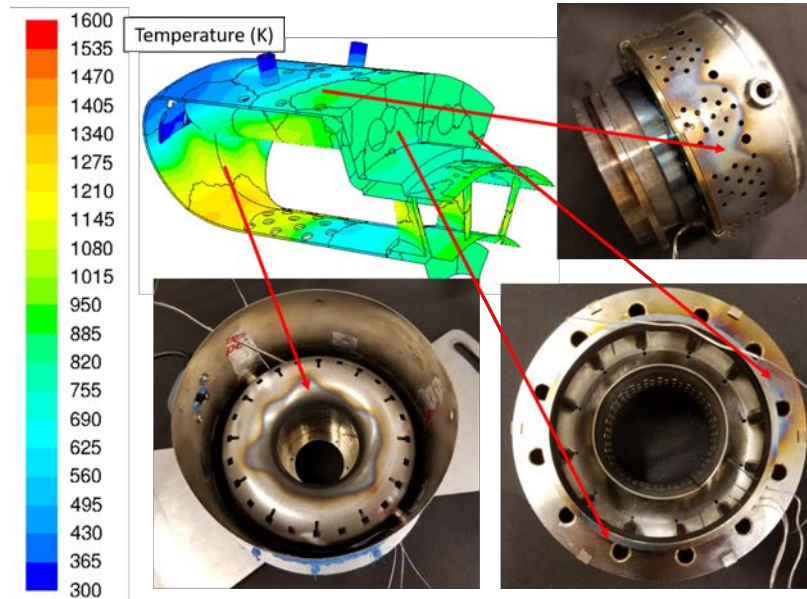


Figure 71. Several views of the combustor post non-rotating testing compared to the surface temperature contours from the computational results.

4.3 Rotating Experimental Results

The rotating testing was accomplished to test the operability of the new UCC with rotating turbomachinery. The test stand and instrumentation from Sections 3.5.5 and 3.6.2 were used. The rotating testing began by turning on the air starter and spooling the engine up to 3,000 RPM. Once this engine speed was reached, the glow plug was turned on and the Alicat was commanded to flow propane. At a fuel mass flow rate of 0.0079 kg/min (4 SLPM setpoint) and engine speed of 3,450 RPM, the fuel-air mixture ignited and the engine speed increased as temperatures downstream of the combustor increased. Figure 72 shows the temperature data from the first run of the JetCat P90 RXi with the UCC against engine speed, along with the mass flow rate

of propane from the Alicat. The fuel flow rate was rapidly increased such that the engine did not linger at low engine speeds. At low engine speeds, the engine was not able to push lubrication to the shaft bearings and would have resulted in bearing damage.

Once the engine reached 11,000 RPM, the air starter was shut off to evaluate the engine's ability to self-sustain at low engine speeds. The engine speed dropped while the downstream temperatures increased, due to the sudden drop in air mass flow through the engine. The engine was not recovering the speed lost from the air starter. Fuel was shut off to keep temperatures from exceeding 1300 K. A second test run was started that would leave the air starter turned on until an engine speed closer to the idle condition was reached. At higher engine speeds, the air flow contribution from the air starter would have been smaller and therefore would not have had as large of an effect when turned off.

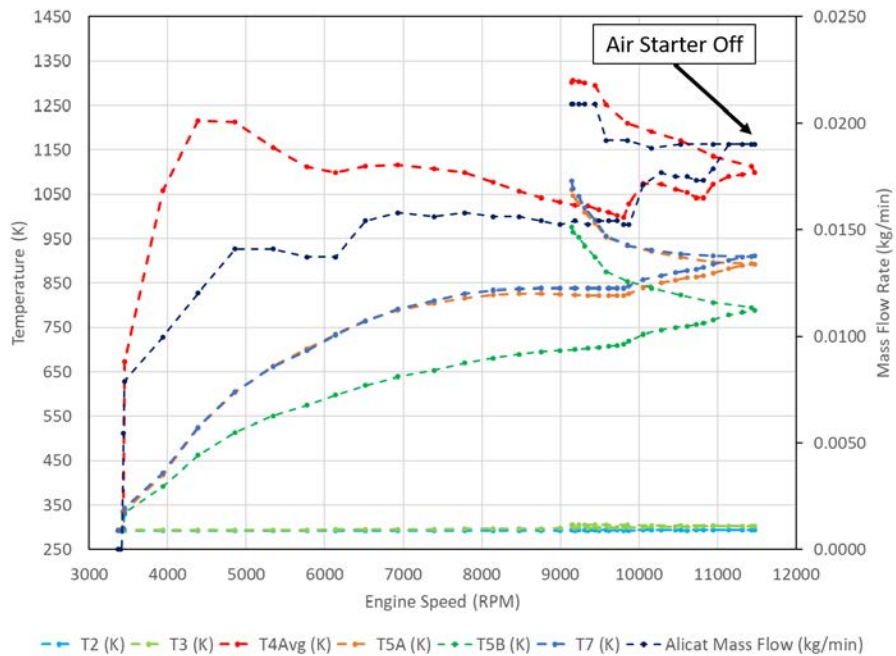


Figure 72. Temperature and fuel mass flow rate data against the engine speed from the first run of rotating testing.

The second test run began much like the first, with the fuel-air mixture igniting at a fuel mass flow rate of 0.0062 kg/min (3 SLPM setpoint) and engine speed 3,690 RPM, shown in Figure 73. The air starter was left on as the fuel flow rate was increased. With each step in fuel flow rate the temperature downstream of the combustor increased. After reaching 21,000 RPM, the engine settled at an exit gas temperature of 980 K while still increasing fuel flow rate and engine speed, up to 25,000 RPM. Once the engine reached a steady operation, as it did here, the air starter should have been shut off and the engine would have remained self-sustaining, based on the steady temperatures downstream of the combustor. However, the Station 4 temperature was significantly high at 1150 K causing potential overheating of the turbine blades. To ensure overall safety, the engine was shutdown.

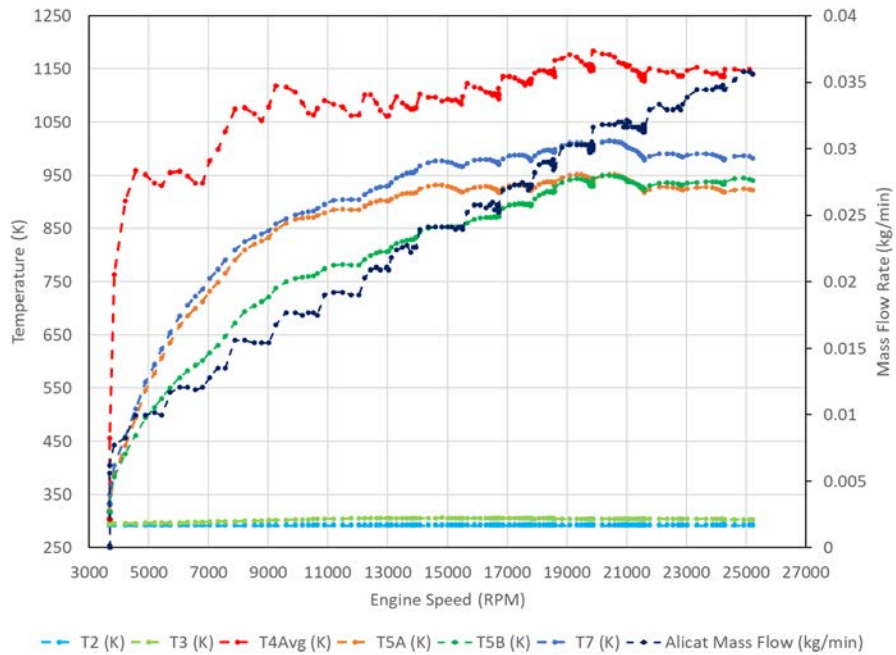


Figure 73. Temperature and fuel mass flow rate data against the engine speed from the second run of rotating testing, up to 25,000 RPM.

The UCC held a stable flame for the engine up to an engine speed of 25,000 RPM, just 11,000 RPM away from the idle condition. There were no signs of combustion fluctuations or potential flame blowout, as the engine steadily increased engine speed, pressures, and temperatures. Figure 74 shows the pressure data from the second test run against engine speed. The pressure data indicated that the engine pressure would have continued to increase past 25,000 RPM, approaching the stock 101.325 kPa operating pressure at the idle condition. This is further demonstrated by the trendlines for the compressor and turbine pressure ratios in Figure 75. From the stock data, the pressure ratios at idle were 1.08 for the compressor and 0.92 for the turbine. The trendlines from Figure 75 indicate, with a 99.7% correlation, that the engine would have reached the idle condition pressure ratios.

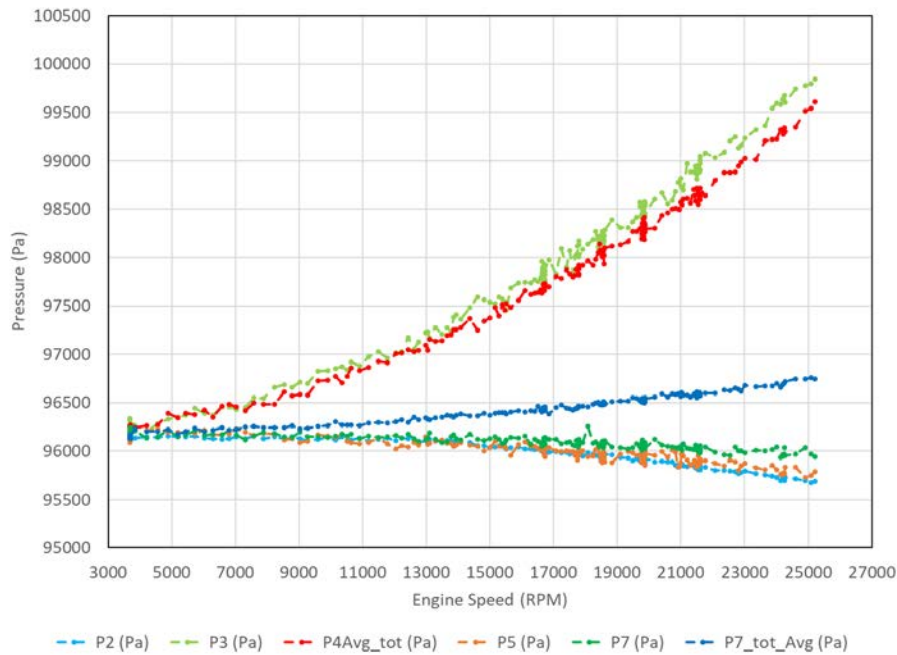


Figure 74. Pressure data against the engine speed from the second run of rotating testing.

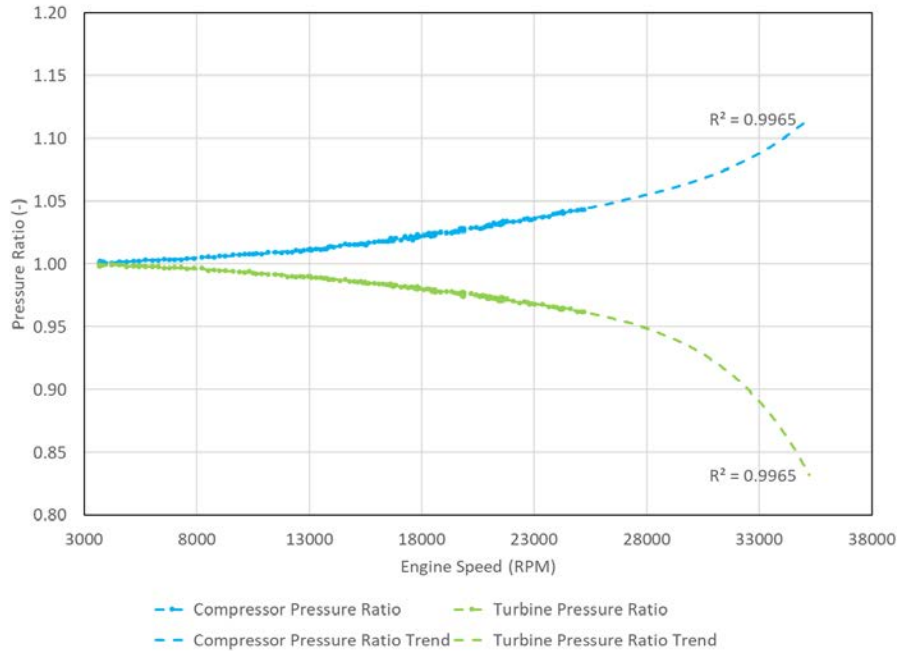


Figure 75. Compressor and turbine pressure ratios against the engine speed from the second run of rotating testing with predicted trendlines.

With the limited data collected from the rotating testing, limited comparisons were made. The turbine inlet temperature between 21,000 and 25,000 RPM of 1150 K matched within 1.2% of the stock idle turbine inlet temperature of 1136 K. The higher Station 4 temperature at 25,000 RPM fell in line with the general trend of the stock JetCat P90 RXi Station 4 temperature, shown in Figure 61b. In addition, the maximum pressure drop across the combustor was 0.45% as compared to the 2.0% drop calculated at the idle condition from CFD. The lower pressure drop was most likely due to not reaching the idle operating pressure; however, a lower pressure drop was acceptable for the testing. While the rotating testing was stopped prematurely, the engine and combustor performance indicated a favorable outcome for future rotating testing to reach higher engine speeds and achieve self-sustained operation.

V. Conclusions

The primary goal of this research was to design a UCC that would power the JetCat P90 RXi in a self-sustained operation at full engine power while achieving a 33% length savings relative to the stock combustor. This goal was supported by four objectives that involved designing the combustor within the JetCat P90 RXi constraints, analyzing the combustor using CFD, testing the combustor with non-rotating hardware, and running the engine powered by the newly designed combustor with rotating turbomachinery. Previous research on small scale engine combustors was conducted by Bohan et al. [1][2][3] and provided recommendations and hardware for continued compact combustor research.

5.1 Combustor Design

The first objective was resolved in Section 3.2, where the final version of the UCC was selected based on iterative computational analysis regarding combustor geometry, internal flow paths, pressure losses, and dilution hole patterns. The iterative process spanned several distinct combustor geometries. The first two design phases incorporated a physical wall that separated the combustor into two zones. These designs were set aside due to the high flow velocities through the transition channel between the two zones as well as the pressure loss experienced behind the separating wall. The wall was removed and an open chamber concept, similar to that of large scale combustors, was adapted for future designs.

The final combustor design utilized a simple open chamber design with air inlets on the forward dome, an impingement plate behind the inlets, fuel-air mixing tubes, and dilution holes on the inner and outer diameters. The simple design of the combustor allowed for the increase in fluidic volume recommended by Bohan et al. [1], where

the new combustor had a 32% increase in fluidic volume when compared to their high-g combustor. The amount of air entering the primary zone of the combustor was driven by the air inlets, which were sized such that 20% of the overall flow would enter the primary zone at the design condition. The impingement plate provided a stable flame holding mechanism for the combustor with the recirculation zones that formed behind the plate. This recirculation zone was fed by the fuel-air mixture exiting the mixing tubes. The mixing tubes would also allow for future integration of kerosene as the primary fuel. Lastly, the dilution holes provided the combustion reaction with additional air to complete the reaction as well as a means to tailor the exit profile of the combustor.

5.2 Computational Analysis

With the combustor design complete, a computational model was created using Solidworks and Pointwise, as discussed in Section 3.3. The model was generated as a 30° wedge of the outer engine case, combustor, turbine nozzle guide vane, and engine centerbody. The 30° wedge allowed for periodic boundaries to reduce computational time. The compressor exit and propane tube inlet were modeled as mass flow inlets and the turbine nozzle guide vane exit was set as a pressure outlet. The combustor was modeled as a conjugate surface such that heat transfer was allowed through the material.

Several aspects of the combustor were analyzed using ANSYS FLUENT at on and off design conditions, as discussed in Section 4.1. It was determined that the combustor provided a stable flame holding region for the combustion reactions to occur behind the impingement plate based on flow path visualizations and temperature contours showing high heat release. The dilution holes on the inner and outer diameters were shown to have significant effects on the combustor flow path, pushing hot gases

off the walls and towards the center of the chamber. Additionally, the combustor surface temperatures were analyzed to determine if the material would survive the combustion environment. The surface temperature did not exceed 1600 K at the on or off design conditions, indicating that the Inconel 600 material used for fabrication would not reach yield temperatures.

The turbine nozzle guide vane was examined for its effects on the turbine inlet profile. It was determined that a vortex formed on the outer diameter of the leading edge of the vane pulling hot gases from the midspan up towards the outer diameter. On the inner diameter, cooling jets prevented the vortex from forming. The turbine inlet temperature profile was studied, revealing that the combustor kept hot gasses near the midspan of the radial profile, keeping the hub and tips of the turbine cool. A pattern factor of 0.67 was found at the design point, which indicated a turbine inlet profile with some hot spots but not unreasonable for operation.

The new combustor was then compared to the stock JetCat P90 RXi combustor. The computational conditions were matched with engine speed conditions with similar air mass flow rates and equivalence ratios. The average turbine inlet temperatures were compared and showed that the computational results produced lower values but followed the same trend as the stock data. The stock data was collected at the midspan of the combustor exit which would have resulted in higher temperatures than an overall exit average, provided by CFD. The peak exit temperatures from CFD were used as a comparison to the stock data and provided closer matching results with an increase of 50 K over the stock combustor at the design point.

5.3 Non-Rotating Testing

From the computational results, it was determined that physical hardware was acceptable for further testing. The combustor was mostly fabricated out of Inconel

600 0.508 mm thick sheet metal, which was rolled, stamped, and welded together to form the multiple pieces of the combustor, as described in Section 3.4. The combustor was then integrated with the non-rotating configuration of the JetCat P90 RXi in the AFIT COAL lab. Sections 3.5 and 3.6 discussed the facility, hardware, and instrumentation utilized in both the non-rotating and rotating configurations.

The results of the non-rotating testing were presented in Section 4.2. The UCC consistently achieved ignition at low air and fuel mass flow rates, 31 g/s and 0.399 g/s. The non-rotating testing showed that the UCC was capable of holding a stable flame at the engine's idle condition. An equivalence ratio test was done that pushed the combustor to a maximum equivalence ratio of 0.235 at the idle condition, resulting in an average exit temperature of 1086 K and a maximum temperature at the midspan of 1222 K. The combustor provided consistent results between tests with matching equivalence ratios, varying a maximum of 25 K between independent runs. Turbine inlet temperature contours were obtained using the thermocouple rake. The contours showed that the temperature profile was more desirable than predicted with CFD, with a pattern factor of 0.38 which fell within the bounds provided by literature.

During the non-rotating testing, some turbine nozzle guide vanes were visibly radiating when high exit temperatures were recorded. Vane 3 continued to visibly radiate even when lower fuel flow rates were used as a precautionary measure. The propane distribution order was changed to eliminate any potential bias in fuel distribution, but Vane 3 continued to radiate. A potential cause for the hot region behind Vane 3 was a local high equivalence ratio due to a decrease in local air mass flow rate. The Vane 3 passage aligned with a smaller compressor diffuser vane passage that would have restricted the amount of air entering that local region. In addition, the calculated equivalence ratios from the testing were too low to produce the recorded exit temperatures, according to idealized analysis. Both the air and fuel mass flow

rate controllers were investigated for potential calibration issues. The fuel mass flow controller was checked with a calibration tool and was operating properly. The air mass flow controller was not able to be checked as the proper equipment was not available. No large fluctuations were recorded in either air or fuel mass flow rates and so the cause of the low equivalence ratio was thought to be either a badly calibrated air mass flow controller or a large leak downstream of the controller.

5.4 Rotating Testing

The non-rotating testing proved that the combustor survived the combustion environment and integrated properly with the JetCat P90 RXi. The rotating turbomachinery was placed in the engine to conduct the final phase of testing. Section 4.3 discussed the data gathered from the rotating configuration testing. Initially, the engine was operated up to an engine speed of 11,000 RPM, with the help of the air starter. The air starter was then turned off to attempt a self-sustained mode. However, the engine began to rapidly lose speed and increase in exit gas temperature. The engine was shutdown and a second test was conducted. The engine was operated up to a maximum engine speed of 25,000 RPM with the air starter on, reaching steady operation after 21,000 RPM at an exit gas temperature of 980 K. This performance compared well against the trend of the stock JetCat P90 RXi data and should have reached the idle condition in a self-sustained mode; however, the engine was stopped at 25,000 RPM due to general safety concerns.

The engine was able to reach a maximum engine speed of 25,000 RPM but did not achieve self-sustained operation at full power with the UCC during this research. Future research should look to test the JetCat P90 RXi with the new UCC in a facility at the Air Force Research Laboratory where the engine can safely be pushed to higher conditions. The engine should be able to achieve self-sustained operation

after 21,000 RPM, based on the steady operation that was observed at and above that speed. In addition, future research should implement kerosene as the primary fuel, utilizing the heated fuel-air mixing tubes to vaporize the liquid fuel. Once the switch to kerosene has been accomplished, the combustor can be scaled up to larger engine sizes (similar to the JetCat P400) to increase future combined efforts with the Air Force Research Laboratory Combustion Branch. While the final objective was not fully completed, this research still proved the further viability of a UCC in a small gas turbine engine. The engine was able to operate and achieved favorable performance with the 33% combustor length reduction.

Bibliography

1. Bohan, B. T. and Polanka, M. D., “Experimental Analysis of an Ultra Compact Combustor Powered Turbine Engine,” *Turbo Expo 2019*, Phoenix, AZ, 2019, GT2019-90607.
2. Bohan, B. T. and Polanka, M. D., “A New Spin on Small-Scale Combustor Geometry,” *Journal of Engineering for Gas Turbines and Power*, Vol. 141, 2019, pp. 011504 1–10.
3. Bohan, B. T., *Combustion Dynamics and Heat Transfer in an Ultra Compact Combustor*, Ph.D. thesis, Air Force Institute of Technology, 2018.
4. Mattingly, J. D., Heiser, W. H., and Pratt, D. T., *Aircraft Engine Design, Second Edition*, American Institute of Aeronautics and Astronautics, 2012.
5. Mattingly, J. D. and Boyer, K. M., *Elements of Propulsion: Gas Turbines and Rockets*, AIAA, Reston, VA, 2nd ed., 2016.
6. Samuelson, S., “Conventional Type Combustion,” *Advance Power and Energy Program*, 2006, pp. 209–217.
7. Turns, S. R., *An Introduction to Combustion: Concepts and Applications*, McGraw Hill, New York, 3rd ed., 2012.
8. Williams, F. A., “Flame Stabilization of Premixed Turbulent Gases,” *Applied Mechanics Surveys*, 1966, pp. 1157–1170.
9. Lapsa, A. P. and Dahm, W. J., “Hyperacceleration Effects on Turbulent Combustion in Premixed Step-Stabilized Flames,” *Proceedings of the Combustion Institute*, Vol. 32, No. 2, 2009, pp. 1731–1738.
10. Huang, Y. and Yang, V., “Dynamics and Stability of Lean-Premixed Swirl-Stabilized Combustion,” *Progress in Energy and Combustion Science*, Vol. 35, No. 4, 2009, pp. 293–364.
11. Young, D. F., Munson, B. R., and Okiishi, T. H., *A Brief Introduction to Fluid Mechanics*, Wiley, 3rd ed., 2004.
12. Bohan, B. T., Polanka, M. D., and Goss, L. P., “Measurements of Temperature, Pressure, Velocity, and Frequency in an Ultra Compact Combustor,” *AIAA SciTech Forum*, AIAA, Kissimmee, Florida, 2018, AIAA-2018-1875.
13. DeMarco, K. J., Bohan, B. T., Polanka, M. D., and Goss, L. P., “Performance Characterization of a Circumferential Combustion Cavity,” *AIAA Propulsion and Energy Forum, Joint Propulsion Conference*, AIAA, Cincinnati, OH, 2018, AIAA-2018-4922.

14. Sirignano, W., Delplanque, J.-P., and Liu, F., "Selected Challenges in Jet and Rocket Engine Combustion Research," *33rd Joint Propulsion Conference and Exhibit*, AIAA, Seattle, 1997, AIAA-1997-2701.
15. Zelina, J., Ehret, J., Hancock, R., Roquemore, W., Shouse, D., and Sturgess, G., "Ultra-Compact Combustion Technology Using High Swirl for Enhanced Burning Rate," *38th AIAA/ASME/SAE/ASEE Joint Propulsion Conference & Exhibit*, AIAA, Indianapolis, Indiana, 2002, AIAA-2002-3725.
16. Lewis, G., "Swirling Flow Combustion - Fundamentals and Application," *AIAA/SAE 9th Propulsion Conference*, AIAA, Las Vegas, Nevada, 1973, AIAA-1973-1250.
17. Briones, A. M., Sekar, B., and Erdmann, T., "Effect of Centrifugal Force on Turbulent Premixed Flames," *Journal of Engineering for Gas Turbines and Power*, Vol. 137, No. 1, 2014, pp. 011501 1–10.
18. Hsu, K.-Y., Goss, L. P., and Roquemore, W. M., "Characteristics of a Trapped-Vortex Combustor," *Journal of Propulsion and Power*, Vol. 14, No. 1, 1998, pp. 57–65.
19. Bills, J. D., *Liquid Fuel Film Cooling: A CFD Analysis with Hydrocarbon Fuel*, Ph.D. thesis, Air Force Institute of Technology, 2016.
20. ANSYS, I., *FLUENT 17.2 User's Guide*, Canonsburg, PA, 2018.
21. Cummings, R. M., Mason, W. H., Morton, S. A., and McDaniel, D. R., *Applied Computational Aerodynamics: A Modern Engineering Approach*, Cambridge University Press, 2015.
22. Menter, F. R., "Two-Equation Eddy-Viscosity Turbulence Models for Engineering Applications," *AIAA Journal*, Vol. 32, No. 8, 1994, pp. 1598–1605.
23. Patankar, S., "Conjugate Heat Transfer," *Numerical Heat Transfer and Fluid Flow*, Hemisphere, 1980, p. 149.
24. Lefebvre, A. H., *Gas Turbine Combustion*, Taylor and Francis, 2nd ed., 1998.
25. Thomas, N., Rumpfkeil, M., Briones, A., Rankin, B., and Erdmann, T. J., "CFD-Based Machine Learning Methodology for Combustor Design Optimization," *44DCASS-167*, AIAA, Dayton, 2018.
26. Special Metals Corporation, "INCONEL ® alloy 718," Tech. rep., 2007.
27. Special Metals Corporation, "INCONEL ® alloy 600," Tech. rep., 2008.

REPORT DOCUMENTATION PAGE

Form Approved
OMB No. 0704-0188

The public reporting burden for this collection of information is estimated to average 1 hour per response, including the time for reviewing instructions, searching existing data sources, gathering and maintaining the data needed, and completing and reviewing the collection of information. Send comments regarding this burden estimate or any other aspect of this collection of information, including suggestions for reducing this burden to Department of Defense, Washington Headquarters Services, Directorate for Information Operations and Reports (0704-0188), 1215 Jefferson Davis Highway, Suite 1204, Arlington, VA 22202-4302. Respondents should be aware that notwithstanding any other provision of law, no person shall be subject to any penalty for failing to comply with a collection of information if it does not display a currently valid OMB control number. **PLEASE DO NOT RETURN YOUR FORM TO THE ABOVE ADDRESS.**

1. REPORT DATE (DD-MM-YYYY) 10-06-2020		2. REPORT TYPE Master's Thesis		3. DATES COVERED (From — To) Sept 2018 — Mar 2020	
4. TITLE AND SUBTITLE DESIGN AND ANALYSIS OF A COMPACT COMBUSTOR FOR INTEGRATION WITH A JETCAT P90 RXI				5a. CONTRACT NUMBER	
				5b. GRANT NUMBER	
				5c. PROGRAM ELEMENT NUMBER	
6. AUTHOR(S) Daniel Holobeney				5d. PROJECT NUMBER	
				5e. TASK NUMBER	
				5f. WORK UNIT NUMBER	
7. PERFORMING ORGANIZATION NAME(S) AND ADDRESS(ES) Air Force Institute of Technology Graduate School of Engineering and Management (AFIT/EN) 2950 Hobson Way WPAFB OH 45433-7765				8. PERFORMING ORGANIZATION REPORT NUMBER AFIT-ENY-MS-20-M-266	
9. SPONSORING / MONITORING AGENCY NAME(S) AND ADDRESS(ES) Dr. Drew Caswell, AFRL/RQTC 2130 Eighth Street WPAFB OH 45433-7542				10. SPONSOR/MONITOR'S ACRONYM(S)	
				11. SPONSOR/MONITOR'S REPORT NUMBER(S)	
12. DISTRIBUTION / AVAILABILITY STATEMENT DISTRIBUTION STATEMENT A: APPROVED FOR PUBLIC RELEASE; DISTRIBUTION UNLIMITED.					
13. SUPPLEMENTARY NOTES					
14. ABSTRACT Ultra Compact Combustors are a novel approach to modern gas turbine combustor designs that look to reduce the overall combustor length and weight. A previous study integrated an Ultra Compact Combustor into a JetCat P90 RXi turbine engine and achieved self-sustained operation with a length savings of 33% relative to the stock combustor. However, that combustor could not operate across the full stock engine performance range due to flameout at increased mass flow rates as reactions were pushed out of the primary zone. To ensure reactions stayed in the primary zone, a new design with a larger combustor volume was conceived maintaining the same axial dimensions. The design was investigated computationally for generalized flow patterns, pressure losses, exit temperature profiles, and reaction distributions throughout the combustor at three engine power conditions. The combustor was then built and tested in the JetCat P90 RXi with and without rotating turbomachinery. The combustor responded well to changes in air and fuel flow rates and operated with rotating hardware.					
15. SUBJECT TERMS UCC, Small Gas Turbine Engine, Combustion					
16. SECURITY CLASSIFICATION OF:			17. LIMITATION OF ABSTRACT	18. NUMBER OF PAGES	19a. NAME OF RESPONSIBLE PERSON
a. REPORT	b. ABSTRACT	c. THIS PAGE			19b. TELEPHONE NUMBER (include area code)
U	U	U	U	124	Dr. Marc D. Polanka, AFIT/ENY (937) 255-3636, x4714; marc.polanka@afit.edu